UNIVERSITY OF LIVERPOOL

Porous Organic Cages: Synthesis and Application in Noble Gas Separation

Paul Stefan Reiss

Department of Chemistry

Supervisor: Prof. Andrew Cooper

Thesis submitted in accordance with the requirements of the University of Liverpool for the degree of Doctor of Philosophy

July 2015

Acknowledgements

Firstly, I extend a great deal of gratitude towards Professor Andy Cooper for giving me the opportunity to work on this project within his research group. I have thoroughly enjoyed my time at the University of Liverpool and I would like to thank him for his guidance and encouragement. I would also like to offer a big thanks to Dr Michael Briggs, who has proven instrumental throughout my PhD, especially with regards to his help and advice concerning organic synthesis, among other things, which have proven invaluable and made me a better chemist as a result.

There are many people within the Cooper group who I would like to thank for making a major contribution to this thesis: Dr Tom Hasell for gas adsorption measurements, scanning electron microscope images and helpful discussion throughout the PhD, Dr Marc Little for single crystal X-ray diffraction analysis and displacement ellipsoid plots of all the crystal structures presented herein, Dr Sam Chong for powder X-ray diffraction analysis and Le Bail refinement, Dr Shan Jiang for scanning electron microscope images and Dr Dan Holden for molecular dynamics simulations. I also owe thanks to Mr Rob Clowes (Centre for Materials Discovery) for gas adsorption measurements, Dr Michael Barrow (University of Liverpool) for his help regarding centrifugation and freeze-drying, Mr Gareth Smith (University of Manchester) for MALDI-TOF mass spectrometry, Dr Angeles Pulido and Dr Graeme Day (University of Southampton) for computational crystal-structure prediction, as well as Dr Maciej Haranczyk (Lawrence Berkeley National Laboratory) for molecular dynamics simulations.

I owe a special thanks to Dr Praveen Thallapally for allowing me to work on the separation of noble gases within his research group at the Pacific Northwest National Laboratory. Both himself and Dr Jian Liu helped me immensely during my short time there and ensured I had a memorable and rewarding experience.

Finally, I would like to thank every member of the Cooper group, past and present, as each one has helped me in some sort of way during my PhD and ensured that I enjoyed my time in Liverpool from beginning to end.

Abstract

Porous organic cages have recently received much attention due to their synthetic tunability, solution processability, high gas adsorption capacities, and ability to selectively separate small molecules based on their size and shape. In this thesis, a range of novel porous organic cages are presented, with each possessing unique functionalities, pore structures and gas sorption properties due to the employment of synthetically-modified versions of traditional trialdehyde and diamine cage precursors. The introduction of new functionality into the cage structure, including methyl, hydroxyl and ethanoanthracene groups, highlights how subtle modification of the cage precursors can initiate significant changes in the self-assembly of the cage molecules. This in turn affects the pore dimensions, as well as the gas sorption and separation performance, of the resultant porous material. This strategy led to the successful isolation of an asymmetric cage molecule, which demonstrated the potential to separate noble gases, as well as the preparation of cages with diverse vertex functionality, molecular size and gas sorption properties. The ability of porous organic cages to selectively separate xenon from krypton gas was also investigated through the use of dynamic breakthrough measurements, with the performance of these cages surpassing all other porous materials evaluated to date.

Abbreviations

BET	Brunauer–Emmett–Teller
CHN	Elemental Analysis
CI	Chemical Ionisation
CMP	Conjugated Microporous Polymer
COF	Covalent Organic Framework
CSP	Crystal-Structure Prediction
ESI	Electrospray Ionisation
FTIR	Fourier-Transform Infrared Spectroscopy
GCMC	Grand Canonical Monte Carlo
HCP	Hyper-Cross-Linked Polymer
HPLC	High-Performance Liquid Chromatography
MALDI	Matrix-Assisted Laser Desorption Ionisation
MD	Molecular Dynamics
MOF	Metal-Organic Framework
MS	Mass Spectrometry
NMR	Nuclear Magnetic Resonance
OCF	Organic-Cage Framework
PAF	Porous Aromatic Framework
PIM	Polymer of Intrinsic Microporosity
PLD	Pore-Limiting Diameter
PLE	Pore-Limiting Envelope
POC	Porous Organic Cage
PSD	Pore-Size Distribution
PSM	Post-Synthetic Modification
PXRD	Powder X-ray Diffraction
RP	Reverse Phase
SBU	Secondary Building Unit
scXRD	Single Crystal X-ray Diffraction
SEM	Scanning Electron Microscopy
TGA	Thermogravimetric Analysis
TOF	Time-Of-Flight
UNF	Used-Nuclear Fuel

Chemical Abbreviations

Br_3TFB	1,3,5-Tribromo-2,4,6-tris(formyl)benzene
CHDA	Cyclohexanediamine
DCM	Dichloromethane
DCTB	*trans*-2-[3-(4-*tert*-Butylphenyl)-2-methyl-2-propenylidene]malononitrile
DMF	Dimethylformamide
DMSO	Dimethyl sulfoxide
EA	Ethanoanthracene
EDA	Ethylenediamine
Et_3TFB	1,3,5-Triethyl-2,4,6-tris(formyl)benzene
*m*CPBA	*meta*-Chloroperbenzoic acid
Me_3TFB	1,3,5-Trimethyl-2,4,6-tris(formyl)benzene
NMP	*N*-Methyl-2-pyrrolidone
PCC	Pyridinium chlorochromate
R,*R*-CHDA	(*R*,*R*)-1,2-Cyclohexanediamine
SBI	1,1'-Spirobisindane
TB	Trögers base
TBAF	Tetrabutylammonium fluoride
TBDMS	*tert*-Butyldimethylsilyl
TFA	Trifluoroacetic acid
TFB	1,3,5-Triformylbenzene
TFE	2,2,2-Trifluoroethanol
THF	Tetrahydrofuran
TTBI	Triptycenetrisbenzimidazolone

Contents

Chapter 1

Introduction

1.1 Porous Materials

Porous materials are important for a wide range of applications, especially in areas such as molecular separations, gas storage and catalysis.[1] These materials can be classified according to their pore size:[2] (i) pores with widths exceeding 50 nm are called *macropores*; (ii) pores with widths between 2 nm and 50 nm are called *mesopores*, and; (iii) pores with widths smaller than 2 nm are called *micropores*. Specifically, microporous materials are of most interest in this thesis because their pore dimensions are comparable to small gas molecules such as N_2, H_2 and CO_2, which themselves are relevant in a range of gas storage and separation applications. According to Barbour, there are three types of porosity, each with its own definition.[3] Virtual porosity describes the deletion of selected atoms, typically solvent or ion molecules, from the crystal structure to afford a virtually porous material. In reality, this is not a stable form of porosity, since guest removal is usually accompanied by contraction of the crystal packing. Porosity "without pores" occurs when dynamic processes arise within the crystal during guest uptake. This creates transient opportunities for guest diffusion to occur, despite a lack of interconnected voids. Finally, conventional porosity is achieved when solvent molecules can be physically removed without disrupting the pore topology of the host.

Activated carbon (or charcoal) and zeolites are traditional and cheap classes of microporous materials. They exhibit high surface areas and are utilised in a wide variety of commercial applications including separation processes and heterogeneous catalysis.[4] However, the ability to tune pore size and therefore the properties of these materials is not as straightforward as it is to synthetically construct microporous materials consisting of novel chemical compositions. In recent years, a plethora of microporous materials have been prepared using various synthetic approaches, and their properties assessed, especially with respect to their ability to adsorb gases. An important factor in determining the significance of these microporous materials is the Brunauer-Emmett-Teller (BET) surface area, although other factors including selectivity and the incorporation of particular functionality also rank highly. In the interests of this thesis, microporous materials can be divided into two sub-sets: (i) those with extended frameworks and networks and (ii) those consisting of discrete organic molecules.

1.2 Porous Frameworks and Networks

1.2.1 Metal-Organic Frameworks (MOFs)

Also known as porous coordination polymers (PCPs), MOFs are a crystalline class of porous materials that have been the subject of intensive research over the past decade or so. They are constructed from metal-containing nodes (also known as secondary building units, or SBUs) and organic linkers, with most materials possessing 3-D structures comprising uniform pores and a network of channels.[5] The variance of these SBUs and organic linkers offers an enormous degree of structural and functional tunability, and hence the potential to design MOFs with deliberate and distinct structures and properties. Their permanent porosities, low densities, and well-defined pores and channels have identified MOFs as ideal candidates for a range of applications, ranging from gas storage and separations to catalysis.[6-8] In addition, their crystallinity allows detailed structural characterisation, which in conjunction with computational modelling helps both predict and aid explanation of their physical properties.[9]

Li *et al*. reported one of the first examples of a MOF demonstrating microporosity, where Zn(BDC – 1,4-benzenedicarboxylate) was shown to have a Langmuir surface area of 310 m^2 g^{-1}.[10] Since then, the reported surface areas of MOFs have risen significantly, encompassing a wide range of SBUs, organic linkers and topologies. In 2002, Eddaoudi *et al.* presented a series of MOFs based on MOF-5,[11] which is constructed from octahedral Zn-O-C clusters and benzene links. Each framework was constructed to possess different pore functionalities and sizes whilst retaining the same framework topology as MOF-5 (Figure 1.1).[12] This isoreticular collection of MOFs (IRMOFs) was shown to be thermally stable and highlighted the ease with which different functional groups could be introduced whilst systematically varying both the pore size and the resulting porosity. By both extending the lengths of the organic linkers and employing a mixed linker strategy, Furukawa *et al.* demonstrated that this heterogeneity principle[13] could generate MOFs of extremely high permanent porosities, with MOF-210 exhibiting a BET surface area of 6240 m^2 g^{-1}.[14] This was the highest surface area ever measured until, in 2012, Farha *et al.* reported the MOF NU-110, which possessed a BET surface area of 7140 m^2 g^{-1}.[9] Using extended, slim hexa-carboxylated organic linkers consisting of an acetylene-based backbone,

ultrahigh porosity was attained, while the employment of an *rht*-topology avoided any structural fragility or self-interpenetration.

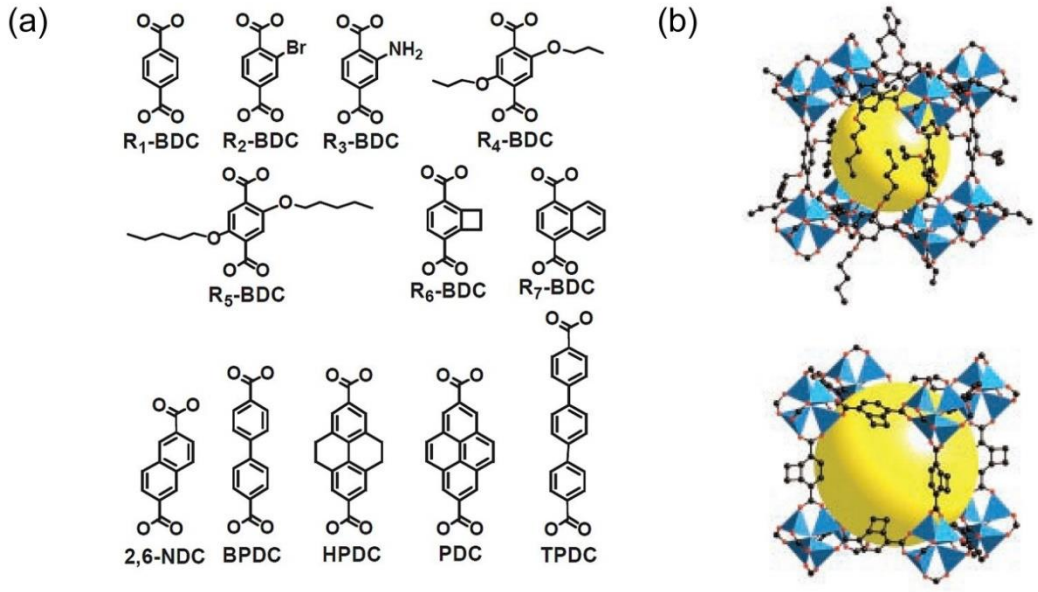

Figure 1.1 (a) Benzene-based organic linkers with different functionalities utilised in the synthesis of the IRMOF series. (b) Single crystal X-ray structures of IRMOF-5 (top) and IRMOF-6 (bottom).[12]

1.2.2 Covalent Organic Frameworks (COFs)

COFs are well-defined, crystalline porous structures composed of lightweight elements (C, O, B and N) linked by strong covalent bonds. In order to obtain a crystalline and ordered COF structure, the building units must react under dynamic covalent bond control and with the appropriate conformation and rigidity to enforce directional-bond formation.[15] Côté *et al.* were the first to report the successful preparation of COFs, with the 2-D materials COF-1 and COF-5 synthesised through boroxine and boronate ester bond formation respectively.[16] Both were found to possess high thermal stabilities and permanent porosities. Since then, a range of reversible approaches have been used to prepare COFs (Figure 1.2a), including those with 3-D architectures that have been shown to possess BET surface areas in excess of 4000 m^2 g^{-1}.[17] Due to their high surface areas and low densities, 3-D COFs are good candidates for the storage of gases, including H_2 and CH_4. Alternatively, as 2-D COFs consist of stacked sheets which form aligned columns (Figure 1.2b), they may also aid the transport of charge carriers in the stacking direction;[15] therefore offering

potential as semi-conducting and photo-conducting materials,[18] as well as materials for energy storage.[19]

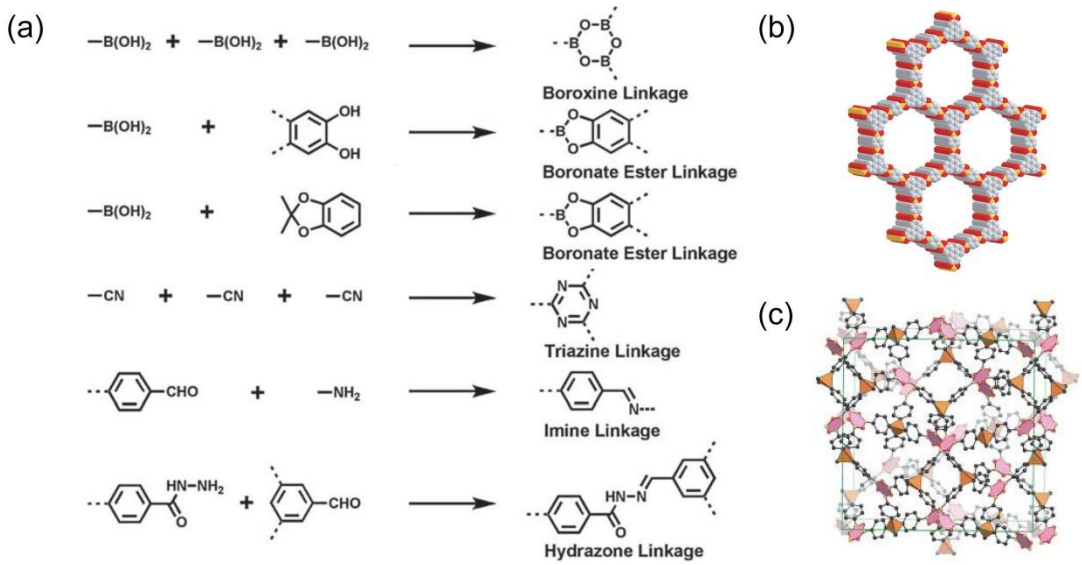

Figure 1.2 (a) Schematic representation of the reactions used for the synthesis of COFs.[15] (b) Structural representation of 2-D COF-5.[16] (c) Structural representation of 3-D COF-102.[17]

1.2.3 Polymers of Intrinsic Microporosity (PIMs)

PIMs can be prepared either as insoluble networks or as soluble linear polymers. Network-PIMs were originally developed by McKeown *et al.* to prepare phthalocyanine-based network polymers, where rigid spirocyclic cross-links were employed to prevent close-packing of the phthalocyanine components and give microporous materials with BET surface areas in the range 450 – 950 m^2 g^{-1}.[20]

The soluble linear polymers consist of robust covalent bonds, with the porosity arising from their rigid and highly contorted molecular structures being unable to pack efficiently in the solid state (Figure 1.3b).[21] A lack of rotational freedom ensures they cannot rearrange their conformation to initiate collapse; this retains the intrinsic microporosity. The classic example is PIM-1, which is prepared *via* dioxane formation using a 1,1'-spirobisindane (SBI), with the spiro-centre acting as the site of contortion, and 1,4-dicyanotetrafluorobenzene.[22] Isolated as an amorphous powder with a BET surface area of 860 m^2 g^{-1}, PIM-1 is soluble in organic solvents, which enables it to be cast into films to act as membranes for gas separation applications including O_2/N_2 and H_2/N_2 separations for example. A great number of PIMs have

been synthesised since then,[23-25] with different macromolecular backbones employed to enhance both shape persistence and performance.[26] An example of this is PIM-EA-TB, which contains both ethanoanthracene (EA) and Trögers base (TB) bicyclic units (Figure 1.3a).[26] Along with a high BET surface area in excess of 1000 m^2 g^{-1}, the rigidity of these units resulted in enhanced permeability properties compared to other PIM membranes.

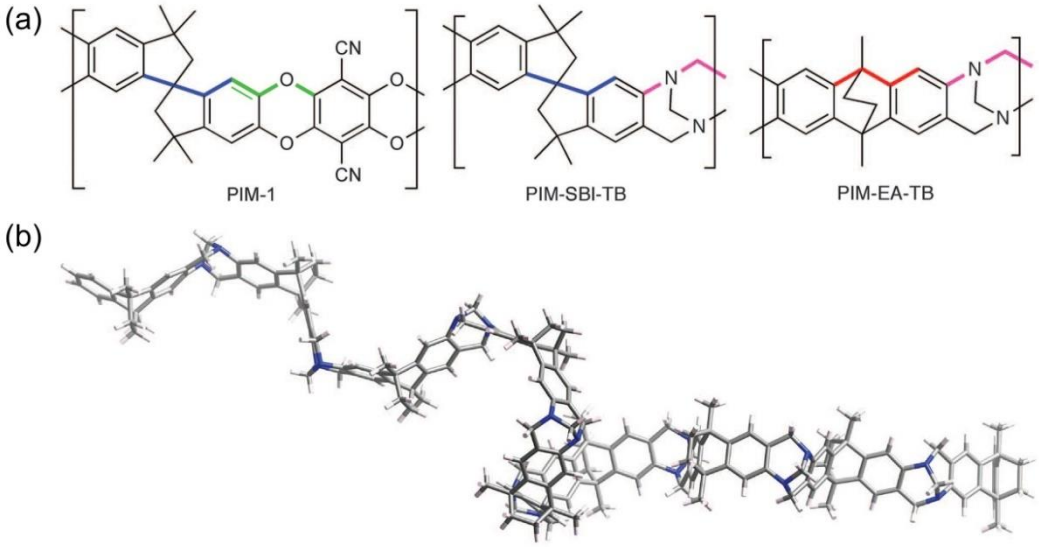

Figure 1.3 (a) Molecular structures of PIM-1, PIM-SBI-TB and PIM-EA-TB. (b) A molecular model of PIM-EA-TB demonstrating its contorted shape.[26]

1.2.4 Conjugated Microporous Polymers (CMPs)

The first generation of CMPs was reported by Cooper and co-workers, where organic conjugated poly(aryleneethynylene) polymers were synthesised *via* Sonogashira-Hagihara coupling (Figure 1.4b).[27] Prepared under kinetic control, amorphous solids were isolated with no long-range molecular order, unlike MOFs and COFs. Using rigid organic linkers of varying length enabled tuning of the microporosity, with BET surface areas of up to 834 m^2 g^{-1} being achieved.

CMP design relies on the covalent linking of building blocks with a π-conjugated bond (Figure 1.4a).[28] The preparation of a conjugated skeleton can be achieved using a range of synthetic reactions including Suzuki cross-coupling,[29] Yamamoto reaction[30] and cyclotrimerization,[31] for example. The ability to tune the pore size, geometry and functional groups inherent to the polymer structure gives rise to a large

number of potential porous materials, with applications ranging from heterogeneous catalysis to light harvesting.[32-34]

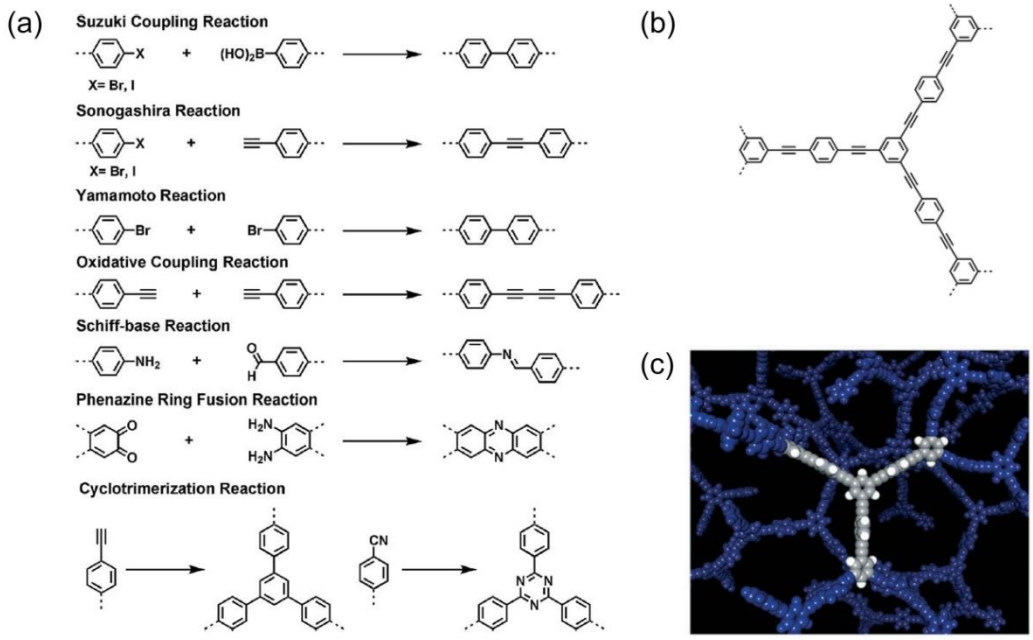

Figure 1.4 (a) Schematic representation of the reactions used for the synthesis of CMPs.[28] (b) Schematic representation of the structure and (c) the node-strut topology for simulated network fragments of CMP-1.[27]

1.2.5 Porous Aromatic Frameworks (PAFs)

PAFs are rigid open-framework structures constructed from covalent bonds. Their structure was originally based on that of diamond, whereby each carbon atom is tetrahedrally connected to four neighbouring atoms.[35] By inserting rigid phenyl rings and using an optimised nickel-catalysed Yamamoto-type Ullman-coupling procedure, Ben *et al.* were able to synthesise PAF-1, which was found to exhibit high physicochemical stabilities and a superb BET surface area of 5640 m^2 g^{-1}.[36] By replacing the tetrahedral sp^3-carbon with silicon and employing a mixed-solvent system at room temperature, Yuan *et al.* isolated PPN-4, which had a superior BET surface area of 6461 m^2 g^{-1}, and is among the most porous materials measured to date (Figure 1.5).[37]

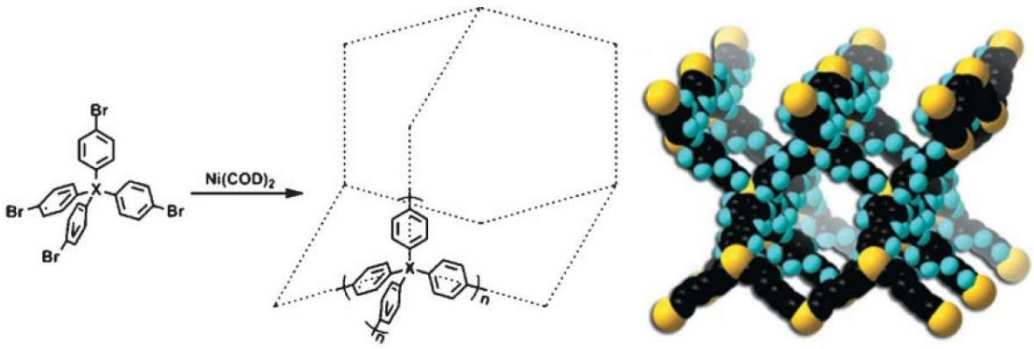

Figure 1.5 Synthetic route (left) for the synthesis of PAF materials including PAF-1 (X: C) and PPN-4 (X: Si) and a molecular model (right) demonstrating the idealised non-interpenetrated diamondoid network of PPN-4.[35]

1.2.6 Hyper-Cross-Linked Polymers (HCPs)

HCPs are typically prepared *via* Friedel-Crafts alkylation reaction, where permanent porosity results from extensive cross-linking preventing the polymer chains from collapsing into a non-porous state, with the resulting materials exhibiting high thermal and chemical stabilities.[38] They can be prepared in different ways, including post-crosslinking of polymers to form "Davankov-type" resins,[39] or by "knitting" together rigid aromatic building blocks using formaldehyde dimethyl acetal as an external cross-linker (Figure 1.6).[40] The latter strategy has proven to be especially effective because it enables microporous materials to be prepared using a range of aromatic monomers, as well as allowing the facile introduction of various functional groups to tune the properties.[41] In addition, this approach avoids the use of precious metal catalysts or the need to employ specific monomers with polymerisable groups. The BET surface areas of HCPs have been found to approach 1500 m^2 g^{-1},[42] and with their physicochemical stabilities and the ability to selectively capture large amounts of CO_2, HCPs have been shown to be strong candidates for the capture of CO_2 under pre-combustion conditions.[43]

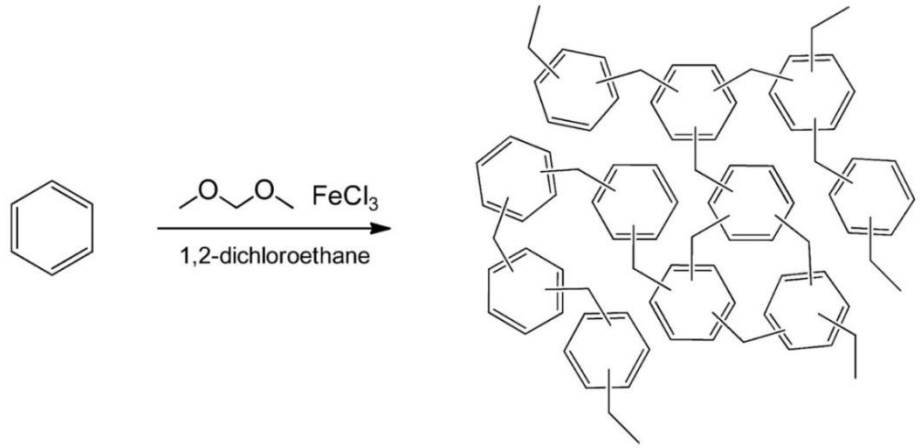

Figure 1.6 Reaction scheme for the synthesis of a microporous "knitted" HCP network.[43]

1.3 Porous Organic Molecules

The majority of microporous materials are composed of directional covalent or coordination bonds, such as the MOFs, COFs and organic network polymers that are discussed above. Permanently porous materials comprising discrete organic molecules are rare because most organic molecules pack efficiently in the solid state to form structures with minimal void volume.[44] Even if porosity is achieved, weak non-covalent interactions between the molecules can result in cavity collapse upon desolvation and hence the porosity is lost. Due to the range of non-covalent interactions which dictate their packing efficiency in the solid state, it is also challenging to predict the assembly of these molecules. Taking this into account, their design and synthesis must be carefully considered.

There are now many examples of organic molecules with structures that are stable towards desolvation, therefore forming permanently porous molecular crystals.[45] These range from molecules which typically possess a pre-fabricated "hole" of some type (e.g. cucurbiturils,[46] calixarenes,[47] Noria waterwheel[48] or porous organic cages[49]) to those where the porosity is generated through inefficient packing of the molecules (e.g. Dianin's compound,[50] tris(*o*-phenylenedioxy)cyclotriphosphazene (TPP)[51] or dipeptides[52]). From the viewpoints of synthetic strategy and properties, the latter approach has recently been shown to be adaptable in the creation of porous materials consisting of discrete molecules of specific shape and directionality. Kohl *et al.* synthesised a series of D_{3h}-symmetric shape-persistent triptycene

derivatives which displayed high internal molecular free volumes.[53] They were shown to form micropores in the solid state, with narrow pore-size distributions (PSDs) and BET surface areas as high as 754 m^2 g^{-1}. Similarly, Taylor *et al.* attached triptycene-based components to a biphenyl core, with their rigid structures preventing efficient packing.[54] These organic molecules of intrinsic microporosity (OMIMs) were shown to possess BET surface areas in the range 515 – 702 m^2 g^{-1}. Perhaps the most celebrated structure amongst this classification is that of triptycenetrisbenzimidazolone (TTBI), which was reported by Mastalerz and Oppel to self-assemble by co-operative hydrogen bonding to give a microporous crystalline material (Figure 1.7).[55] Upon activation *via* solvent swapping, the BET surface area was found to be a remarkable 2796 m^2 g^{-1}. This is among the highest surface areas ever measured for a discrete molecule.

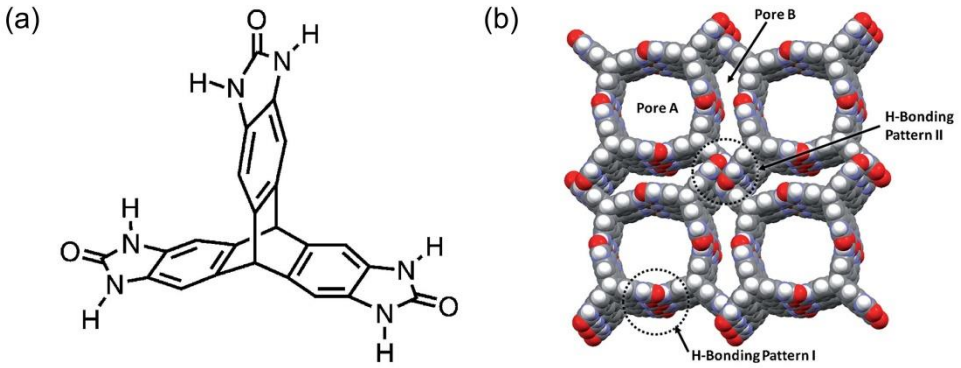

Figure 1.7 (a) Molecular structure and (b) single crystal X-ray structure of TTBI.[55]

The main advantage that porous organic molecules hold over extended frameworks and networks is that they can possess a high degree of solubility in a variety of solvents. This quality provides a degree of flexibility with regards to both their preparation and subsequent processing. The ability to dissolve them allows ease of purification *via* recrystallisation or chromatography, whilst the ability to post-synthetically modify their chemical structure, or induce the creation of new polymorphs, enables their properties to be tailored towards a certain function or application. In addition, they offer the potential to be cast into composite structures and deliver improved material properties. With regards to these ambitions, porous organic cage molecules have been instrumental in advancing the merits of this approach, making them an established class of porous materials in their own right.

1.3.1 Porous Organic Cages (POCs)

POCs have proven to be an effective and fascinating approach towards the synthesis of porous materials consisting of discrete organic molecules. The recent major advances that have been made in their preparation are due to the application of dynamic covalent chemistry. Under certain conditions, this exploits reversible covalent bond formation to achieve the most thermodynamically stable product.[56] This means that even once the initial products are formed, changing the reaction environment can result in an adjustment in their distribution towards the isolation of a single product.[57] By utilising this approach, POC molecules consisting of covalent bonds may be prepared, typically requiring the use of simple starting materials and proceeding in one step and in high yields. It is therefore a very powerful and adaptable tool. It has enabled a large number of POC molecules to be synthesised over the past few years, with many remaining shape-persistent upon desolvation and exhibiting BET surface areas to rival those of extended porous frameworks and networks.[58] The majority of POCs synthesised to date rely on the formation of an imine bond through the reaction of a primary amine and an aldehyde,[59] although more recently, boronate ester methodologies have also been shown to be a promising route towards their preparation.[60]

Imine Bond-Based Cages

The first series of POC molecules was reported by Tozawa *et al.* in 2009.[61] The reaction of 1,3,5-triformylbenzene (TFB) with three different vicinal diamines yielded [4+6] cages where the porosity was pre-fabricated and intrinsic to the cage structure, with the molecules packing together *via* non-covalent interactions to generate extended structures in the solid state (Figure 1.8). These cages were isolated as the most thermodynamically stable product and typically adopted a tetrahedral structure. The vertex functionality was shown to have a strong influence on both the crystal packing and topology of the resulting pore network (Figure 1.8b). For example, **CC1**, synthesised from the reaction of TFB and ethylenediamine (EDA), was formally non-porous to N_2 and packed in a window-to-arene fashion with no interconnected voids. By contrast, **CC3**, synthesised from the reaction of TFB with cyclohexanediamine (CHDA), was shown to pack window-to-window with a 3-D diamondoid pore network passing though the intrinsic cage voids. This was

represented by a BET surface area of 624 m^2 g^{-1}. The difference in crystal packing and surface area was due to the introduction of the cyclohexane vertex, which forced the generation of additional extrinsic porosity between the discrete cage molecules and created the observed pore structure.

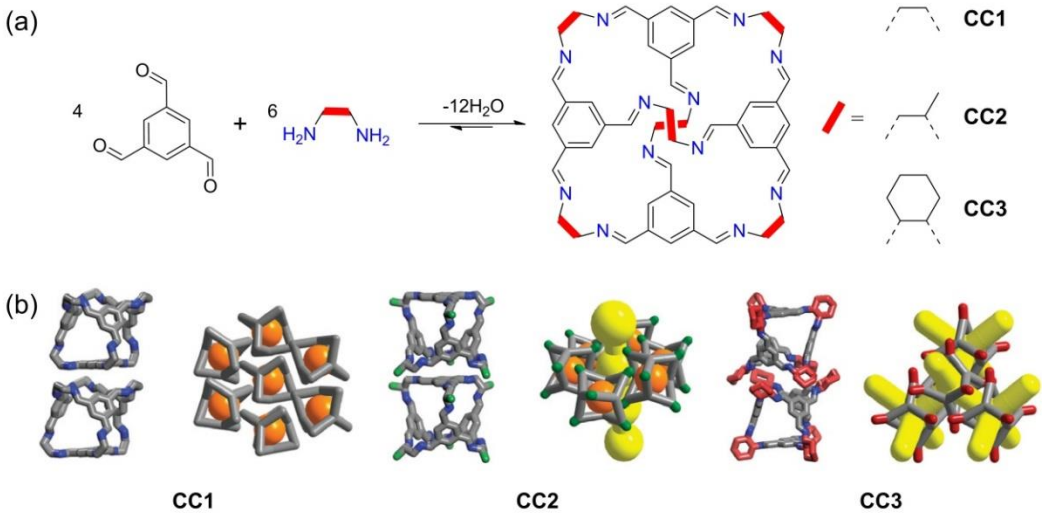

Figure 1.8 (a) Reaction scheme for the synthesis of cages **CC1** – **CC3**. (b) Schematic representation of cage-cage packing in the crystal structures of **CC1** – **CC3** resulting from a change in the vertex functionality.[61]

Building on this work, the use of different diamine precursors in conjunction with TFB led to a collection of POCs with distinct stoichiometries or properties. For example, Bojdys *et al.* showed that the introduction of bulky aryl groups onto the cage vertices frustrated the molecular packing and created additional extrinsic porosity.[62] One of these cages, **CC9**, possessed an improved BET surface area, in comparison to **CC3**, of 854 m^2 g^{-1}. In another study using complementary experimental and computational modelling studies, Jelfs *et al.* found that with increasing chain length of alkane diamine precursors, an odd-even effect with respect to the formation of either a [2+3] or [4+6] cage molecule was observable.[63]

Alteration of the trialdehyde precursor has also proven to have an impact, providing examples of some of the biggest cage molecules reported to date. The reaction of tri(4-formylphenyl)amine with (*R*,*R*)-1,2-cyclopentanediamine gave the [4+6] cage **CC5**, which was found to have a BET surface area of 1333 m^2 g^{-1}.[64] On the other hand, by changing the diamine to (*R*,*R*)-1,2-cyclohexanediamine, an [8+12] cage, **CC7**, was isolated (Figure 1.9).[65] However, **CC7** was found to collapse upon

desolvation and was therefore non-porous. This alternate behaviour was rationalised to be due to small differences in steric strain between the respective cage vertices, but it once again shows the importance of diamine choice in the synthesis of POC molecules.

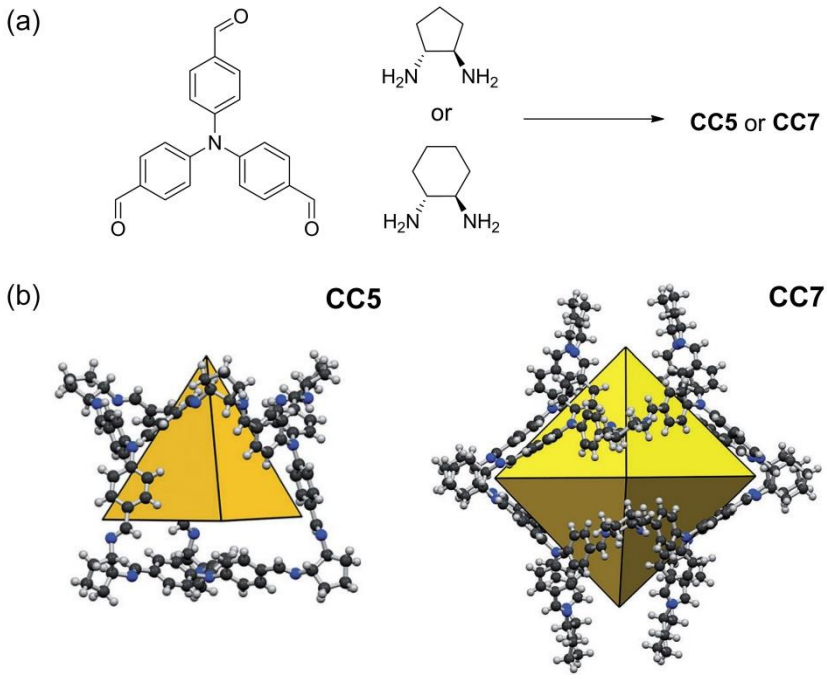

Figure 1.9 (a) Reaction scheme for the synthesis of **CC5** and **CC7**. (b) Single crystal X-ray structures of **CC5** (left) and **CC7** (right).[65]

CC3 has been repeatedly studied and utilised in many publications by the Cooper group over the past few years. In 2011, Jones *et al.* showed that by combining solutions of opposing cage enantiomers, highly porous crystalline solids could be prepared in a modular fashion *via* chiral recognition.[64] For example, **CC3**-*R* could be mixed together with **CC1**, **CC3**-*S* or **CC4**-*S* to give porous racemic materials with BET surface areas of up to 980 m^2 g^{-1}. This concept was later extended by Hasell *et al.* from a binary to a ternary system.[66] Hasell *et al.* also investigated the effect of precipitation rate upon particle size and morphology, and hence the gas sorption properties, of different cage racemates, including **CC3**-*R*/**CC3**-*S*.[67] It was found that by varying the rate or temperature of mixing, fine control over particle size could be achieved. The most rapidly precipitated samples also showed enhanced gas sorption properties, with BET surface areas of up to 1000 m^2 g^{-1} being attained for these heterochiral systems. This observation was rationalised as being due to an increase in the amorphous character of the material. By running a control experiment on

homochiral **CC3**-*R* to investigate the influence of precipitation rate on the degree of crystallinity, it was demonstrated in this case that there is a direct link between surface area and the degree of crystallinity, with highly crystalline **CC3** exhibiting a BET surface area of 409 m^2 g^{-1}. Therefore, the introduction of amorphous character into these cage materials can result in an increase in the number of defects due to inefficient cage packing, and hence an increase in surface area.

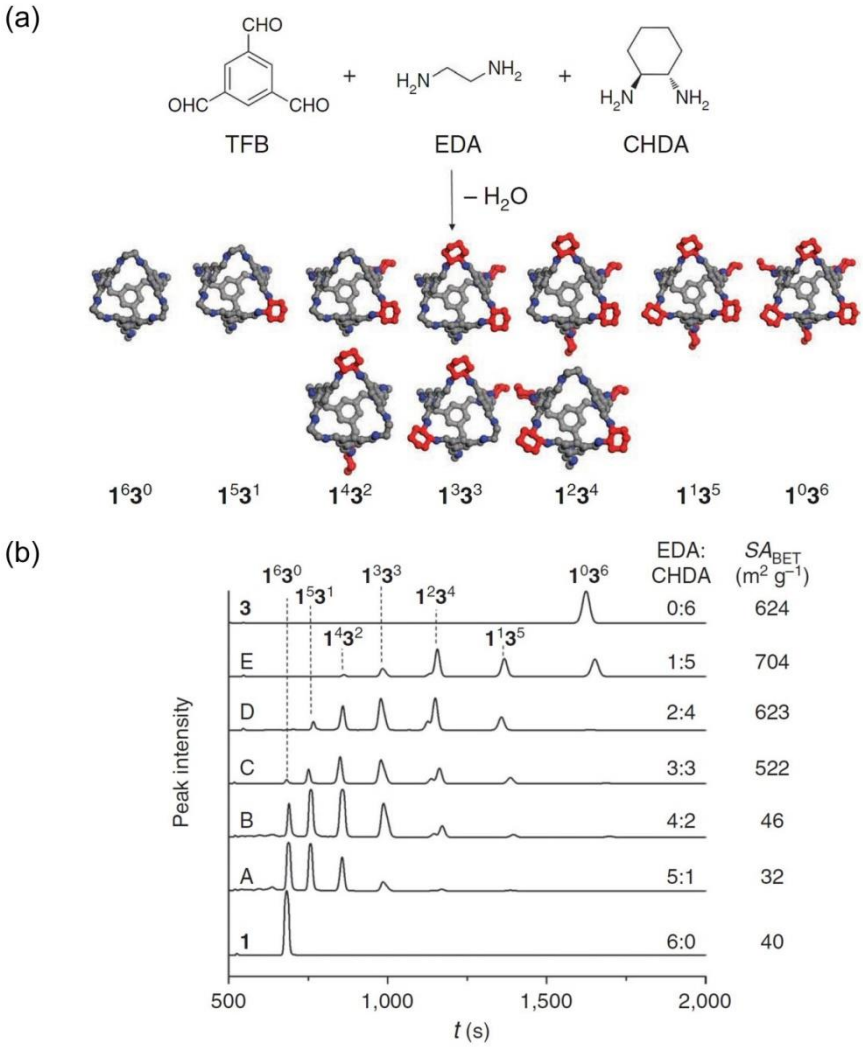

Figure 1.10 (a) Synthesis of scrambled cage products by reaction of TFB with two different diamines. (b) Analytical high-performance liquid chromatography (HPLC) data to show the equilibrium distribution of products resulting from the use of different diamine ratios and the associated BET surface areas.[68]

This phenomenon was exploited by Jiang *et al.*, who revealed that an equilibrium distribution of POC molecules with mixed vertex functionalities could be produced by reacting different ratios of EDA and CHDA with TFB.[68] Depending on the ratio used, up to seven cage products ranging in vertex functionality, from pure **CC1** to

CC3, could be observed by analytical HPLC. The resultant mixture comprised of POC molecules of different shapes which packed inefficiently in the solid state, resulting in higher BET surface areas of up to 704 m^2 g^{-1} being observed upon isolation (Figure 1.10).

These findings highlight the ease with which the properties of **CC3** can be tailored. Furthermore, exploiting the ability of **CC3** to dissolve in chlorinated solvents, as well as its structural stability and defined 3-D diamondoid pore network, has important implications with regards to its use in applications, including separations and the formation of composite materials. The interconnected 3-D diamondoid pore network of **CC3** has proven extremely important in several studies. Hasell *et al.* showed that both iodine and osmium tetroxide guest molecules could be sublimed into the pore structure and subsequently stabilised.[69] The pore structure was also shown by Mitra *et al*. to facilitate the separation of mesitylene from its C9 structural isomer 4-ethyltoluene with total specificity.[70] Using a chromatography column packed with **CC3** crystals, fractions from breakthrough measurements demonstrated that mesitylene eluted immediately, whereas 4-ethyltoluene was retained in the pore structure. This observation was reaffirmed by gas chromatography analysis and complementary computational simulations. Taking advantage of its solution processability, mixed-matrix membranes of **CC3** and PIM-1 were prepared by Bushell *et al.* through *in-situ* crystallisation of the POC molecules from a single homogeneous solution.[71] By dispersing **CC3** throughout the resulting membrane, its incorporation was determined to enhance the gas permeability, whilst retaining selectivity, and provided better resistance towards physical ageing. An alternative approach to exploit the solubility of **CC3** was conducted by Hasell *et al.*, where **CC3** was used to enhance the surface area and microporosity of macroporous inorganic supports.[72] Utilising the **CC3**-*R*/**CC3**-*S* racemate approach discussed above, its incorporation into macroscopic silica beads provided hierarchical porosity and the potential for use in chromatography or sensing. The solubility of **CC3** has also enabled it to be induced by a co-solvent to interchange its crystal packing mode (Figure 1.11). Upon slow evaporation of a solution of **CC3** in dichloromethane (DCM) and diethyl ether, crystals of **CC3** were isolated in which the cage molecules packed in a window-to-arene fashion (β-phase) in preference to the typical low-energy window-to-window packing mode (α-phase).[73] This change was due to

solvent loss causing the cages to pack in a more frustrated arrangement. Hasell *et al.* also demonstrated that the use of 1,4-dioxane could direct the crystal packing of POC molecules away from their lowest energy polymorphs, this time towards window-to-window packing in the formation of 3-D diamondoid pore networks.[74]

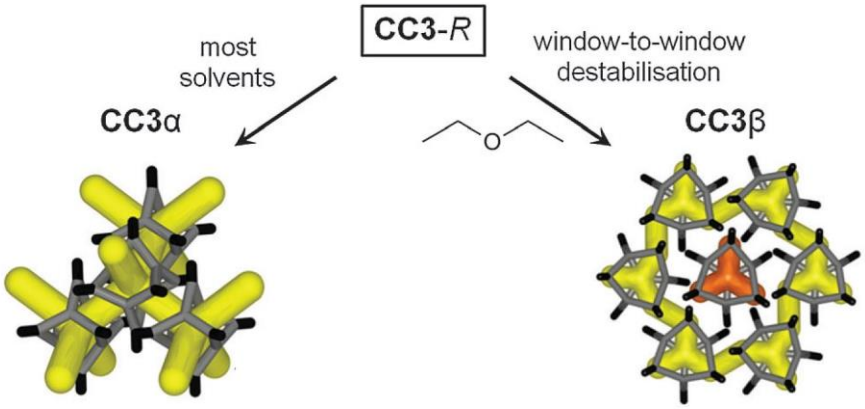

Figure 1.11 Schematic representation to show the crystal packing of **CC3** in its lower energy α-phase and destabilised β-phase.[73]

In 2008, Mastalerz reported the synthesis of an *endo*-functionalised [4+6] salicylbisimine cage compound formed *via* the cycloimination reaction of triptycene triamine and a salicyldialdehyde (**2a**, Figure 1.12).[56] Only in 2011, when its gas sorption properties were analysed, was it found to be highly porous, with a BET surface area of 1377 m^2 g^{-1}.[75] Upon crystallisation from hot dimethyl sulfoxide (DMSO), a second polymorph was found with an improved BET surface area of 2071 m^2 g^{-1}. In its reduced secondary amine form, this cage has been shown to be an ideal candidate as an affinity material, with its defined cavity size and shape enabling its use in the detection of aromatic solvent vapours upon deposition onto quartz crystal microbalances,[76] as well as in the detection of the drug γ-butyrolactone.[77]

This cage has also been shown to be easily modifiable. Schneider *et al.* investigated the influence of peripheral groups on the crystal packing and porosity by synthesising salicyldialdehydes with substituents of varying steric demand and successfully utilising them in POC synthesis (Figure 1.12).[78] In the crystalline state, and with increased peripheral bulk, the accessible BET surface area was found to substantially decrease. This was rationalised as being due to the molecules packing more tightly together and resulted in the pore windows becoming blocked. In the

amorphous state, the BET surface area values for each cage were roughly similar at around 700 m^2 g^{-1}, with the intrinsic cage cavity having a greater influence on the gas sorption properties. Alternatively, the introduction of various alkyl chains into the intrinsic cage voids *via* Williamson etherification of the interior hydroxyl groups resulted in "fine-tuning" of the pore structure, with the bulkier substituents taking up more space and corresponding to lower surface areas.[79]

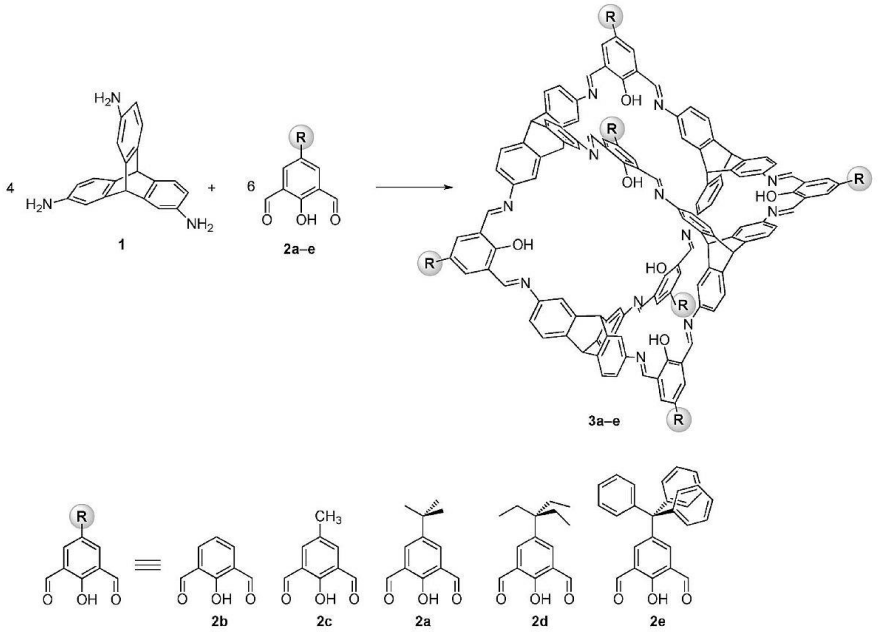

Figure 1.12 Reaction scheme for the synthesis of a series of periphery-substituted salicylbisimine cage compounds.[78]

Zhang and co-workers have synthesised a number of organic cages *via* imine bond formation, with the porous properties subsequently assessed. These shape-persistent 3-D prismatic organic cages are typically isolated as amorphous powders due to reduction to secondary amine architectures (Figure 1.13a). They have been shown to exhibit high CO_2/N_2 selectivities under ambient conditions (36/1 to 138/1, v/v) due to a combination of a well-defined cage structure and the strong interaction of CO_2 with the secondary amine groups.[80, 81] Microwave-assisted Sonogashira coupling of these cages using various diacetylene linkers gave organic-cage frameworks (OCFs) with improved CO_2/N_2 selectivity (213/1, v/v).[82] However, it should be noted that the actual gas uptakes are poor, and this is rationalised to be based on the presence of long hexyl chains which decrease the accessible pore volume. Interestingly, the introduction of thioether functionalities into the cage interior has allowed these

materials to be used in a functional manner; proving effective in the controlled synthesis of gold nanoparticles (Figure 1.13c,d).[83]

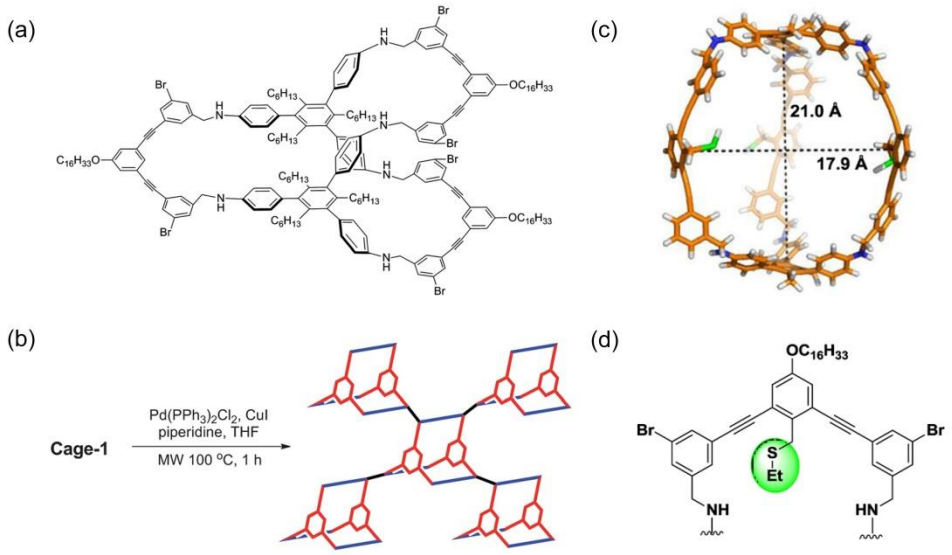

Figure 1.13 (a) Structure of a prismatic organic cage molecule.[80] (b) Reaction scheme for the synthesis of an OCF *via* Sonogashira coupling.[82] (c) The side view of an artificially inflated model of a thioether functionalised organic cage and (d) the position of the thioether functionality in the cage.[83]

Giri *et al.* designed and prepared a range of alkylated organic cages in the pursuit of porous liquid candidates.[84] From the reaction of (*R*,*R*)-1,2-bis(2-hydroxyphenyl)-1,2-diaminoethane and various aliphatic aldehydes, a range of alkyl-substituted vicinal diamines were synthesised *via* consecutive diaza-Cope rearrangement and acidic cleavage steps (Figure 1.14a). Although the alkyl tails could act as spacers in generating additional extrinsic porosity in the resulting POC materials, with the isohexyl cage possessing a BET surface area of 289 m^2 g^{-1}, the non-branched versions could also penetrate adjacent cage cavities; thus reducing the accessible surface area. Building on this work, using complementary experimental and computational studies, Melaugh *et al.* concluded that the introduction of bulky *tert*-butyl terminal branching groups prevented cage penetration, delivering a material which may be regarded as a liquid constituting of cages with empty intrinsic cavities.[85]

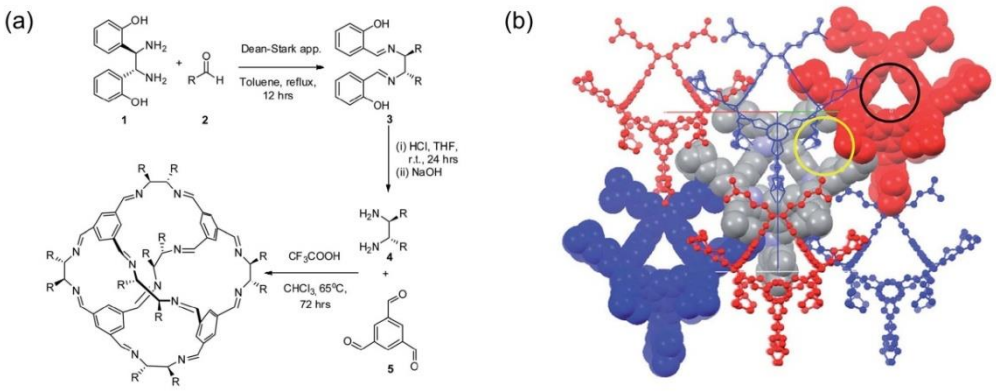

Figure 1.14 (a) Reaction scheme for the synthesis of a series of alkylated organic cages. R = *n*-hexyl, *n*-pentyl, isohexyl and *n*-octyl. (b) Crystal packing of an isohexyl cage showing internal and external cavities, which are circled in black and yellow respectively.[84]

Recently, Ding *et al.* reported the synthesis of a novel triazine-based [4+6] cage (Figure 1.15). Analysis of single crystals grown from a chloroform-DMSO solution showed that it had a large intrinsic cavity (2070 $Å^3$), which is greater than that of **CC5** (1356 $Å^3$). However, the cage loses its crystallinity upon activation through heating under vacuum due to the difficulty of removing the large DMSO molecules from the pore structure. Subsequent analysis of the cage in its amorphous state demonstrated that it possessed a BET surface area of 1181 $m^2\ g^{-1}$, which is still among the highest measured to date.

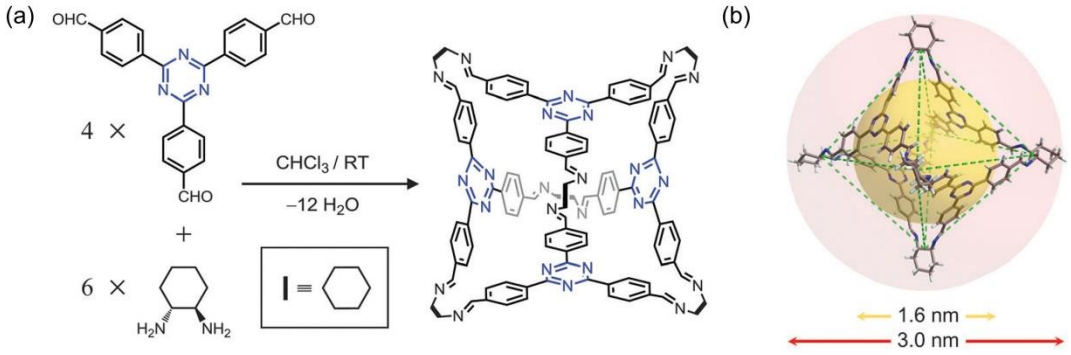

Figure 1.15 (a) Reaction scheme for the synthesis of a triazine-based [4+6] cage. (b) Crystal structure of the cage with yellow and red spheres to highlight the interior and exterior cage sizes respectively.[86]

Boronate Ester Bond-Based Cages

Boronate ester bond formation has previously been shown to be an effective method for preparing COFs, with its reversible and rigid nature enabling the isolation of crystalline materials.[16] Inspired by this, Zhang *et al.* synthesised a tetraol precursor which, when reacted with a triboronic acid, produced a [12+8] cage composed of 24 boronate ester bonds (Figure 1.16).[60] Upon activation by solvent swapping, the BET surface area was found to be 3758 $m^2 g^{-1}$, which is the highest reported for POC molecules to date. In addition, its internal cavity size was measured to be 2.3 nm, making it the first example of a mesoporous cage. By relocating the alkyl chains in the triptycene precursor from the 13- and 16- positions to the 9- and 10-bridgehead positions, an interlocked catenane structure was formed upon crystallisation from hexane.[87] This occurred due to the longer alkyl chains creating additional attractive dispersion interactions; thus promoting catenane formation. Two pores of varying size (1.4 nm and 2.0 nm) were inherent to the pore structure, with the BET surface area determined to be 1540 $m^2 g^{-1}$.

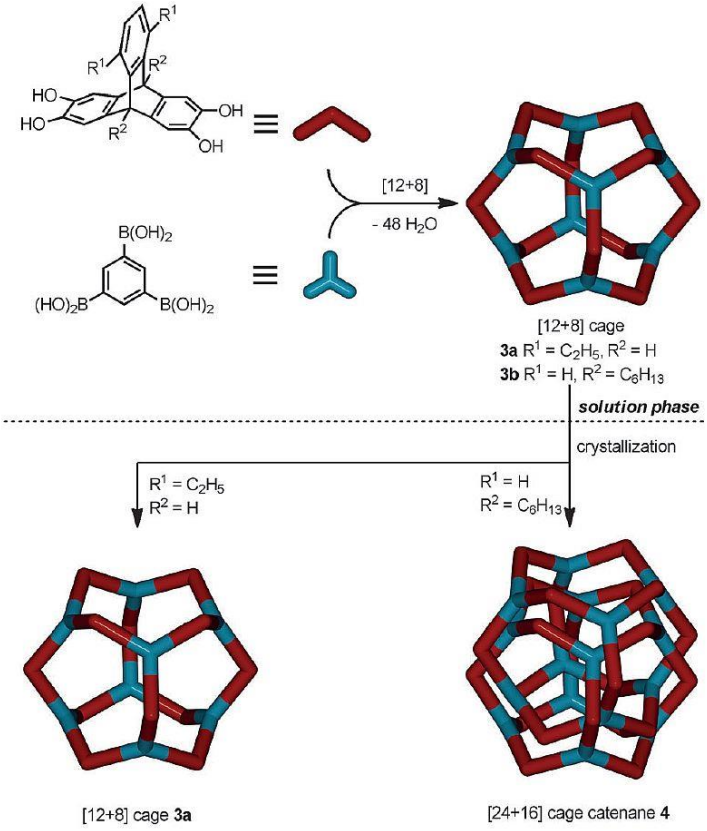

Figure 1.16 Reaction scheme to show the synthesis of the [12+8] boronate ester cage **3a** and the formation of the [24+16] cage catenane **4**.[87]

Another example based on this methodology was reported by Klotzbach *et al.*, where a large molecular cube was constructed from catechol-functionalised tribenzotriquinacene and a 1,4-phenylene diboronic acid.[88] Although isolated in high yield, the solvent could not be removed without promoting structural collapse, highlighting the importance of activation conditions in the retention of shape-persistence.

Carbon-Carbon Bond-Based Cages

Although coveted due to their rigidity and high chemical and thermal stabilities, historically, the synthesis of organic cage compounds based on carbon-carbon bonds has been held back by low overall yields due to their irreversible nature. However, by conducting a three-fold Eglinton homocoupling reaction between two rigid alkyne-terminated building blocks, Avellaneda *et al.* were able to synthesise a cage as the major product in 20 % yield (Figure 1.17).[89] Interestingly, upon rapid precipitation, a kinetically-trapped and crystalline porous polymorph was isolated with an excellent BET surface area of 1153 m^2 g^{-1}. Other cages based on this architecture have been prepared in higher yields, although they have not been evaluated for porosity.[90, 91] With alkyne metathesis emerging as an alternative dynamic covalent approach, there is further scope for other POCs to be constructed from carbon-carbon bonds and in improved yields.

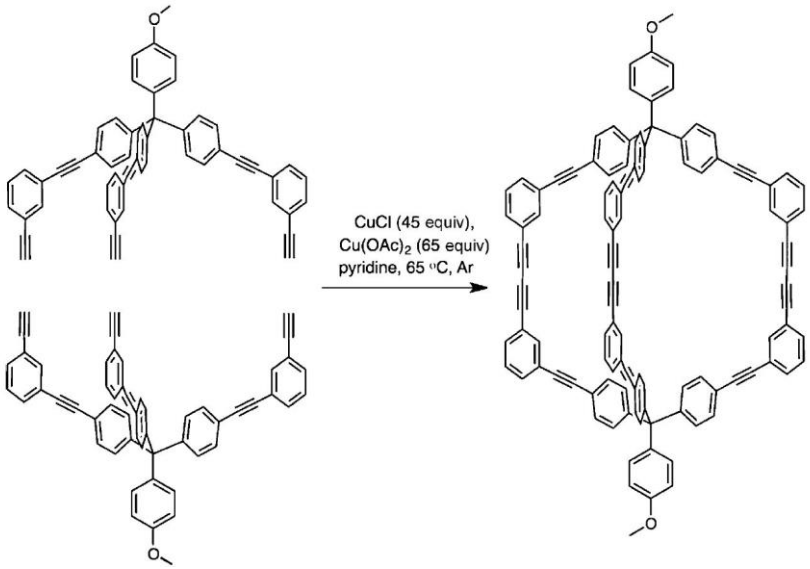

Figure 1.17 Reaction scheme for the synthesis of a carbon-carbon bond-based cage.[89]

1.4 Gas Separation using Porous Materials

Adsorption-based technologies for gas separation have developed rapidly over the past 30 years, potentially offering a more energy-efficient and environmentally-benign alternative in preference to more traditional approaches such as cryogenic distillation.[7] This rise in interest can be correlated with the development of MOFs, with their structural stabilities, high surface areas, controllable PSDs and adjustable chemical functionalities making them perfect candidates as selective adsorbents.[92] The ability to tune the properties of these materials has given rise to the study of a range of commercially relevant gas separations including, but not limited to: (i) CO_2 capture from gaseous mixtures;[93-95] (ii) propylene/propene;[96] (iii) hexane isomers;[97] (iv) xylene isomers;[98] and so on. Other amorphous porous materials such as PAFs[99] and HCPs[43] have also shown exceptional promise with regards to gas separation over more traditional porous materials such as zeolites, activated carbon, silica gel and metal-oxide molecular sieves for example.

According to Li *et al.*, gas separation *via* an adsorptive process is achieved based on a difference in the adsorption capability of different gaseous components in an adsorbent, where the performance is determined by the properties of the adsorbent with regards to both adsorption equilibrium and kinetics.[7] Most importantly, the adsorbent must exhibit both a good adsorption capacity and selectivity to be considered as a candidate for commercial applications. The successful separation of a mixture of gas molecules can be achieved in different manners. Firstly, size/shape exclusion (steric separation) is attained by preventing larger gas molecules from entering the pores and being adsorbed (e.g. separation of hydrocarbons). This is also known as the molecular sieving effect. Secondly, thermodynamic equilibrium separation is dependent on the preferential adsorption of one component over another (e.g. C_2H_2/CO_2 separation). The strength of this interaction is dictated by the respective properties of the adsorbate and adsorbent, including their polarisability or dipole-induced dipole interactions. Finally, kinetic separation is achieved based on a difference in the diffusion rates of the components in the pore channels, where the adsorbent's pore size must be finely-tuned between the diameters of the gas molecules in need of separating (e.g. N_2/CH_4 separation).[7]

A gas separation application that has been rarely explored is the separation of xenon (Xe) from krypton (Kr). Due to their similarity in size and shape, inert nature and very low concentrations in air, the separation of these noble gases has presented a difficult challenge for materials scientists. Interest in this application has therefore remained low, until recently, when the US Department of Energy began to sponsor research and development into alternative technologies for their successful capture and separation.[100]

1.5 The Separation of Noble Gases using Porous Sorbents and its Potential Application to the Nuclear Industry

Nuclear energy is an emission-free source of energy considered as a clean and affordable alternative to the use of non-renewable fossil fuels.[101] Despite this, there remain considerable safety concerns with this technology, one of which is the release of volatile and hazardous radionuclides. These include radioisotopes of the noble gases xenon (^{133}Xe) and krypton (^{85}Kr), which are generated during nuclear fission. They can enter the atmosphere as a consequence of nuclear accidents, such as the Fukushima Daiichi nuclear power plant catastrophe in Japan in 2011,[102] or in process off-gas streams during the reprocessing of used-nuclear fuel (UNF).

The motivations for reprocessing UNF are clear: to minimise the volume of radioactive waste and recover precious isotopes such as plutonium and uranium.[101] However, in countries such as Japan and Russia, the volatile radionuclides generated from this process are ultimately released into the atmosphere. In the US, there are no facilities for the reprocessing of UNF, but the storage of vast and ever-increasing amounts of nuclear waste across the country is no longer viewed as a long-term solution. Hence, for any future reprocessing facility in the US to meet strict licensing requirements, there needs to be an efficient and affordable technology implemented for the capture of these volatile radionuclides from the process off-gas streams.[100]

Various technologies for the capture and separation of Xe and Kr from process off-gas streams have been investigated, with the capture of ^{85}Kr, amongst other fission and activation products, garnering most attention due to its long half-life ($t_{1/2}$ = 10.8 years). An established method which has been previously examined for this purpose is cryogenic distillation, which is used commercially to separate low concentrations of Xe (0.087 ppmv) and Kr (1.14 ppmv) from air. This is

accomplished by utilising the differences in boiling points between the gases. In Japan, this technology has been shown to be feasible, with reported Kr decontamination factors (10 – 1000) which would be expected to meet the anticipated regulatory ^{85}Kr emission requirements.[103] On the other hand, this process is both energy-intensive and costly, as the Xe and Kr are only present in low concentrations, and presents an explosion hazard through the possible radiolytic formation of concentrated ozone. Moreover, optimum ^{85}Kr decontamination is not always achieved.[100] Alternatively, selective absorption can be utilised due to a difference in solubility between the targeted noble gases in a particular solvent. Using dichlorodifluoromethane (refrigerant-12), ^{85}Kr removal efficiencies of up to 99.9 % can be reached.[104] This approach offers low solvent and refrigeration costs, as well as a reduced explosion hazard, although operating and equipment costs are just as high as for cryogenic distillation. CO_2 absorption has also been considered but this process is strictly limited to gas streams with high CO_2 concentrations.[101]

Recently, there has been an increasing focus on the use of microporous materials for the separation of Xe and Kr from air, and from each other, under ambient conditions *via* selective physical adsorption. This offers the potential of savings in both energy consumption and cost. By the time the UNF is reprocessed, Xe will consist of only stable isotopes due to the short half-lives of its radionuclides (e.g. $t_{1/2}$ = 36.3 days for ^{127}Xe). However, in process off-gas streams, the concentration of Xe is around 10 times higher than Kr, thus the presence of Xe will impact on the capture of ^{85}Kr, the isotope of regulatory concern, by competing for adsorption sites.[105] Whereas ^{85}Kr needs to be isolated and stored before being potentially released into the atmosphere, the captured Xe is extremely valuable, and has several industrial applications ranging from lighting to medical devices. Therefore, if it can be separated efficiently from Kr, it could be potentially recovered for sale, in turn reducing the volume of noble gas waste.[101]

1.5.1 Xenon Adsorption in Activated Carbon and Zeolites

A cheap and commercially available porous sorbent, activated carbon was investigated early on for its ability to adsorb and separate noble gases. Munakata *et al.* studied its performance for binary-component gas mixtures (Kr-Xe and Kr-N_2) in the temperature range 77 – 323 K and found that its higher affinity for Xe

inhibited the adsorption of Kr.[106] This behaviour is unsurprising, as Xe is more polarisable than Kr and experiences a greater interaction with the pore surface; therefore occupying more adsorption sites. Despite boasting high surface areas and thermal and chemical stabilities, activated carbon is not presently considered to be a viable candidate for noble gas separation, as it poses a significant fire-risk due to the presence of incompatible NO_x in the process off-gas streams.

Alternatively, several commercially-available zeolites were studied by Jameson *et al.*[107] Utilising ^{129}Xe NMR spectroscopy and grand canonical Monte Carlo (GCMC) simulations, it was found that the zeolites NaA and NaX were selective for Xe over Kr, with selectivity values in the range 4 – 6 calculated using ideal adsorbed solution theory (IAST). The influence of silver (Ag) nanoparticle loading in zeolites has also been examined, as their presence has been hypothesised to polarise the noble gas atoms and enhance the adsorption capacity.[108-110] For example, a silver-exchanged zeolite, Ag-ETS-10, was shown to exhibit an enhanced Xe adsorption capacity, with high isosteric heats of adsorption observed in comparison to a sodium-exchanged zeolite Na-ETS-10.[111]

Although there have been advances regarding the ability to tune the porous properties of zeolites,[112] like activated carbon, they cannot match the reticular approach to the synthesis of MOFs, where the properties can be fine-tuned by constructing extended frameworks of novel chemical compositions, pore sizes and structural stabilities.

1.5.2 MOFs for the Capture and Separation of Xenon from Krypton

The applicability of MOFs was first reported by Mueller *et al.*,[113] where it was initially found that containers filled with IRMOF-1 had higher adsorption capacities for Xe and Kr compared to empty containers. A breakthrough system loaded with HKUST-1 was then shown to purify a 94:6 molar ratio of Kr and Xe to 99 % Kr, with less than 50 ppm of Xe remaining. Following this study, Thallapally *et al.* utilised Ni/DOBDC and revealed that it outperformed both activated carbon and IRMOF-1; achieving a higher Xe uptake (4.2 mmol g^{-1}, 55 wt %) and selectivity for Xe over Kr at room temperature.[114] These observations were rationalised based on the pore structure of Ni/DOBDC: a large number of open metal sites within uniform hexagonal pore channels (11 Å).[115] The only mechanism for Xe to interact with the

pore surface is through its polarisability and as metal cations are very polarising, they enhance the interaction with the noble gas. By comparison, activated carbon and IRMOF-1 contain no open metal sites.

To complement and aid these initial experimental studies, there have been a number of computational reports which have investigated the adsorption properties of both existing and hypothetical MOF structures in relation to noble gas separation.[116-119] These have provided valuable insights into deciphering the ideal framework structure for Xe/Kr separation that exhibits both high adsorption capacity and selectivity. Ryan *et al.* used GCMC simulations to screen a variety of well-known MOFs of varying topologies, pore sizes and metal atoms to determine the ideal structural characteristics required for Xe/Kr separation.[120] It was concluded that the presence of small pores with strong adsorption sites induced the desired adsorption of Xe over Kr, with MOF-505 found to exhibit the best combination of capacity and selectivity. Building on this work, Sikora *et al.* used high-throughput computational screening of 137,000 hypothetical MOFs to find that the best-performing materials for Xe/Kr separation contained tube-like pores which were just large enough to fit a single Xe atom.[121] They also determined that significantly improved materials remain to be synthesised and evaluated. These observations have also been supported through other computational approaches. Gurdal and Keskin used GCMC and equilibrium molecular dynamics (MD) simulations to calculate adsorption isotherms and self-diffusivities of Xe/Kr mixtures in ten different MOFs.[122] Those MOFs with the highest adsorption selectivities possessed narrow pores, which were found to promote stronger Xe confinement. By investigating the effect of open metal sites through running both experimental and simulation experiments on the *nbo*- and M/DOBDC series of MOFs, Perry *et al*. established that target structures should have a high density of metal sites with pore dimensions approaching the size of the gas of interest.[123]

One issue with some of these computational approaches is that the selectivities for thermodynamic mixture adsorption are typically calculated from single-component isotherms. When examining the capture of Xe and Kr from process off-gas streams, not only do you need to consider the presence of other gases (N_2, O_2, CO_2, Ar) competing for adsorption sites, but also their diffusion rates within the material.[118] This is of particular relevance to Xe/Kr separation, where Xe has a higher

polarisability but a lower diffusivity in comparison to Kr. While the thermodynamic effect is solely based on adsorbate-adsorbent interactions, the kinetic effect (i.e. diffusion rate) is determined by many factors, such as:[7] (i) the relationship between the size and shape of the adsorbate versus the size and shape of the adsorbent's pore; (ii) the strength of adsorption; (iii) the affinity of the adsorbate towards the adsorption site; (iv) the concentration of the adsorbed species, and; (v) the system temperature. Therefore, any experimental study needs to address both the thermodynamic and kinetic selectivities, whereby not only is the adsorption performance considered, but also the kinetic behaviour of the gas molecules within the material itself.

To satisfy this, Liu *et al.* used a dynamic breakthrough column method at room temperature to study Xe and Kr adsorption.[124] Two MOFs were selected due to their different pore morphologies (Figure 1.18). Ni/DOBDC had been previously shown to adsorb a large amount of Xe with selectivity over Kr.[114] With its uniform cylindrical pores and open metal sites, it satisfied some of the desired characteristics for Xe/Kr separation identified by simulation studies. Alternatively, HKUST-1 contains open metal sites but also has three different types of connected cavities: cages with dimensions of 11 Å and 13 Å, as well as small tetrahedral-shaped cavities with a diameter of 5 Å.[125] Using Xe/Kr mixtures of different compositions (80:20, 50:50 and 20:80), Ni/DOBDC was shown to outperform HKUST-1, as well as activated carbon, for all compositions. These results were rationalised on the basis of its pore structure. While the high density of open metal sites in Ni/DOBDC predisposed Xe to interact more strongly due to its higher polarisability and ensure a higher Xe/Kr selectivity, Ryan *et al.* found through simulation studies that both Xe and Kr prefer to adsorb in or around the small pockets of HKUST-1, leading to higher Kr uptakes in relation to Xe and therefore lower selectivities.[120] Liu *et al.* also ran breakthrough measurements for low concentrations of Xe (400 ppm) and Kr (40 ppm) in simulated air; thus mirroring the conditions that would be encountered in the reprocessing of UNF.[124] It was found that Ni/DOBDC could successfully separate ppm levels of Xe from Kr in air and achieved a selectivity of 7.3.

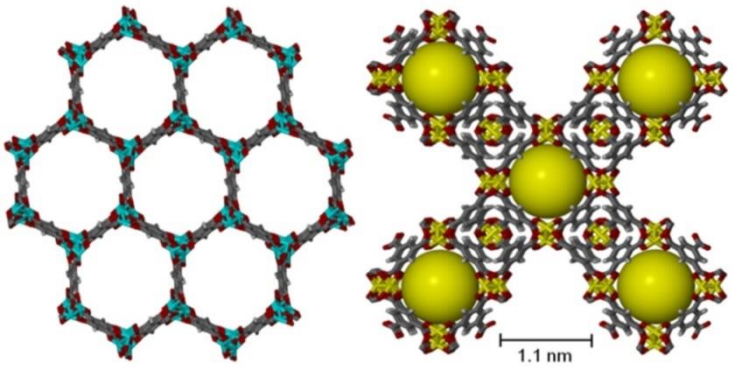

Figure 1.18 Crystal structures of Ni/DOBDC (left) and HKUST-1 (right) to illustrate their different pore morphologies.[124]

The influence of Ag nanoparticles, which enhanced Xe adsorption in Ag-loaded zeolites, was also investigated for Ni/DOBDC.[126] By fine-tuning the Ag-loading mass whilst retaining a high surface area, Ag@Ni/DOBDC had an improved Xe uptake capacity (70 wt %) and thermodynamic Xe/Kr selectivity (6.8) compared to the unadulterated Ni/DOBDC sample. This was rationalised based on the strong dipole-induced dipole interaction between the adsorbed Xe atoms and the Ag nanoparticles within the pores.

MOF-505 was previously identified by Ryan *et al*. to be a promising material for Xe/Kr separation due to its ideal combination of small pores and strong adsorption sites (Figure 1.19).[120] Bae *et al.* used breakthrough measurements to verify these computational predictions.[127] Conducted at room temperature using a Xe/Kr mixture (20:80) which is representative of the composition used industrially, MOF-505 was found to have a Xe/Kr selectivity of 9 – 10, which outperformed Ni/DOBDC and matched well with complementary simulation studies. It also exhibited a higher Xe uptake at 0.2 bar in comparison to Ni/DOBDC, with its superior properties attributed to the pore confinement effect of its small pores (4.8 Å, 7.1 Å and 9.5 Å) and its accessible metal centres serving as strong adsorption sites.[127] This study also highlighted how simulated and experimental measurements can deviate due to either inappropriate fittings used during the simulation studies, or through sample variability arising from the preparation and activation procedures. Therefore, a complementary approach between experimental and simulated measurements must be followed to maximise understanding of the desired properties required for Xe/Kr separation.

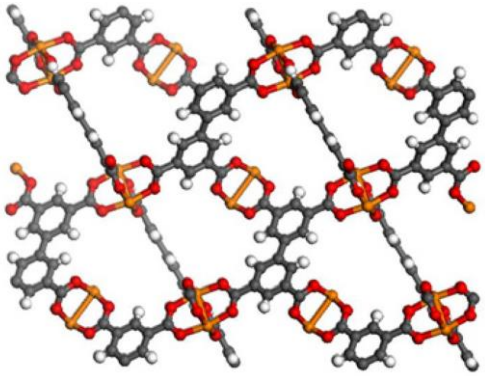

Figure 1.19 Framework structure of MOF-505.[127]

More recently, the microporous MOF $Co_3(HCOO)_6$, which contains 1-D channels of repeating zig-zag segments and a pore diameter of 5 – 6 Å, was found by Wang *et al.* to possess a high Xe adsorption capacity (2.0 mmol g^{-1}, 28 wt %) and Xe/Kr selectivity (6) when calculated from breakthrough experiments using a Xe/Kr mixture (10:90) at room temperature.[128] These observations were rationalised by simulations, whereby each Xe atom was found to fit within a segment and interact with the formate groups on the pore surface (Figure 1.20); this resulted in commensurate adsorption.[101] The introduction of different metals, including manganese and nickel, had no effect on the uptake and selectivity. This feature validates the findings of Perry *et al.*,[123] who demonstrated that changing the identity of the transition metal centre in the M/DOBDC series of MOFs[129] did not lead to any enhanced properties. This was due to the formal charge and the nature of the interaction remaining the same across the series.[101]

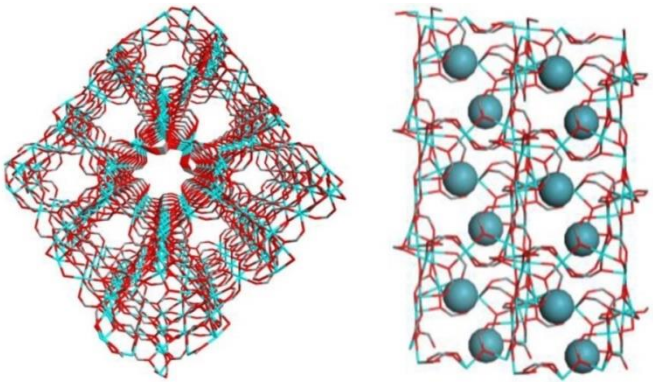

Figure 1.20 Top view of the $Co_3(HCOO)_6$ framework along the *b*-axis (left) and an image produced from the simulation of Xe adsorption at 298 K and 1 bar showing commensurate packing of Xe atoms (blue spheres) within the zig-zag channels (right).[128]

The selectivity can also be switched in favour of Kr by utilising MOFs with pore sizes small enough to promote a "molecular-sieving" effect.[118] FMOF-Cu comprises a pore structure containing tubular cavities (5.1 Å × 5.1 Å), along with bottleneck windows with estimated dimensions of 3.5 Å × 3.5 Å (Figure 1.21). Based on the respective diameters of Kr (3.69 Å) and Xe (4.10 Å), it would be expected that Kr would be selectively adsorbed over Xe (termed "reverse selectivity"). Indeed, at temperatures below 273 K, Fernandez *et al.* found that more Kr is adsorbed in comparison to Xe.[130] This behaviour was ascribed to a temperature-dependent gating effect, whereby the decreasing flexibility of the windows restricted the diffusion of Xe molecules inside the pore channels, with the kinetic effect outperforming the thermodynamic one. Alternatively, the selectivity can be switched in favour of Xe by raising the temperature above 298 K. This is due to the windows expanding and the gas molecules diffusing more readily, resulting in the thermodynamic effect becoming more dominant.

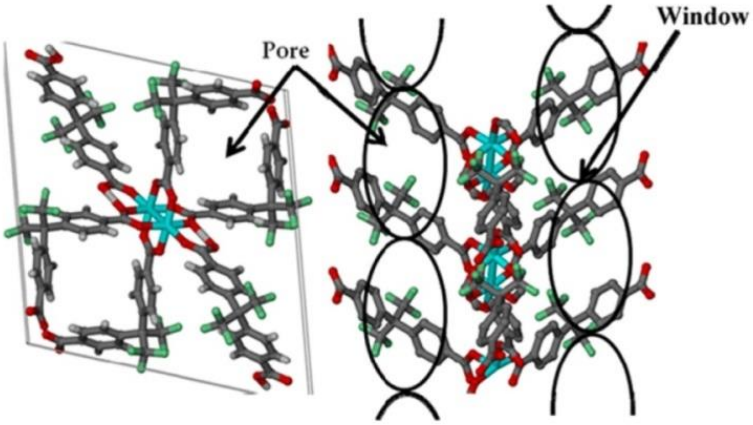

Figure 1.21 Crystal structure of FMOF-Cu.[101]

The ability of FMOF-Cu to selectively adsorb Kr over Xe led Liu *et al.* to develop a two-column method for the separation of Xe and Kr from process off-gas streams.[105] Using breakthrough measurements at 233 K and the same gas mixture of Xe (400 ppm) and Kr (40 ppm) in simulated air utilised in previous studies,[124] the Xe was initially removed selectively from the mixture stream by loading the first bed with Ni/DOBDC. By subsequently passing the left-over gas stream through a second bed containing FMOF-Cu, the removal efficiency and adsorption capacity for Kr was greatly improved, as it was no longer competing with Xe for adsorption sites.[105]

1.5.3 Outlook for Noble Gas Separation using Porous Sorbents

Of the porous materials discussed so far, MOFs have shown the greatest promise for the capture and separation of Xe and Kr from process off-gas streams during the reprocessing of UNF. Based on the experimental and computational studies published to date, according to Banerjee *et al.*, it has become clear that the ideal material for Xe/Kr separation should exhibit one or more of the following properties:[101] (i) a high concentration of open metal sites on the pore surface; (ii) narrow pores of uniform width which are large enough to accommodate a single Xe atom; (iii) contain polarised nanoparticles within the pore structure, and; (iv) facilitate the temperature-dependent separation of the gas mixture. Comparing the best performing materials to date also demonstrates that a high surface area is not essential for enhanced Xe/Kr selectivity (Table 1.1), although overall uptake is still important in terms of commercial applicability.

Table 1.1 Comparison of Xe uptake and Xe/Kr selectivity from breakthrough measurements (Xe/Kr, 20:80) at 298 K and 1 bar for selected porous materials.[128]

Material	SA_{BET} / $m^2\ g^{-1}$	Xe Uptake (298 K) / mmol g^{-1}	Xe/Kr Selectivity
Ni/DOBDC[114]	950	4.2	~ 4.0[124]
Ag@Ni/DOBDC[126]	750	~ 4.9	-
HKUST-1[124]	1710	3.2	2.6
FMOF-Cu[130]	58	~ 0.5	~ 2.0[a]
$Co_3(HCOO)_6$[128]	300	~ 2.0	6.0[b]
MOF-505[127]	1030	2.2*	9 – 10

[a]From breakthrough measurement (Xe/Kr, 50:50); [b]from breakthrough measurement (Xe/Kr, 10:90). *Xe uptake measured at 0.2 bar.

Finding a material that encompasses all of these aspects will prove challenging. Therefore, uniting both experimental and computational approaches will be important in the search for new and superior materials. Furthermore, investigations need not be limited to MOFs, with studies relating to POCs,[131] metallosupramolecular cages[132] and covalent-organic polymers[133] showing that there may be many other candidates suitable for the capture and separation of Xe and Kr.

1.6 Aims and Objectives

This thesis describes the synthesis and characterisation of novel porous organic cages, combined with an investigation of their gas sorption and separation properties. The structures of the prepared cages presented herein are based on the established porous organic cage **CC3**. Through synthetic modification of both the trialdehyde and diamine precursors, the gas sorption properties of the resultant cages can be finely-tuned, resulting in enhanced properties with respect to both gas storage and selectivity.

Chapter 3, *Synthesis of an Asymmetric Porous Organic Cage*, presents the preparation and utilisation of a derivative of the cage precursor triformylbenzene in the synthesis and isolation of a porous organic cage of reduced symmetry. Complementary gas sorption kinetics and molecular dynamics simulations demonstrate the potential of this cage for use in noble gas separation.

Chapter 4, *Synthesis of Periphery-Substituted Porous Organic Cages*, presents the preparation of enantiomerically-pure cyclohexanediamine derivatives and their successful utilisation in porous organic cage synthesis. The effect of introducing functional groups of varying steric and electronic characteristics on the gas sorption properties of the resulting cages is investigated, as well as a rare demonstration of the post-synthetic modification of an imine bond-based cage molecule. A large [8+12] cage molecule possessing bulky cage vertices was also successfully synthesised and characterised, with its shape-persistence and stability subsequently evaluated.

Chapter 5, *Separation of Xenon from Krypton using Porous Organic Cages*, presents the use of dynamic breakthrough measurements to assess the ability of porous organic cages to selectively separate Xe from Kr under conditions mimicking those experienced in the reprocessing of used-nuclear fuel.

1.7 References

1. R. E. Morris and P. S. Wheatley, *Angew. Chem.*, 2008, **47**, 4966-4981.
2. K. S. W. Sing, D. H. Everett, R. A. W. Haul, L. Moscou, R. A. Pierotti, J. Rouquérol and T. Siemieniewska, *Pure & Appl. Chem.*, 1985, **57**, 603-619.
3. L. J. Barbour, *Chem. Commun.*, 2006, 1163-1168.
4. A. Primo and H. Garcia, *Chem. Soc. Rev.*, 2014, **43**, 7548-7561.
5. J. Liu, P. K. Thallapally, B. P. McGrail, D. R. Brown and J. Liu, *Chem. Soc. Rev.*, 2012, **41**, 2308-2322.

6. L. J. Murray, M. Dinca and J. R. Long, *Chem. Soc. Rev.*, 2009, **38**, 1294-1314.
7. J.-R. Li, R. J. Kuppler and H.-C. Zhou, *Chem. Soc. Rev.*, 2009, **38**, 1477-1504.
8. J. Lee, O. K. Farha, J. Roberts, K. A. Scheidt, S. T. Nguyen and J. T. Hupp, *Chem. Soc. Rev.*, 2009, **38**, 1450-1459.
9. O. K. Farha, I. Eryazici, N. C. Jeong, B. G. Hauser, C. E. Wilmer, A. A. Sarjeant, R. Q. Snurr, S. T. Nguyen, A. Ö. Yazaydın and J. T. Hupp, *J. Am. Chem. Soc.*, 2012, **134**, 15016-15021.
10. H. Li, M. Eddaoudi, T. L. Groy and O. M. Yaghi, *J. Am. Chem. Soc.*, 1998, **120**, 8571-8572.
11. H. Li, M. Eddaoudi, M. O'Keeffe and O. M. Yaghi, *Nature*, 1999, **402**, 276-279.
12. M. Eddaoudi, J. Kim, N. Rosi, D. Vodak, J. Wachter, M. O'Keeffe and O. M. Yaghi, *Science*, 2002, **295**, 469-472.
13. H. Furukawa, U. Müller and O. M. Yaghi, *Angew. Chem. Int. Ed.*, 2015, **54**, 3417-3430.
14. H. Furukawa, N. Ko, Y. B. Go, N. Aratani, S. B. Choi, E. Choi, A. O. Yazaydin, R. Q. Snurr, M. O'Keeffe, J. Kim and O. M. Yaghi, *Science*, 2010, **329**, 424-428.
15. X. Feng, X. Ding and D. Jiang, *Chem. Soc. Rev.*, 2012, **41**, 6010-6022.
16. A. P. Côté, A. I. Benin, N. W. Ockwig, M. O'Keeffe, A. J. Matzger and O. M. Yaghi, *Science*, 2005, **310**, 1166-1170.
17. H. M. El-Kaderi, J. R. Hunt, J. L. Mendoza-Cortés, A. P. Côté, R. E. Taylor, M. O'Keeffe and O. M. Yaghi, *Science*, 2007, **316**, 268-272.
18. X. Ding, J. Guo, X. Feng, Y. Honsho, J. Guo, S. Seki, P. Maitarad, A. Saeki, S. Nagase and D. Jiang, *Angew. Chem. Int. Ed.*, 2011, **50**, 1289-1293.
19. C. R. DeBlase, K. E. Silberstein, T.-T. Truong, H. D. Abruña and W. R. Dichtel, *J. Am. Chem. Soc.*, 2013, **135**, 16821-16824.
20. N. B. McKeown, S. Makhseed and P. M. Budd, *Chem. Commun.*, 2002, 2780-2781.
21. N. B. McKeown and P. M. Budd, *Chem. Soc. Rev.*, 2006, **35**, 675-683.
22. P. M. Budd, E. S. Elabas, B. S. Ghanem, S. Makhseed, N. B. McKeown, K. J. Msayib, C. E. Tattershall and D. Wang, *Adv. Mater.*, 2004, **16**, 456-459.
23. M. Carta, P. Bernardo, G. Clarizia, J. C. Jansen and N. B. McKeown, *Macromolecules*, 2014, **47**, 8320-8327.
24. M. Carta, M. Croad, R. Malpass-Evans, J. C. Jansen, P. Bernardo, G. Clarizia, K. Friess, M. Lanč and N. B. McKeown, *Adv. Mater.*, 2014, **26**, 3526-3531.
25. C. R. Mason, L. Maynard-Atem, K. W. J. Heard, B. Satilmis, P. M. Budd, K. Friess, M. Lanč, P. Bernardo, G. Clarizia and J. C. Jansen, *Macromolecules*, 2014, **47**, 1021-1029.
26. M. Carta, R. Malpass-Evans, M. Croad, Y. Rogan, J. C. Jansen, P. Bernardo, F. Bazzarelli and N. B. McKeown, *Science*, 2013, **339**, 303-307.
27. J. X. Jiang, F. Su, A. Trewin, C. D. Wood, N. L. Campbell, H. Niu, C. Dickinson, A. Y. Ganin, M. J. Rosseinsky, Y. Z. Khimyak and A. I. Cooper, *Angew. Chem.*, 2007, **46**, 8574-8578.
28. Y. Xu, S. Jin, H. Xu, A. Nagai and D. Jiang, *Chem. Soc. Rev.*, 2013, **42**, 8012-8031.

29. G. Cheng, T. Hasell, A. Trewin, D. J. Adams and A. I. Cooper, *Angew. Chem.*, 2012, **51**, 12727-12731.
30. J.-X. Jiang, A. Trewin, D. J. Adams and A. I. Cooper, *Chem. Sci.*, 2011, **2**, 1777-1781.
31. P. Kuhn, M. Antonietti and A. Thomas, *Angew. Chem. Int. Ed.*, 2008, **47**, 3450-3453.
32. L. Chen, Y. Honsho, S. Seki and D. Jiang, *J. Am. Chem. Soc.*, 2010, **132**, 6742-6748.
33. J.-X. Jiang, Y. Li, X. Wu, J. Xiao, D. J. Adams and A. I. Cooper, *Macromolecules*, 2013, **46**, 8779-8783.
34. J.-X. Jiang, C. Wang, A. Laybourn, T. Hasell, R. Clowes, Y. Z. Khimyak, J. Xiao, S. J. Higgins, D. J. Adams and A. I. Cooper, *Angew. Chem. Int. Ed.*, 2011, **50**, 1072-1075.
35. T. Ben and S. Qiu, *CrystEngComm*, 2013, **15**, 17.
36. T. Ben, H. Ren, S. Ma, D. Cao, J. Lan, X. Jing, W. Wang, J. Xu, F. Deng, J. M. Simmons, S. Qiu and G. Zhu, *Angew. Chem.*, 2009, **48**, 9457-9460.
37. D. Yuan, W. Lu, D. Zhao and H. C. Zhou, *Adv. Mater.*, 2011, **23**, 3723-3725.
38. S. Xu, Y. Luo and B. Tan, *Macromol. Rapid Commun.*, 2013, **34**, 471-484.
39. J.-H. Ahn, J.-E. Jang, C.-G. Oh, S.-K. Ihm, J. Cortez and D. C. Sherrington, *Macromolecules*, 2006, **39**, 627-632.
40. B. Li, R. Gong, W. Wang, X. Huang, W. Zhang, H. Li, C. Hu and B. Tan, *Macromolecules*, 2011, **44**, 2410-2414.
41. R. Dawson, T. Ratvijitvech, M. Corker, A. Laybourn, Y. Z. Khimyak, A. I. Cooper and D. J. Adams, *Polym. Chem.*, 2012, **3**, 2034-2038.
42. R. Dawson, E. Stockel, J. R. Holst, D. J. Adams and A. I. Cooper, *Energy Environ. Sci.*, 2011, **4**, 4239-4245.
43. R. T. Woodward, L. A. Stevens, R. Dawson, M. Vijayaraghavan, T. Hasell, I. P. Silverwood, A. V. Ewing, T. Ratvijitvech, J. D. Exley, S. Y. Chong, F. Blanc, D. J. Adams, S. G. Kazarian, C. E. Snape, T. C. Drage and A. I. Cooper, *J. Am. Chem. Soc.*, 2014, **136**, 9028-9035.
44. J. Tian, P. K. Thallapally and B. P. McGrail, *CrystEngComm*, 2012, **14**, 1909.
45. J. R. Holst, A. Trewin and A. I. Cooper, *Nat. Chem.*, 2010, **2**, 915-920.
46. S. Lim, H. Kim, N. Selvapalam, K. J. Kim, S. J. Cho, G. Seo and K. Kim, *Angew. Chem.*, 2008, **47**, 3352-3355.
47. P. K. Thallapally, B. P. McGrail, J. L. Atwood, C. Gaeta, C. Tedesco and P. Neri, *Chem. Mater.*, 2007, **19**, 3355-3357.
48. J. Tian, P. K. Thallapally, S. J. Dalgarno, P. B. McGrail and J. L. Atwood, *Angew. Chem.*, 2009, **48**, 5492-5495.
49. J. D. Evans, C. J. Sumby and C. J. Doonan, *Chem. Lett.*, 2015, **44**, 582-588.
50. R. M. Barrer and V. H. Shanson, *J. Chem. Soc., Chem. Commun.*, 1976, 333-334.
51. P. Sozzani, S. Bracco, A. Comotti, L. Ferretti and R. Simonutti, *Angew. Chem.*, 2005, **44**, 1816-1820.
52. A. Comotti, S. Bracco, G. Distefano and P. Sozzani, *Chem. Commun.*, 2009, 284-286.
53. B. Kohl, F. Rominger and M. Mastalerz, *Org. Lett.*, 2014, **16**, 704-707.
54. R. G. D. Taylor, M. Carta, C. G. Bezzu, J. Walker, K. J. Msayib, B. M. Kariuki and N. B. McKeown, *Org. Lett.*, 2014, **16**, 1848-1851.
55. M. Mastalerz and I. M. Oppel, *Angew. Chem.*, 2012, **51**, 5252-5255.
56. M. Mastalerz, *Chem. Commun.*, 2008, 4756-4758.

57. S. J. Rowan, S. J. Cantrill, G. R. L. Cousins, J. K. M. Sanders and J. F. Stoddart, *Angew. Chem. Int. Ed.*, 2002, **41**, 898-952.
58. G. Zhang and M. Mastalerz, *Chem. Soc. Rev.*, 2014, **43**, 1934-1947.
59. Y. Jin, Y. Zhu and W. Zhang, *CrystEngComm*, 2013, **15**, 1484.
60. G. Zhang, O. Presly, F. White, I. M. Oppel and M. Mastalerz, *Angew. Chem. Int. Ed.*, 2014, **53**, 1516-1520.
61. T. Tozawa, J. T. A. Jones, S. I. Swamy, S. Jiang, D. J. Adams, S. Shakespeare, R. Clowes, D. Bradshaw, T. Hasell, S. Y. Chong, C. Tang, S. Thompson, J. Parker, A. Trewin, J. Bacsa, A. M. Slawin, A. Steiner and A. I. Cooper, *Nat. Mater.*, 2009, **8**, 973-978.
62. M. J. Bojdys, M. E. Briggs, J. T. A. Jones, D. J. Adams, S. Y. Chong, M. Schmidtmann and A. I. Cooper, *J. Am. Chem. Soc.*, 2011, **133**, 16566-16571.
63. K. E. Jelfs, E. G. B. Eden, J. L. Culshaw, S. Shakespeare, E. O. Pyzer-Knapp, H. P. G. Thompson, J. Bacsa, G. M. Day, D. J. Adams and A. I. Cooper, *J. Am. Chem. Soc.*, 2013, **135**, 9307.
64. J. T. A. Jones, T. Hasell, X. Wu, J. Bacsa, K. E. Jelfs, M. Schmidtmann, S. Y. Chong, D. J. Adams, A. Trewin, F. Schiffman, F. Cora, B. Slater, A. Steiner, G. M. Day and A. I. Cooper, *Nature*, 2011, **474**, 367-371.
65. K. E. Jelfs, X. Wu, M. Schmidtmann, J. T. A. Jones, J. E. Warren, D. J. Adams and A. I. Cooper, *Angew. Chem.*, 2011, **50**, 10653-10656.
66. T. Hasell, S. Y. Chong, M. Schmidtmann, D. J. Adams and A. I. Cooper, *Angew. Chem.*, 2012, **51**, 7154-7157.
67. T. Hasell, S. Y. Chong, K. E. Jelfs, D. J. Adams and A. I. Cooper, *J. Am. Chem. Soc.*, 2012, **134**, 588-598.
68. S. Jiang, J. T. A. Jones, T. Hasell, C. E. Blythe, D. J. Adams, A. Trewin and A. I. Cooper, *Nat. Commun.*, 2011, **2**, 207.
69. T. Hasell, M. Schmidtmann and A. I. Cooper, *J. Am. Chem. Soc.*, 2011, **133**, 14920-14923.
70. T. Mitra, K. E. Jelfs, M. Schmidtmann, A. Ahmed, S. Y. Chong, D. J. Adams and A. I. Cooper, *Nat. Chem.*, 2013, **5**, 276-281.
71. A. F. Bushell, P. M. Budd, M. P. Attfield, J. T. A. Jones, T. Hasell, A. I. Cooper, P. Bernardo, F. Bazzarelli, G. Clarizia and J. C. Jansen, *Angew. Chem.*, 2013, **52**, 1253-1256.
72. T. Hasell, H. Zhang and A. I. Cooper, *Adv. Mater.*, 2012, **24**, 5732-5737.
73. M. A. Little, S. Y. Chong, M. Schmidtmann, T. Hasell and A. I. Cooper, *Chem. Commun.*, 2014, **50**, 9465-9468.
74. T. Hasell, J. L. Culshaw, S. Y. Chong, M. Schmidtmann, M. A. Little, K. E. Jelfs, E. O. Pyzer-Knapp, H. Shepherd, D. J. Adams, G. M. Day and A. I. Cooper, *J. Am. Chem. Soc.*, 2014, **136**, 1438-1448.
75. M. Mastalerz, M. W. Schneider, I. M. Oppel and O. Presly, *Angew. Chem.*, 2011, **50**, 1046-1051.
76. M. Brutschy, M. W. Schneider, M. Mastalerz and S. R. Waldvogel, *Adv. Mater.*, 2012, **24**, 6049-6052.
77. M. Brutschy, M. W. Schneider, M. Mastalerz and S. R. Waldvogel, *Chem. Commun.*, 2013, **49**, 8398-8400.
78. M. W. Schneider, I. M. Oppel, H. Ott, L. G. Lechner, H. J. Hauswald, R. Stoll and M. Mastalerz, *Chem. Eur. J.*, 2012, **18**, 836-847.
79. M. W. Schneider, I. M. Oppel, A. Griffin and M. Mastalerz, *Angew. Chem.*, 2013, **52**, 3611-3615.

80. Y. Jin, B. A. Voss, A. Jin, H. Long, R. D. Noble and W. Zhang, *J. Am. Chem. Soc.*, 2011, **133**, 6650-6658.
81. Y. Jin, B. A. Voss, R. D. Noble and W. Zhang, *Angew. Chem.*, 2010, **49**, 6348-6351.
82. Y. Jin, B. A. Voss, R. McCaffrey, C. T. Baggett, R. D. Noble and W. Zhang, *Chem. Sci.*, 2012, **3**, 874.
83. R. McCaffrey, H. Long, Y. Jin, A. Sanders, W. Park and W. Zhang, *J. Am. Chem. Soc.*, 2014, **136**, 1782-1785.
84. N. Giri, C. E. Davidson, G. Melaugh, M. G. Del Pópolo, J. T. A. Jones, T. Hasell, A. I. Cooper, P. N. Horton, M. B. Hursthouse and S. L. James, *Chem. Sci.*, 2012, **3**, 2153.
85. G. Melaugh, N. Giri, C. E. Davidson, S. L. James and M. G. Del Pópolo, *Phys. Chem. Chem. Phys.*, 2014, **16**, 9422-9431.
86. H. Ding, Y. Yang, B. Li, F. Pan, G. Zhu, M. Zeller, D. Yuan and C. Wang, *Chem. Commun.*, 2015, **51**, 1976-1979.
87. G. Zhang, O. Presly, F. White, I. M. Oppel and M. Mastalerz, *Angew. Chem.*, 2014, **126**, 5226-5230.
88. S. Klotzbach, T. Scherpf and F. Beuerle, *Chem. Commun.*, 2014, **50**, 12454-12457.
89. A. Avellaneda, P. Valente, A. Burgun, J. D. Evans, A. W. Markwell-Heys, D. Rankine, D. J. Nielsen, M. R. Hill, C. J. Sumby and C. J. Doonan, *Angew. Chem.*, 2013, **52**, 3746-3749.
90. Q. Wang, C. Zhang, B. C. Noll, H. Long, Y. Jin and W. Zhang, *Angew. Chem. Int. Ed.*, 2014, **53**, 10663-10667.
91. C. Zhang and C.-F. Chen, *J. Org. Chem.*, 2007, **72**, 9339-9341.
92. M. O'Keeffe and O. M. Yaghi, *Chem. Rev.*, 2011, **112**, 675-702.
93. D. Britt, H. Furukawa, B. Wang, T. G. Glover and O. M. Yaghi, *Proc. Natl. Acad. Sci.*, 2009, **106**, 20637-20640.
94. J. Liu, J. Tian, P. K. Thallapally and B. P. McGrail, *J. Phys. Chem. C*, 2012, **116**, 9575-9581.
95. Z. Zhang, Y. Zhao, Q. Gong, Z. Li and J. Li, *Chem. Commun.*, 2013, **49**, 653-661.
96. Y. S. Bae, C. Y. Lee, K. C. Kim, O. K. Farha, P. Nickias, J. T. Hupp, S. T. Nguyen and R. Q. Snurr, *Angew. Chem.*, 2012, **51**, 1857-1860.
97. Z. R. Herm, B. M. Wiers, J. A. Mason, J. M. van Baten, M. R. Hudson, P. Zajdel, C. M. Brown, N. Masciocchi, R. Krishna and J. R. Long, *Science*, 2013, **340**, 960-964.
98. S. Mukherjee, B. Joarder, B. Manna, A. V. Desai, A. K. Chaudhari and S. K. Ghosh, *Sci. Rep.*, 2014, **4**, 1-7.
99. B. Li, Y. Zhang, R. Krishna, K. Yao, Y. Han, Z. Wu, D. Ma, Z. Shi, T. Pham, B. Space, J. Liu, P. K. Thallapally, J. Liu, M. Chrzanowski and S. Ma, *J. Am. Chem. Soc.*, 2014, **136**, 8654-8660.
100. N. R. Soelberg, T. G. Garn, M. R. Greenhalgh, J. D. Law, R. Jubin, D. M. Strachan and P. K. Thallapally, *Science and Technology of Nuclear Installations*, 2013, 1-12.
101. D. Banerjee, A. J. Cairns, J. Liu, R. K. Motkuri, S. K. Nune, C. A. Fernandez, R. Krishna, D. M. Strachan and P. K. Thallapally, *Acc. Chem. Res.*, 2015, **48**, 211-219.

102. S. R. Biegalski, T. W. Bowyer, P. W. Eslinger, J. A. Friese, L. R. Greenwood, D. A. Haas, J. C. Hayes, I. Hoffman, M. Keillor, H. S. Miley and M. Moring, *Journal of Environmental Radioactivity*, 2012, **114**, 15-21.
103. W. R. A. Goossens, G. G. Eichholz and D. W. Tedder, *Radioactive Waste Management Handbook, Vol. 2*, Harwood Academic Publishers, 1991.
104. D. K. Little, *Proceedings of the 17th DOE Nuclear Air Cleaning Conference, CONF-820833, US Department of Energy, The Harvard Air Cleaning Laboratory*, 1983.
105. J. Liu, C. A. Fernandez, P. F. Martin, P. K. Thallapally and D. M. Strachan, *Ind. Eng. Chem. Res.*, 2014, **53**, 12893-12899.
106. K. Munakata, T. Fukumatsu, S. Yamatsuki, K. Tanaka and M. Nishikawa, *Journal of Nuclear Science and Technology*, 1999, **36**, 818-829.
107. C. J. Jameson, A. K. Jameson and H.-M. Lim, *J. Chem. Phys.*, 1997, **107**, 4364.
108. L. Deliere, S. Topin, B. Coasne, J.-P. Fontaine, S. De Vito, C. Den Auwer, P. L. Solari, C. Daniel, Y. Schuurman and D. Farrusseng, *J. Phys. Chem. C*, 2014, **118**, 25032-25040.
109. C. Daniel, A. Elbaraoui, S. Aguado, M.-A. Springuel-Huet, A. Nossov, J.-P. Fontaine, S. Topin, T. Taffary, L. Deliere, Y. Schuurman and D. Farrusseng, *J. Phys. Chem. C*, 2013, **117**, 15122-15129.
110. R. Grosse, R. Burmeister, B. Boddenberg, A. Gedeon and J. Fraissard, *J. Phys. Chem.*, 1991, **95**, 2443-2447.
111. S. M. Kuznicki, A. Ansón, A. Koenig, T. M. Kuznicki, T. Haastrup, E. M. Eyring and D. Hunter, *J. Phys. Chem. C*, 2007, **111**, 1560-1562.
112. D. P. Serrano, J. M. Escola and P. Pizarro, *Chem. Soc. Rev.*, 2013, **42**, 4004-4035.
113. U. Mueller, M. Schubert, F. Teich, H. Puetter, K. Schierle-Arndt and J. Pastré, *J. Mater. Chem.*, 2006, **16**, 626.
114. P. K. Thallapally, J. W. Grate and R. K. Motkuri, *Chem. Commun.*, 2012, **48**, 347-349.
115. P. D. Dietzel, B. Panella, M. Hirscher, R. Blom and H. Fjellvag, *Chem. Commun.*, 2006, 959-961.
116. M. V. Parkes, H. Demir, S. L. Teich-McGoldrick, D. S. Sholl, J. A. Greathouse and M. D. Allendorf, *Microporous and Mesoporous Materials*, 2014, **194**, 190-199.
117. M. V. Parkes, C. L. Staiger, J. J. T. Perry, M. D. Allendorf and J. A. Greathouse, *Phys. Chem. Chem. Phys.*, 2013, **15**, 9093-9106.
118. T. Van Heest, S. L. Teich-McGoldrick, J. A. Greathouse, M. D. Allendorf and D. S. Sholl, *J. Phys. Chem. C*, 2012, **116**, 13183-13195.
119. S. T. Meek, S. L. Teich-McGoldrick, J. J. Perry, J. A. Greathouse and M. D. Allendorf, *J. Phys. Chem. C*, 2012, **116**, 19765-19772.
120. P. Ryan, O. K. Farha, L. J. Broadbelt and R. Q. Snurr, *AIChE J.*, 2011, **57**, 1759-1766.
121. B. J. Sikora, C. E. Wilmer, M. L. Greenfield and R. Q. Snurr, *Chem. Sci.*, 2012, **3**, 2217.
122. Y. Gurdal and S. Keskin, *Ind. Eng. Chem. Res.*, 2012, **51**, 7373-7382.
123. J. J. Perry, S. L. Teich-McGoldrick, S. T. Meek, J. A. Greathouse, M. Haranczyk and M. D. Allendorf, *J. Phys. Chem. C*, 2014, **118**, 11685-11698.
124. J. Liu, P. K. Thallapally and D. Strachan, *Langmuir*, 2012, **28**, 11584-11589.

125. Z. Hulvey, K. V. Lawler, Z. Qiao, J. Zhou, D. Fairen-Jimenez, R. Q. Snurr, S. V. Ushakov, A. Navrotsky, C. M. Brown and P. M. Forster, *J. Phys. Chem. C*, 2013, **117**, 20116-20126.
126. J. Liu, D. M. Strachan and P. K. Thallapally, *Chem. Commun.*, 2014, **50**, 466-468.
127. Y.-S. Bae, B. G. Hauser, Y. J. Colón, J. T. Hupp, O. K. Farha and R. Q. Snurr, *Microporous and Mesoporous Materials*, 2013, **169**, 176-179.
128. H. Wang, K. Yao, Z. Zhang, J. Jagiello, Q. Gong, Y. Han and J. Li, *Chem. Sci.*, 2014, **5**, 620-624.
129. S. R. Caskey, A. G. Wong-Foy and A. J. Matzger, *J. Am. Chem. Soc.*, 2008, **130**, 10870-10871.
130. C. A. Fernandez, J. Liu, P. K. Thallapally and D. M. Strachan, *J. Am. Chem. Soc.*, 2012, **134**, 9046-9049.
131. L. Chen, P. S. Reiss, S. Y. Chong, D. Holden, K. E. Jelfs, T. Hasell, M. A. Little, A. Kewley, M. E. Briggs, A. Stephenson, K. M. Thomas, J. A. Armstrong, J. Bell, J. Busto, R. Noel, J. Liu, D. M. Strachan, P. K. Thallapally and A. I. Cooper, *Nat. Mater.*, 2014, **13**, 954-960.
132. J. Roukala, J. Zhu, C. Giri, K. Rissanen, P. Lantto and V.-V. Telkki, *J. Am. Chem. Soc.*, 2015, **137**, 2464-2467.
133. Q. Wang, H. Wang, S. Peng, X. Peng and D. Cao, *J. Phys. Chem. C*, 2014, **118**, 10221-10229.

Chapter 2

Characterisation Methods

2.1 Gas Adsorption Theory and Measurements

Gas adsorption isotherms were used to characterise the porous properties of the POC molecules presented herein. For **CC14** and **CC16 – 19**, volumetric adsorption isotherms using N_2 gas were run to determine the surface areas and PSDs of both amorphous and crystalline samples, where appropriate. Other relevant gases (H_2 and CO_2) were also analysed, as well as Xe and Kr for **CC14**. Gravimetric adsorption isotherms for Xe and Kr for the powder samples of **CC1***β* and **CC3** were analysed in order to make direct comparisons with the uptake values obtained from previously run volumetric adsorption isotherms. Dynamic breakthrough measurements for samples of **CC1***β* and **CC3** in their pellet form were conducted to examine the ability of these porous materials to separate Xe from Kr at industrially-relevant concentrations.

2.1.1 Gas Adsorption Theory

The term adsorption is used to describe the process by which a molecule (the adsorbate) forms a bond to the surface (the adsorbent).[1] In the interests of this work, the adsorbate consists of gaseous molecules, while the adsorbent is a porous material consisting of discrete organic cage molecules. To characterise the properties of a particular porous material, gas adsorption measurements are used to determine its surface area, PSD and pore size.

Adsorption is a spontaneous and exothermic process and can be split into two categories: physisorption and chemisorption. In physisorption, no chemical bond is formed, with the interaction arising from weak van der Waals forces between the gas molecules and the surface. As the bonding is generally fragile, it tends to be a reversible process, with the adsorbate layer in equilibrium with the molecules of the gas phase.[1] All gases physisorb below their condensation temperature. On the other hand, chemisorption involves electron transfer, resulting in the formation of a true chemical bond between the adsorbate and the surface. This is distinguished from physisorption by its higher heat of adsorption. Whilst chemisorption is limited to the formation of a single layer (monolayer) of adsorbates on the surface, physisorption also allows the formation of multilayers, providing the pores of the material are large enough to facilitate this.

2.1.2 Langmuir Adsorption Model

There are two major models which describe the adsorption of gaseous molecules to a surface, the first of which is the Langmuir adsorption model.[2] The Langmuir isotherm is used to determine the total surface area, but applies only to monolayer adsorption and involves a number of assumptions which paradoxically may not be relevant to actual porous materials:[1]

1. All adsorption sites are equivalent and may be occupied by only one adsorbate molecule
2. A dynamic equilibrium exists between the molecules in the gas phase and the adsorbed layer
3. If an adsorbate molecule collides with a vacant adsorption site, it forms a bond with the surface, whereas if a filled site is struck, it is reflected back into the gas phase
4. Once adsorbed, the molecules are localised, with the interactions between other adsorbate molecules on adjacent sites discounted.

To determine the specific surface area using the Langmuir model (SA_{lang}), it must first be assumed that the molecules in the gas phase are in dynamic equilibrium with the surface:

$$M_{(g)} + S_{(surface\ site)} \rightleftharpoons M - S \qquad (2.1)$$

As this is an equilibrium process, the equilibrium constant K is a function of k_a and k_d, which are the rate constants for adsorption and desorption respectively:

$$K = \frac{k_a}{k_d} \qquad (2.2)$$

If N_s is the number of sites occupied by the adsorbate and N is the total number of surface adsorption sites (the monolayer capacity), the fractional coverage of the adsorbate is defined as:

$$\theta = \frac{N_s}{N} \qquad (2.3)$$

The rate of adsorption is dependent on the pressure P, as well as the fractional monolayer coverage of sites which are not occupied by adsorbate molecules ($1 - \theta$),

whereas the rate of desorption is independent of the pressure and depends only on the fractional monolayer coverage:

$$\text{Rate of adsorption} = k_a P(1 - \theta) \qquad (2.4)$$

$$\text{Rate of desorption} = k_d \theta \qquad (2.5)$$

Despite this alternate dependence, P does determine θ to an extent; hence, there is an "indirect" influence on the rate of adsorption. Therefore, at equilibrium, both the rate of adsorption and desorption are equal:

$$k_a P(1 - \theta) = k_d \theta \qquad (2.6)$$

Upon rearrangement, Equation 2.7 gives the Langmuir adsorption isotherm for associative adsorption, which predicts how the fractional monolayer coverage of the adsorbate changes with pressure. This may also be defined in terms of relative amounts or relative volumes, as well as the relative number of molecules:

$$\theta = \frac{N_s}{N} = \frac{n_a}{n_m} = \frac{V_a}{V_m} = \frac{KP}{1 + KP} \qquad (2.7)$$

where n_a is the amount of gas adsorbed, n_m is the amount of gas adsorbed corresponding to all adsorption sites being occupied in the monolayer, V_a is the volume of gas adsorbed at constant P and V_m is the volume of gas adsorbed at constant P corresponding to all adsorption sites being occupied in the monolayer.

The Langmuir equation can then be rewritten in the linear form as:

$$\frac{P}{n_a} = \frac{1}{n_m K} + \frac{P}{n_m} \qquad (2.8)$$

The plot of P/n_a against P will give a straight line of gradient $1/n_m$. The specific surface area can then be calculated using:

$$SA_{lang} = n_m L a_m \qquad (2.9)$$

where a_m is the cross-sectional area of one molecule and L is Avogadro's number ($6.022 \times 10^{23}\ \text{mol}^{-1}$).

2.1.3 Brunauer-Emmett-Teller (BET) Adsorption Model

The BET adsorption model is now widely applied to determine a material's surface area and other porous properties.[3] It overcomes the restriction of the Langmuir model by allowing for multilayer formation. Initial monolayer adsorption occurs with a fixed heat of adsorption, whilst subsequent multilayer formation differs significantly in value, as the strength of adsorbate-adsorbent bonds differs from that of adsorbate-adsorbate bonds. In accordance with a number of simplified assumptions, the Langmuir model can be applied to each adsorption layer to give the BET equation, which in its linear form is defined as:

$$\frac{P}{V(P_0 - P)} = \frac{1}{V_m C} + \frac{(C - 1)}{V_m C} \cdot \frac{P}{P_0} \qquad (2.10)$$

The adsorption of N_2 gas at 77 K and 1 bar is generally employed to determine the specific BET surface area (SA_{BET}) exhibited by a porous material. Using this in relation to Equation 2.10, P is the pressure of N_2 applied, P_0 is the saturated gas pressure of N_2 at 77 K, V is the total volume of N_2 gas adsorbed, V_m is the volume of gas adsorbed on the monolayer and C is a constant which takes account of the enthalpies of adsorption. Plotting $P/V(P_0 - P)$ against P/P_0 gives a linear plot, where values for the gradient $(C - 1)/V_m C$ and intercept $1/V_m C$ can be obtained. These values are used to determine V_m, the value of which is then utilised to calculate the total surface area:[4]

$$SA = \frac{a_m V_m L}{V_0} \qquad (2.11)$$

where a_m is the cross-sectional area of one molecule of N_2 (16.2×10^{-20} m^2), L is Avogadro's number (6.022×10^{23} mol^{-1}) and V_0 is the molar volume of N_2 gas (22.4 dm^3 mol^{-1}) at standard temperature and pressure.

The specific BET surface area can then be calculated by dividing this value by the mass of the adsorbent. It should be noted that the isotherm is only valid in the range $P/P_0 = 0.05 - 0.3$, as outside of this range it is not linear.

2.1.4 Gas Adsorption Isotherm Classification

The majority of physisorption isotherms can be classified into six different categories (Figure 2.1). Type I isotherms are reversible and typically correspond to the filling of micropores. This is demonstrated by a large gas uptake at low relative pressures, which then approaches saturation at higher relative pressures. The reversible Type II isotherm is generally obtained for macroporous adsorbents, where unrestricted monolayer-multilayer adsorption can occur.[5] Point B in Figure 2.1-II indicates the stage at which monolayer coverage is complete and multilayer adsorption begins. The Type III isotherm is also reversible. Behaviour of this type is relatively rare, with low gas uptake at low relative pressures indicating a weak interaction between the adsorbate and adsorbent. Type IV isotherms are characterised by a "hysteresis loop" and are typically observed for mesoporous adsorbents. At low relative pressures, it follows the same behaviour as the Type II isotherm. Conversely, larger volumes are adsorbed at higher relative pressures due to capillary condensation within the mesopores. The Type V isotherm is uncommon and difficult to interpret, whereas the Type VI isotherm represents stepwise multilayer adsorption, with each "step" corresponding to the completion of each separate monolayer.[1]

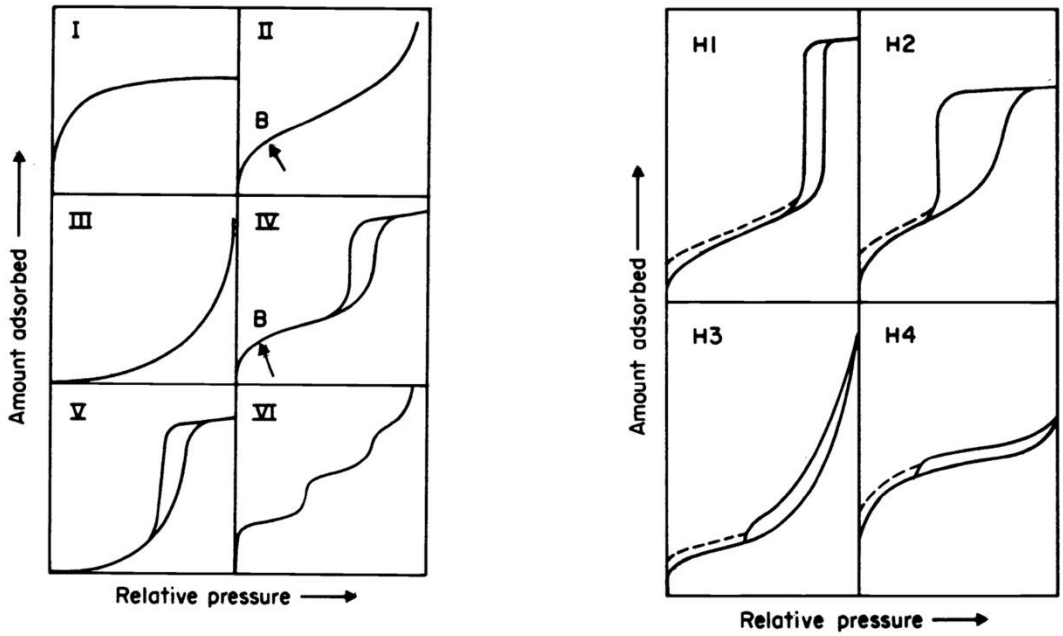

Figure 2.1 Illustrations to show the different types of physisorption isotherms (left) and hysteresis loops (right).[5]

Hysteresis is usually associated with capillary condensation in mesoporous adsorbents. It appears as a "loop" in the isotherm and may exhibit a variety of shapes (Figure 2.1). Type H1 is often related to porous materials with uniform and narrow PSDs, and is characterised by vertical adsorption and desorption curves which are almost parallel to one another.[5] On the other hand, Type H2 loops are typical of porous adsorbents where the distribution of pore size and shape is not uniform. Type H3 and H4 loops are observed for porous adsorbents with slit-shaped pores, with Type H4 often associated with narrow pores and hence microporous solids exhibiting a Type I adsorption isotherm.

2.1.5 Volumetric Gas Adsorption Measurements

Surface areas for all POC molecules were measured by N_2 adsorption at 77 K and 1 bar. Powder samples were degassed offline at 373 K for 15 hours under dynamic vacuum (10^{-5} bar) before analysis, followed by degassing on the analysis port under vacuum, also at 373 K. Isotherms were measured using Micromeritics 2020 or 2420 volumetric adsorption analysers. N_2 and H_2 isotherms were maintained at 77 K by liquid nitrogen cooling. Higher temperature isotherms for CO_2 (273 K) and Xe and Kr (298 K) required a circulating water chiller/heater to maintain the temperature. PSDs were derived from the adsorption branches of the isotherms using the non-local density functional theory (NL-DFT) model within the Micromeritics ASAP software. Xe kinetics measurements for **CC3** and **CC14** were performed using a Micromeritics 3flex surface characterisation analyser. Isotherms for **CC3** and **CC14**, using samples of the same mass, were recorded in parallel. By recording the decrease in pressure as a function of time, after dosing at equivalent pressure steps, a comparison between the samples could be made. All measurements were carried out using high purity gases: N_2 (N5.0: 99.999 % - BOC gases); H_2, CO_2, Xe and Kr (N5.5: 99.9995 % - BOC gases).

2.1.6 Gravimetric Gas Adsorption Measurements

Static Xe and Kr adsorption isotherms of the powder samples of **CC1***β* and **CC3** were performed gravimetrically using an Intelligence Gravimetric Analyser (IGA) from Hiden Instruments. Prior to analysis, the samples were degassed by heating at 413 K under vacuum for 10 hours. Both Xe and Kr adsorption isotherms were

measured at 298 K under IGA water bath control using the static mode. Pure Xe and Kr were purchased from OXARC, Inc. (Spokane, WA) and used as received.

2.1.7 Xe/Kr Breakthrough Measurements

To minimise pressure drop and prevent potential contamination of the main gas pipelines, pellet samples for each cage were formed following a two-step procedure. Firstly, a powder sample was pressed into a disk under 9 MPa for 3 minutes. The disk was then carefully broken up using a pestle and mortar and the fragments were sieved for 20 – 30 mesh (600 – 850 μm) pellets. The two-step procedure was repeated to make more pellets when necessary.

The Xe and Kr breakthrough curves were measured for **CC1***β* and **CC3** using a dynamic sorption analyser (ARBC, Hiden Analytical Ltd., Warrington, U.K.).[6] The 600 – 850 μm cage pellets were packed into an adsorption bed for the breakthrough experiments. With reference to the ARBC system illustrated in Figure 2.2, the gases were introduced through the bottom inlet of the adsorption bed. The adsorption bed was held between two layers of quartz wool and two sample holders, with frit gaskets installed at both the top and bottom ends of the adsorption bed to further prevent any potential powder contamination of the pipelines.

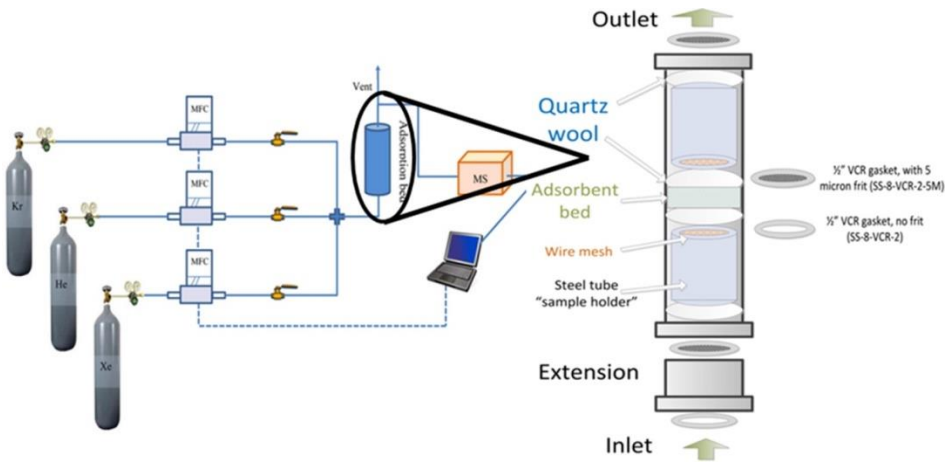

Figure 2.2 Apparatus for Xe/Kr breakthrough measurements.[7]

In a typical pure Xe or Kr breakthrough experiment, a gas mixture with a total flow rate of 20 sccm (standard cubic centimetres per minute) and a total pressure of 1 bar was flowed through the adsorption bed. For a Xe/Kr mixture breakthrough experiment, a total flow rate of 40 sccm and a total pressure of 1 bar were used. For

the separation of Xe (400 ppm) and Kr (40 ppm) in simulated air, a total flow rate of 40 sccm and a total pressure of 1 bar were used.

Prior to a specific sequence of breakthrough experiments for each cage, the pellet sample was degassed by heating at 413 K *in situ* under a He purge for 10 hours. In between breakthrough experiments, the sample was again purged with He, and the gas lines were purged with a gas mixture comprised of the same composition and total flow rate as that in the next measurement. The samples were then regenerated under a He purge at room temperature for 200 minutes and purged with He immediately before commencing the breakthrough experiment. This procedure was applied to all the samples tested. Dead volume and delay in the mass spectrometer signal were considered and deducted from the measured breakthrough capacities. The activated sample weight was determined immediately after unloading the sample and the ideal gas law was used to calculate the moles of gas adsorbed by the cage samples.[7]

Based on the mass balance, the gas adsorption properties can be determined as follows:

$$q = \frac{C_0 V t_s}{22.4 W} \qquad (2.12)$$

$$t_s = \int_0^t \left(1 - \frac{F}{F_0}\right) dt \qquad (2.13)$$

where t_s is the stoichiometric time (min), C_0 is the feed gas concentration, F_0 and F are the inlet and outlet gas molar flow rates respectively, q is the equilibrium adsorption capacity of gas (mmol g^{-1}), t is the adsorption time (min) which is from time zero to time when equilibrium is reached, V is the volumetric feed flow rate (cm^3 min^{-1}) at standard temperature and pressure (273 K and 1 atm) and W is the weight of the activated adsorbent (g).[6]

The respective dynamic capacities of Xe and Kr, determined using Equations 2.12 and 2.13, can be used to calculate the Xe/Kr selectivity using the standard definition:

$$S_{AB} = \frac{x_A / y_A}{x_B / y_B} \qquad (2.14)$$

where x_A and x_B are the mole fractions of gases A and B in the adsorbed phase and y_A and y_B are the mole fractions of gases A and B in the bulk phase.

Pure He, Xe and Kr were purchased from OXARC, Inc. (Spokane, WA) and used as received. The low concentration Xe (400 ppm) and Kr (40 ppm) mixtures in simulated air were also purchased from the same company and used as received.

2.2 X-ray Diffraction Theory and Measurements

X-ray diffraction is the most accurate method for characterising the structure of crystalline materials. In addition to providing information on the phase-purity of the material, it can precisely determine the atomic positions, bond lengths and bond angles of the molecules within the unit cell: providing an overall, average picture of a long-range ordered structure.[8] X-rays are a form of electromagnetic radiation with wavelengths in the range 0.01 nm to 10 nm, and are typically generated as a result of the impact of high-energy electrons with a metal target.[9]

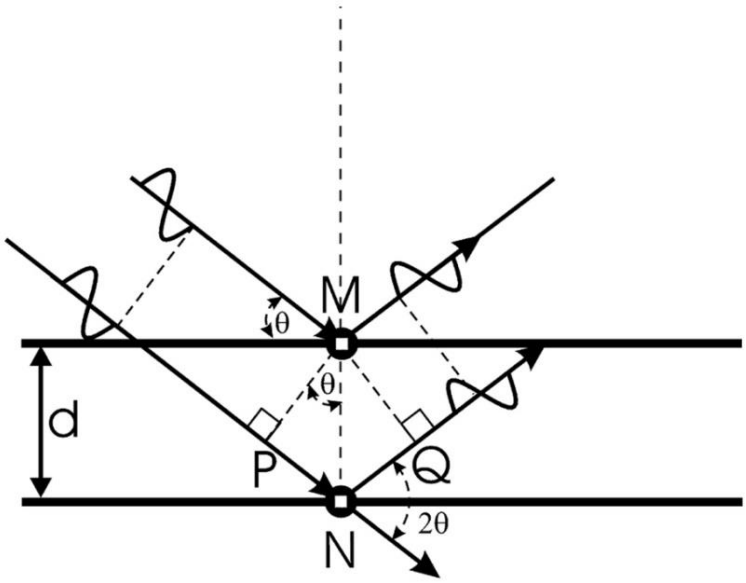

Figure 2.3 Illustration of Bragg diffraction.[10]

Crystalline solids consist of regular arrays of atoms, ions or molecules with characteristic interatomic spacings. Diffraction occurs when the wavelength of the X-ray is of the same order of magnitude as the interatomic spacing (Figure 2.3).[8] At specific orientations, X-rays are "reflected" from these atomic planes. The reflected beams may arrive in phase with one another, also known as constructive interference,

and for this to take place, the path lengths of the interfering beams must differ by an integral number of wavelengths.[8] This gives rise to the Bragg equation:

$$n\lambda = 2d\sin\theta \qquad (2.15)$$

where n is the number of wavelengths, λ is the wavelength, d is the spacing between the atomic planes and θ is the diffraction angle between incoming and outgoing X-ray beams.

Using Bragg's Law, the resulting diffraction pattern can be interpreted to provide information on the structural properties of the crystalline solid, including the size of the unit cell or its symmetry for example.

2.2.1 Single Crystal X-ray Diffraction (scXRD)

scXRD involves measuring the position and intensity of each reflection to precisely determine the unit cell dimensions, space group and positions of the atoms and chemical bonds.[8] The diffraction pattern generated is a transformation of the atomic structure into reciprocal space, with the 3-D distribution of atoms restored after transforming back into direct space *via* the application of a Fourier transform, whereby the atomic positions can be determined according to the distribution of electron density.[9] scXRD was used primarily to confirm the chemical structure and stoichiometry of cages **CC14**, **CC16**, **CC17** and **CC19**. In addition, where relevant, it enabled analysis of their solid state packing modes in order to help rationalise their respective gas sorption properties.

scXRD data sets for **CC14**, **CC16** and **CC19** were measured on a Rigaku MicroMax-007 HF rotating anode diffractometer (Mo-Kα radiation, λ = 0.71073 Å, Kappa 4-circle goniometer, Rigaku Saturn724+ detector), or, where specified, at Beamline I19, Diamond Light Source, Didcot, UK, using silicon double crystal monochromated radiation (λ = 0.6889 Å, Rigaku Saturn724+ detector).[11] scXRD data sets for **CC17** were measured on a Bruker D8 Venture Advance diffractometer equipped with IμS microfocus source (Cu-Kα radiation, λ = 1.54185 Å, Kappa 4-circle goniometer, Photon 100 detector). Empirical absorption corrections using equivalent reflections were performed with the program SADABS.[12] Structures were solved with SHELXD,[13] or by direct methods using SHELXS,[13] and refined by full-

matrix least squares on F^2 by SHELXL,[13] interfaced through the programme OLEX2.[14] In general, all non-H atoms were refined anisotropically. H atoms were fixed in geometrically estimated positions using the riding model.

2.2.2 Powder X-ray Diffraction (PXRD)

PXRD is a technique commonly employed in structure determination for assessing the phase-purity of solid state materials. A crystalline powder sample typically consists of a large number of crystallites, which are arranged in random orientations to one another. When an X-ray beam is applied, diffraction occurs from the atomic planes in those crystallites which are at the correct angle to fulfil the Bragg condition. This gives rise to a diffraction pattern which is plotted as intensity against 2θ.[8] PXRD patterns were used herein to qualitatively assess the degree of crystallinity exhibited by bulk samples of the respective POC molecules, as well as to confirm their phase purity in comparison to powder patterns simulated from scXRD analysis and crystal-structure prediction (CSP) methods.

PXRD data for **CC14** were collected on samples held between Scotch tape in transmission geometry on a Bruker D8 Advance diffractometer with Ge-monochromated Cu $K\alpha_1$ radiation and a LynxEye PSD. Spinning was enabled to improve particle statistics. Data were collected in the range $4° \leq 2\theta \leq 50°$ with a step size of 0.01° over 4 hours. Le Bail fitting was carried out using *TOPAS Academic*.[15]

PXRD data for **CC16** were collected using a Panalytical X'Pert PRO HTS X-ray diffractometer with Cu $K\alpha_1$ radiation. Samples were ground and mounted as a loose powder onto transparent film, with data collected in the range $4° \leq 2\theta \leq 50°$ with a step size of 0.013° over 1 hour.

For **CC19**, as the cage was potentially sensitive to guest loss, crystals were ground and dispersed in a minimal volume of crystallisation solvent before loading into borosilicate glass capillaries. Laboratory PXRD data were collected from the samples in transmission geometry on a Panalytical Empyrean diffractometer producing Cu $K\alpha_1$ radiation and equipped with an X-ray focussing mirror, using a PIXcel3D detector operating in 1-D scanning mode. Powder data were collected in the range $2° \leq 2\theta \leq 40°$ in steps of 0.013° over approximately 1 hour. This program was cycled to monitor any structural changes over a period of 4 hours. In the absence of

significant changes in diffraction, individual patterns were summed to generate a cumulative profile with improved counting statistics. The temperature of the capillary was controlled using an Oxford Cryosystems 700 Series Cryostream Plus.

2.3 Nuclear Magnetic Resonance (NMR) Spectroscopy

By dissolving an organic molecule in a particular deuterated solvent and placing the sample within a strong magnetic field, when irradiated with electromagnetic radiation of a certain frequency, energy is absorbed to produce resonance.[16] The NMR spectrum generated provides precise structural information on the molecule, including the chemical environment of individual nuclei and the types and numbers of equivalent nuclei present. ^{1}H and ^{13}C NMR spectroscopy were used to characterise and confirm the purity of all POC molecules, precursors and intermediates synthesised herein.

Solution ^{1}H and ^{13}C NMR spectra were recorded at 400.13 MHz and 100.6 MHz respectively using a Bruker Avance 400 NMR spectrometer. Chemical shifts are reported in ppm (δ) with reference to the internal residual protonated species of the deuterated solvent used for ^{1}H and ^{13}C analysis.

2.4 Fourier-Transform Infrared (FTIR) Spectroscopy

In FTIR spectroscopy, infrared radiation is passed through a sample, with some of the radiation being absorbed. The resulting spectrum contains absorption peaks which correspond to the characteristic vibrational frequencies of the chemical bonds which constitute the sample, therefore enabling analysis of its chemical structure. FTIR spectroscopy was used to characterise each of the POC molecules, as well as their precursors and intermediates.

IR spectra were recorded using a Bruker Tensor 27 FT-IR spectrometer with Quest ATR (diamond crystal puck) attachment running Opus 6.5 software. Samples were analysed as dry powders for 16 scans with a resolution of 4 cm^{-1}. Spectra were recorded in transmission mode.

2.5 Mass Spectrometry (MS)

MS involves the conversion of organic molecules into positively charged ions. The ions are sorted according to their mass-to-charge ratio (*m/z*) and their relative

amounts are then determined.[16] Chemical ionisation (CI) and electrospray ionisation (ESI) mass spectrometry were used to determine the accurate molecular weights of the POC precursors and their intermediates. Matrix-assisted laser desorption/ionisation time-of-flight mass spectrometry (MALDI-TOF MS) was used to determine the accurate molecular weight, as well as the stoichiometry, of each POC molecule.

CI mass spectra were recorded using an Agilent Q-TOF 7201. ESI mass spectra were recorded using a Micromass LCT-MS. MALDI-TOF MS was conducted using an AXIMA Confidence MALDI MS (Shimadzu Biotech) fitted with a 50 Hz N_2 laser. A 10:1 ratio of matrix/sample was dissolved in tetrahydrofuran (THF, 10 mg mL^{-1}) and this was drop-coated onto the microtitre plate before analysis. For **CC14** and **CC16**, the matrix used was dithranol. For **CC17** and **CC18**, the matrix used was *trans*-2-[3-(4-*tert*-butylphenyl)-2-methyl-2-propenylidene]malononitrile (DCTB).

2.6 Elemental (CHN) Analysis

Through the oxidation of an organic sample *via* combustion, CHN analysis enables the amounts of carbon, hydrogen and nitrogen present in the sample to be determined and provide information on its composition and purity. CHN analysis was used to confirm the structure and purity of novel cage precursors and POC molecules.

CHN analysis was conducted using a Thermo FlashEA 1112 Elemental Analyser. Samples were analysed as dry powders and the data was processed using dedicated elemental analysis software.

2.7 High-Performance Liquid Chromatography (HPLC)

HPLC is a form of column chromatography that can be used to separate, identify and quantify certain compounds. The constituents of a mixed sample can be separated based on differences between each compound's interaction with both the solid stationary and liquid mobile phases. This is represented by a difference in retention time, which is recorded by a suitable detector. In this thesis, both analytical and preparative HPLC were performed in the reverse phase (RP), which involves the use of a non-polar stationary phase and a polar mobile phase, whereby the compounds are separated based on their size and hydrophobic interactions.[17]

2.7.1 Analytical HPLC

Analytical HPLC was used to analyse both crude cage product mixtures and subsequently purified samples. Analysis was conducted using the Dionex Ultimate 3000 HPLC system. Analysis of mixed product samples of **CC3** and **CC14** was carried out using two Accucore RP-MS, 100 × 2.1 mm, 2.6 µm (SN 12163466BR6, Lot 11492) in series. The mobile phase was methanol at a flow rate of 0.5 mL min^{-1}. The injection volume was 1 µL and the sample concentration was *ca.* 1 mg mL^{-1} in chloroform. The column oven temperature was set to 30 °C. Detection for HPLC analysis was conducted at 254 nm. The column used for the analysis of pure samples of **CC14** was Syncronis C_8, 150 × 4.6 mm, 3 µm (SN 10136940, Lot 12459). The mobile phase was methanol at a flow rate of 0.5 mL min^{-1}. The injection volume was 5 µL and the sample concentration was *ca.* 1 mg mL^{-1} in chloroform. The column oven temperature was set to 30 °C. Detection for HPLC analysis was conducted at 254 nm. The column used for the analysis of both crude and purified product samples of **CC17** was Syncronis C_8, 150 × 4.6 mm, 3 µm (SN 10136940, Lot 12459). The mobile phase was methanol-water (10:90 to 90:10 over 27 minutes) at a flow rate of 0.5 mL min^{-1}. The injection volume was 2 µL and the sample concentration was *ca.* 1 mg mL^{-1} in DMSO. The column oven temperature was set to 30 °C. Detection for HPLC analysis was conducted at 254 nm.

2.7.2 Preparative HPLC

Preparative HPLC was utilised to isolate pure samples of **CC14** and **CC17**. It was conducted using the Shimadzu Prominence Preparative HPLC system. The column used for the purification of mixed product samples of **CC3** and **CC14** was Syncronis C_8, 150 × 30 mm, 5 µm (SN 10159851, Lot 12105). The mobile phase was methanol at a flow rate of 35 mL min^{-1}. The injection volume was 400 µL and the sample concentration was *ca.* 20 mg mL^{-1} in chloroform. The column oven temperature was set to 30 °C. Detection for HPLC analysis was conducted at 254 nm. The column used for the purification of crude product samples of **CC17** was Syncronis C_8, 150 × 30 mm, 5 µm (SN 10159851, Lot 12105). The mobile phase was methanol-water (10:90 to 90:10 over 9 minutes) at a flow rate of 35 mL min^{-1}. The injection volume was 600 µL and the sample concentration was *ca.* 20 mg mL^{-1} in

DMSO-methanol (2:1). The column oven temperature was set to 30 °C. Detection for HPLC analysis was conducted at 254 nm.

2.8 Scanning Electron Microscopy (SEM)

In SEM, an electron beam is scanned across a selected area of a solid sample's surface. The electrons penetrate the sample, with the interaction generating information, typically represented as a high-magnification image, concerning the topography of the sample, as well as enabling analysis of its crystalline structure and chemical composition.[18] SEM was used to characterise the morphologies of crystalline samples of **CC14** and **CC16**.

High resolution imaging of the crystal morphology was achieved using a Hitachi S-4800 Cold Field Emission Scanning Electron Microscope (FE-SEM). Scanning-mode samples were prepared by depositing dry crystals on 15 mm Hitachi M4 aluminium stubs using an adhesive high-purity carbon tab before coating with a 2 nm layer of gold using an Emitech K550X automated sputter coater. Imaging was conducted at a working distance of 8 mm and a working voltage of 3 kV using a mix of upper and lower secondary electron detectors. The FE-SEM measurement scale bar was calibrated using certified SIRA calibration standards.

2.9 Thermogravimetric Analysis (TGA)

TGA allows changes in the physical and chemical properties of materials to be measured as a function of increasing temperature (with constant heating rate) or as a function of time (with constant temperature). TGA was used to determine the change in water content of **CC17** upon exposure to air.

TGA was carried out using a Q5000IR analyser (TA instruments) with an automated vertical overhead thermobalance. The sample was heated under nitrogen at a rate of 5 °C min^{-1} up to 120 °C and the temperature was held isothermally for 1 hour. The sample was then cooled under either air or nitrogen down to 30 °C at a rate of 10 °C min^{-1}. The procedure was then repeated as appropriate.

2.10 References

1. G. Attard and C. Barnes, *Surfaces*, Oxford University Press, 1998.
2. I. Langmuir, *J. Am. Chem. Soc.*, 1916, **38**, 2221-2295.
3. S. Brunauer, P. H. Emmett and E. Teller, *J. Am. Chem. Soc.*, 1938, **60**, 309-319.
4. H. K. Livingston, *J. Am. Chem. Soc.*, 1944, **66**, 569-573.
5. K. S. W. Sing, D. H. Everett, R. A. W. Haul, L. Moscou, R. A. Pierotti, J. Rouquérol and T. Siemieniewska, *Pure & Appl. Chem.*, 1985, **57**, 603-619.
6. J. Liu, J. Tian, P. K. Thallapally and B. P. McGrail, *J. Phys. Chem. C*, 2012, **116**, 9575-9581.
7. J. Liu, P. K. Thallapally and D. Strachan, *Langmuir*, 2012, **28**, 11584-11589.
8. L. E. Smart and E. A. Moore, *Solid State Chemistry: An Introduction*, CRC Press: Boca Raton, Florida, 2005.
9. V. K. Pecharsky and P. Y. Zavalij, *Fundamentals of Powder Diffraction and Structural Characterization of Materials*, Springer: US, 2009.
10. R. E. Dinnebier and S. J. L. Billinge, *Powder Diffraction: Theory and Practice*, Royal Society of Chemistry: Cambridge, 2008.
11. H. Nowell, S. A. Barnett, K. E. Christensen, S. J. Teat and D. R. Allan, *J. Synchrotron Rad.*, 2012, **19**, 435-441.
12. G. M. Sheldrick, *University of Göttingen, Germany*, 2008.
13. G. M. Sheldrick, *Acta. Cryst. Sect. A*, 2008, **64**, 112-122.
14. O. V. Dolomanov, L. J. Bourhis, R. J. Gildea, J. A. K. Howard and H. Puschmann, *J. Appl. Cryst.*, 2009, **42**, 339-341.
15. A. A. Coehlo, *http://www.topas-academic.net*, 2007.
16. A. F. Parsons, *Keynotes in Organic Chemistry*, Blackwell Publishing: UK, 2003.
17. R. Malviya, V. Bansal, O. P. Pal and P. K. Sharma, *J. Glob. Pharm. Tech.*, 2010, **2**, 22-26.
18. K. D. Vernon-Parry, *III-Vs Review*, 2000, **13**, 40-44.

Chapter 3

Synthesis of an Asymmetric Porous Organic Cage

3.1 Introduction to Porous Organic Cage CC3

The POC molecule **CC3** was initially reported by the groups of Gawronski[1] and Cooper.[2] Its *R*-enantiomer is synthesised *via* the [4+6] cycloimination reaction of TFB with (*R*,*R*)-1,2-cyclohexanediamine (*R*,*R*-CHDA) and crystallises from a DCM solution in both high yield and purity as the most thermodynamically stable product. Possessing tetrahedral symmetry, the structure of **CC3** consists of a pre-fabricated inner cavity, as well as four open windows. In the solid state, it retains shape-persistency upon desolvation, with its α-phase packing in a window-to-window arrangement to generate a 3-D diamondoid pore network which passes through the intrinsic cage voids (Figure 3.1b).

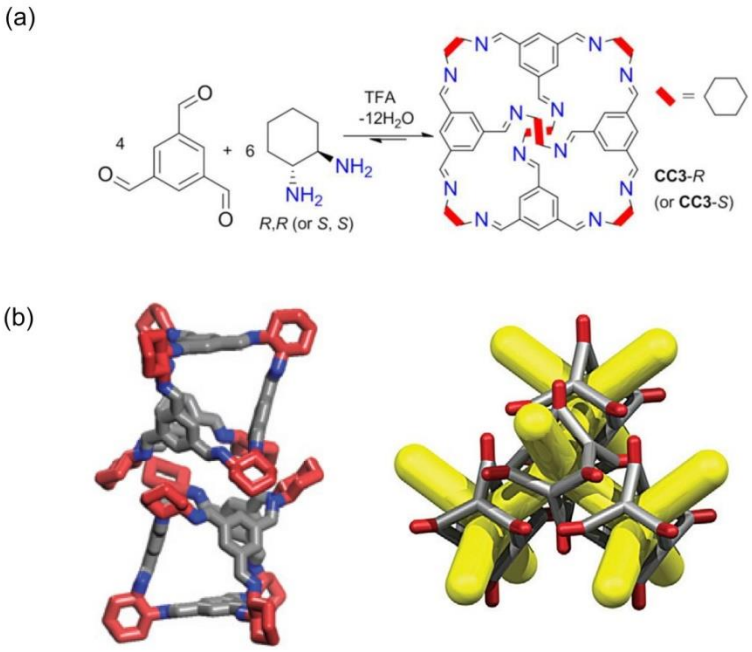

Figure 3.1 (a) Reaction scheme for the synthesis of **CC3**.[3] (b) Representation of the single crystal structure and packing arrangement of **CC3***α*, with a 3-D diamondoid pore network passing through the intrinsic cage voids (yellow – right).[2]

The inherent porosity leads to a high level of microporosity after desolvation, with an apparent BET surface area of 409 m^2 g^{-1} in its most crystalline form.[4] The interconnected micropore structure of **CC3***α* has recently been exploited for the separation of organic molecules based on solid state "shape-sorting"[5] and the selective separation of noble gases.[6] As with other POC molecules, **CC3** is solution processable and this characteristic has enabled it to be cast into composite membranes[7] and macroporous supports[8] or combined in a modular way to create

porous co-crystals.[9] In addition, **CC3** has been shown to be very stable, retaining its crystal packing arrangement, and without significant decomposition, even after being boiled in water for prolonged periods of time.[10]

CC3 has also been well-studied computationally through MD simulations, especially with regards to investigating the ability of small gas molecules to diffuse through the pore structure.[11] If each cage molecule is considered to be static, then the narrowest point in the 3-D pore structure, a circumcircle denoted as the pore-limiting diameter (PLD) and located between the cage and window cavities, has a value of 3.62 Å. According to Holden *et al.*, considering the kinetic diameter of N_2 is 3.64 Å, it could be argued that the pore channel needs to be wider than this in order to facilitate diffusion, in which case **CC3** should be formally non-porous to N_2.[12] However, gas sorption measurements have confirmed the ability of **CC3** to adsorb significant quantities of N_2 (4.50 mmol g^{-1}) at 77 K and 1 bar.[4] Alternatively, by allowing for the vibrational motion of the cage molecules, it was found that the flexibility of the host system resulted in a time-averaged, pore-limiting envelope (PLE), where the distribution of window sizes for the empty host ranged from 3.0 Å to 4.5 Å.[12] Using this model, the narrowest point in the 3-D pore structure was, for a calculable percentage of the simulated time period, wide enough to facilitate the diffusion of gas molecules such as N_2. In addition, larger gas molecules, such as Xe, which according to the static models should be much too big to pass through the cage windows, are able to diffuse between cage molecules *via* opportunistic hopping.

The synthesis of new POCs with precise control over pore size and topology is therefore of major interest, as it provides the opportunity to tailor the properties of these porous materials towards a specific application. Based on the relative success of **CC3**, synthesising derivatives of it in an isoreticular manner should impart new properties through tuning the dimensions of the 3-D diamondoid pore network.

3.2 Synthesis of a Methylated CC3 Derivative

The term isoreticular is defined as ‘based on the same net (having the same topology)’.[13] The concept of isoreticular porous materials was pioneered by Eddaoudi *et al.*, where an isoreticular series of MOFs, each possessing a molecular strut of varying length or functionality, was synthesised.[14] Variance of these struts led to porous materials ranging in pore size, gas uptake capability and density, whilst

preserving the same packing motif. Since then, many MOFs and COFs have been synthesised following these principles.[15-19] However, to date, an isoreticular series of POCs has not been successfully designed and synthesised, although certain POCs can be induced to display identical packing modes through the use of a directing solvent.[20] As POC molecules are discrete and interact together through a range of different supramolecular interactions, it is difficult to predict how they will pack in the solid state. In addition, small changes to the cage building blocks often preclude the formation of the cage, change the stoichiometry of the building blocks within the cage (for example, favouring '[8+12]' over '[4+6]' cages),[21] or change the way in which the cage molecules pack together in the solid state.

Another challenge in the area of POCs is the introduction of functionality that can be used to either tune properties or enable the material to be used for a secondary purpose. Amongst the best examples of the latter have stemmed from the Zhang group, where discrete molecular cages have been linked together *via* Sonogashira coupling to form OCFs[22] or functionalised with interior thioether groups for controlling the synthesis of gold nanoparticles.[23]

Our initial aim was to tune the porous properties of **CC3** by synthesising derivatives of its trialdehyde precursor TFB. The introduction of methyl groups into the TFB precursor offered the opportunity to narrow the dimensions of the pore windows, in conjunction with the cage molecules packing in an isoreticular manner to its parent cage **CC3**. This would also allow a direct comparison between the porous properties of the two cages and hence a greater understanding of their behaviour. The motivation for this was directed towards the separation of gas molecules of varying size. This is of relevance to the separation of noble gases, whereby the diffusion of larger gas molecules, such as Xe, through the pore network might be restricted, hence providing a greater degree of separation *via* a gating effect.[24]

The use of methyl and other alkyl groups to tailor microporosity has been previously reported for porous networks. Tilford *et al.* synthesised a series of alkyl substituted COFs using dialkyl substituted derivatives of 1,2,4,5-tetrahydroxybenzene as a precursor.[25] Altering the alkyl group from methyl to propyl resulted in a reduction in pore size from 18 Å to 11 Å respectively. This was also reflected in a significant drop in surface area. Although the N_2 uptake decreased, the H_2 uptake

(mol H_2/mol COF) actually increased upon introducing longer alkyl chains. This was rationalised by the ability of the smaller H_2 molecules to access pore corner cavities and adsorb onto the alkyl chains. In a similar vein, Ghanem *et al*. synthesised network-PIMs derived from triptycene monomers possessing different alkyl groups attached to their bridgehead positions.[26] The gas sorption properties could be tuned by varying the length and branching of the alkyl chain: methyl and isopropyl chains afforded materials with the highest surface area, while longer alkyl chains were found to significantly reduce the microporosity. Alternatively, Liu *et al.* studied the effect of methyl functionalisation on the capacity and binding energy for CO_2 adsorption in MOFs.[27] The introduction of the methyl groups resulted in a loss of surface area and pore volume. However, an enhanced CO_2 capacity was observed, and this was attributed to the methyl groups inducing stronger interactions between the framework and CO_2 molecules. This behaviour was confirmed by an increase in the isosteric heat of CO_2 adsorption. Other examples of MOFs have shown similar properties, where the loss of surface area has been compensated for by an increase in CO_2 uptake.[28, 29] Finally, Schneider *et al*. reported a series of POCs whose intrinsic voids had been post-synthetically modified through Williamson etherification.[30] The introduction of alkyl chains of varying size allowed the pore structures of the POCs to be "fine-tuned", with the bulkier substituents filling up more of the interior and corresponding to lower surface areas.

The methylated derivative of TFB, 1,3,5-trimethyl-2,4,6-tris(formyl)benzene (Me_3TFB), was chosen as a candidate for inclusion into a **CC3** analogue. Me_3TFB (**1**) was synthesised in a 69 % yield from 1,3,5-trimethyl-2,4,6-tris(bromomethyl)benzene *via* a modified Hass procedure (Scheme 3.1).[31, 32] Despite screening various conditions, the reaction of Me_3TFB with *R,R*-CHDA resulted in no cage species being detected. Only insoluble oligomeric by-products and unconsumed starting material were observed. This was rationalised on the basis of the steric hindrance of the methyl groups inhibiting the formation of a closed cage structure.

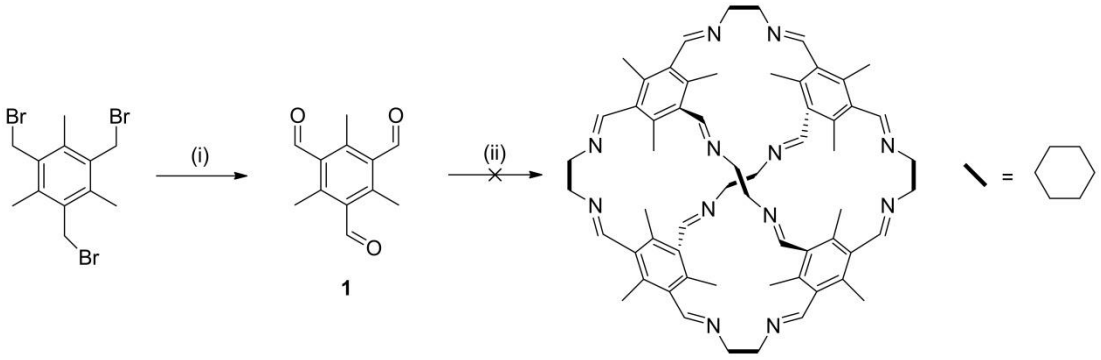

Scheme 3.1 Proposed reaction scheme for the synthesis of a methylated **CC3** derivative. Reaction conditions: (i) NaOMe, 2-nitropropane, CH_3OH, rt, 69 %. (ii) *R,R*-CHDA, solvent, rt.

To investigate this behaviour, different ratios of Me_3TFB and TFB were reacted with *R,R*-CHDA and the resulting product distribution analysed upon work-up by analytical HPLC. Our rationale was that introducing TFB would reduce the steric crowding and allow the formation of a mixed TFB/Me_3TFB cage product. This procedure was based on the method outlined by Jiang *et al.*, whereby TFB was reacted with two different diamines to give an equilibrium distribution of POC products with mixed vertex functionalities.[33] Of course, here the ratio of the trialdehydes was being altered instead of the diamines.

Table 3.1 Synthesis of cage mixtures by the reaction of *R,R*-CHDA with various ratios of TFB and Me_3TFB.

TFB: Me_3TFB	TFB	Me_3TFB	Yield / mg	Appearance
4:0	100 mg, 0.62 mmol	0 mg, 0 mmol	118	Powdery white solid
3:1	75 mg, 0.46 mmol	32 mg, 0.16 mmol	87	
2:2	50 mg, 0.31 mmol	63 mg, 0.31 mmol	61	Flaky yellow solid
1:3	25 mg, 0.15 mmol	94 mg, 0.46 mmol	93	

As outlined in Table 3.1, with an increasing amount of Me_3TFB, the appearance of the isolated product changed from a powdery white solid to a flaky yellow solid which displayed limited solubility. The reduced solubility of the latter samples, coupled with the yellow tinge, is indicative of the presence of oligomeric or polymeric by-products.

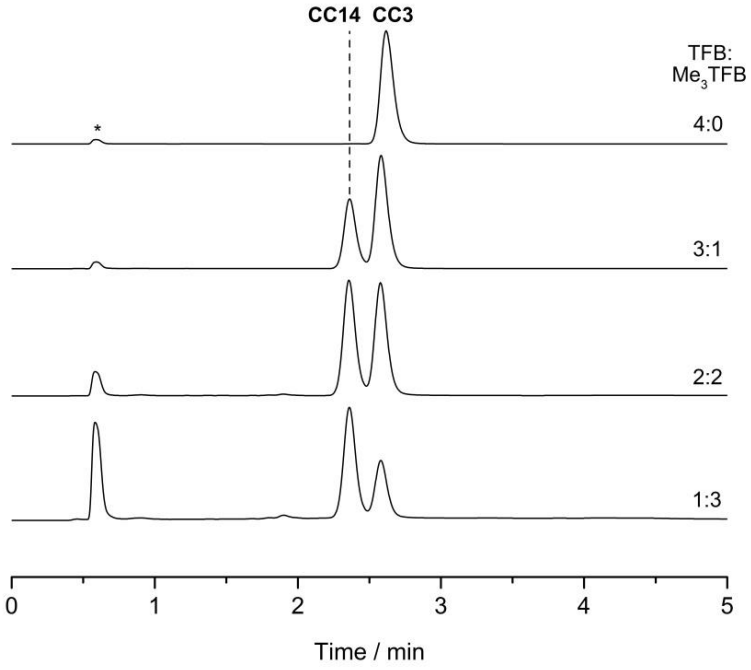

Figure 3.2 HPLC analysis for the cage product mixtures formed by the reaction of *R,R*-CHDA with various ratios of TFB and Me_3TFB. The peak intensities have been normalised to equal 0 – 1 for clarity. Column: 2 × Accucore RP-MS in series; 100 × 2.1 mm; 2.6 μm; mobile phase: isocratic CH_3OH; flow: 0.5 mL min^{-1}; detection: λ = 254 nm; oven temperature = 30 °C. *$CHCl_3$ solvent peak.

Analysis of the isolated products by analytical HPLC (Figure 3.2) showed the presence of only two components, one of which was identified as **CC3** (t_R = 2.58 min). This contrasts with the scrambling of the diamines, where all seven hypothetical cage species were obtained.[33] Since there is only one other peak at 2.36 min, and as the peak intensity for **CC3** decreases as the amount of Me_3TFB used increases, the additional cage species was theorised to be a cage containing three equivalents of TFB and one equivalent of Me_3TFB, denoted here as **CC14**. This indicates that only one Me_3TFB may be accommodated in a cage molecule; this is likely due to steric hindrance. It should be noted that the peak intensities have been normalised to better represent the relative amounts of each cage that has formed. This is because at higher Me_3TFB ratios, the amount of oligomeric and polymeric material in the isolated product increases, as cage formation is now more restricted. The peak intensities of both cage molecules in the HPLC trace are therefore much lower.

3.3 Isolation and Characterisation of the Asymmetric Cage CC14

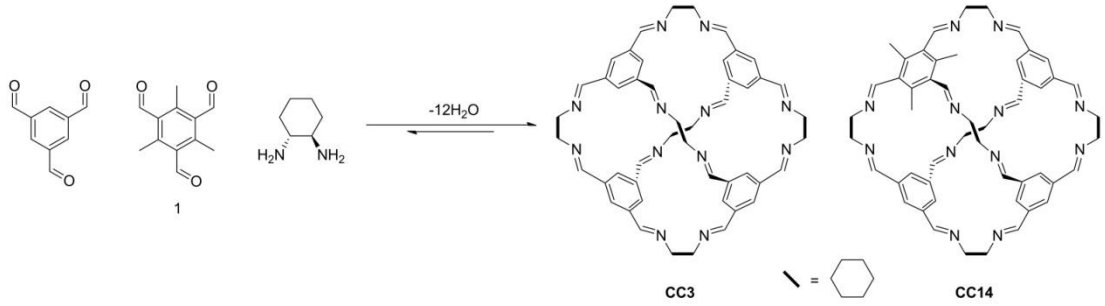

Scheme 3.2 Reaction scheme for the synthesis of the cage product mixture of **CC3** and **CC14**.

As a result of the initial screen, a ratio of TFB-Me_3TFB (3:1) was used to synthesise the mixed cage product sample on a larger scale. The cage species were subsequently separated by preparative HPLC, using an isocratic flow of methanol, with the new cage **CC14** isolated as a white solid in high purity (> 99 % a/a by HPLC; Figure 3.3) and in an overall yield of 14 %.

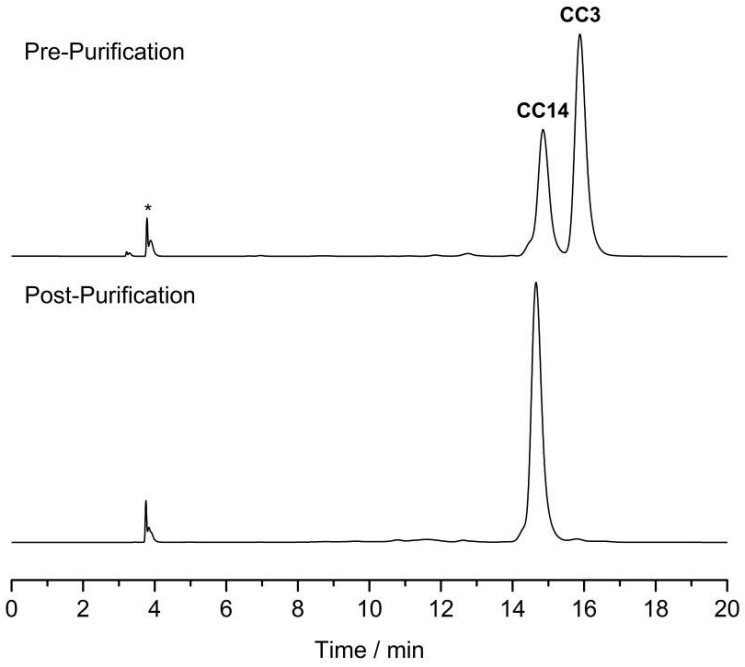

Figure 3.3 HPLC analysis for the cage product mixture formed by the reaction of *R,R*-CHDA with TFB and Me_3TFB (3:1) before and after purification *via* preparative HPLC. Column: Syncronis C_8; 150 × 4.6 mm; 3 µm; mobile phase: isocratic CH_3OH; flow: 0.5 mL min^{-1}; detection: λ = 254 nm; oven temperature = 30 °C. *$CHCl_3$ solvent peak.

^{1}H NMR spectroscopy confirmed the isolation of a cage containing three equivalents of TFB and one equivalent of Me_3TFB (Figure 3.4) Analysis of the integration confirmed the presence of nine aromatic protons relative to twelve imine protons. In addition, the multiplet at δ 2.32 ppm could be assigned to the three methyl groups on the single Me_3TFB molecule. Based on this observation, an imine bond-based POC molecule composed of at least two different aldehyde precursors has been successfully isolated for the first time, effectively reducing the symmetry of the resultant cage. There are other examples of asymmetric cages in the literature, but they tend to be restricted to metal-organic cage systems.[34, 35]

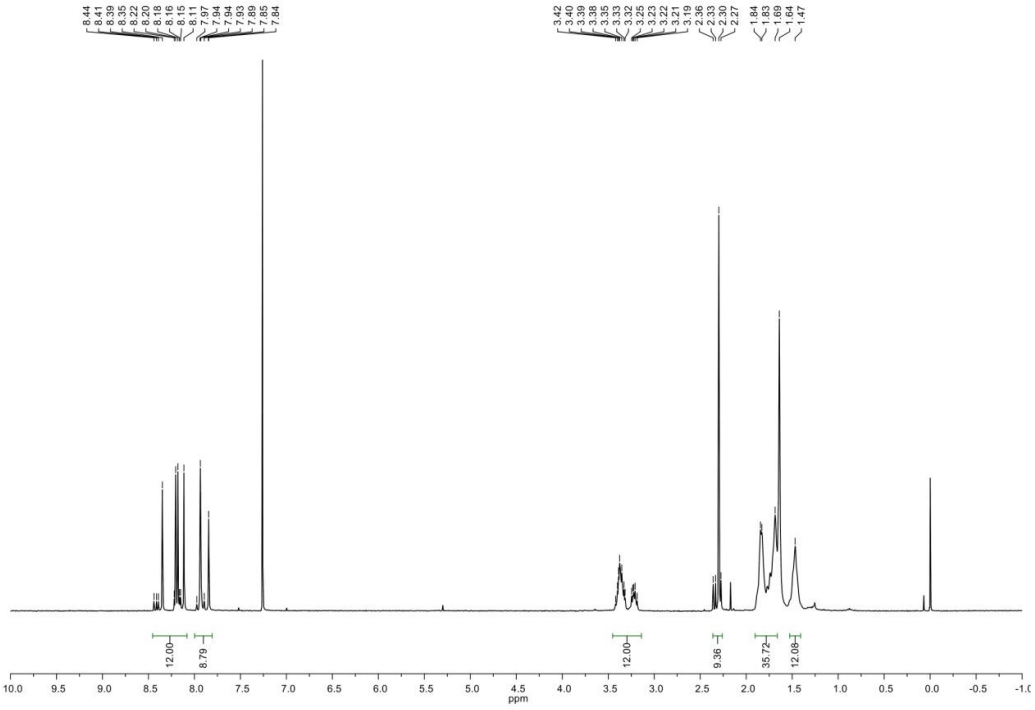

Figure 3.4 ^{1}H NMR spectrum ($CDCl_3$) of **CC14**.

Analysis by MALDI-TOF mass spectrometry gave a molecular ion peak of *m/z* = 1159, which correlates to a [4+6] cage containing three equivalents of TFB and one equivalent of Me_3TFB (Figure 3.5). However, a weak molecular ion peak of *m/z* = 1201 is also observable, and this may be assigned to a cage species containing two equivalents each of TFB and Me_3TFB. This cage species was not detected upon ^{1}H NMR analysis but may explain a slight shoulder on the **CC14** peak in the post-purification HPLC analysis (Figure 3.3). As MALDI-TOF is not quantitative, it is presumed that the impurity is in fact very small and it therefore has little or no effect on crystallinity or gas sorption behaviour.

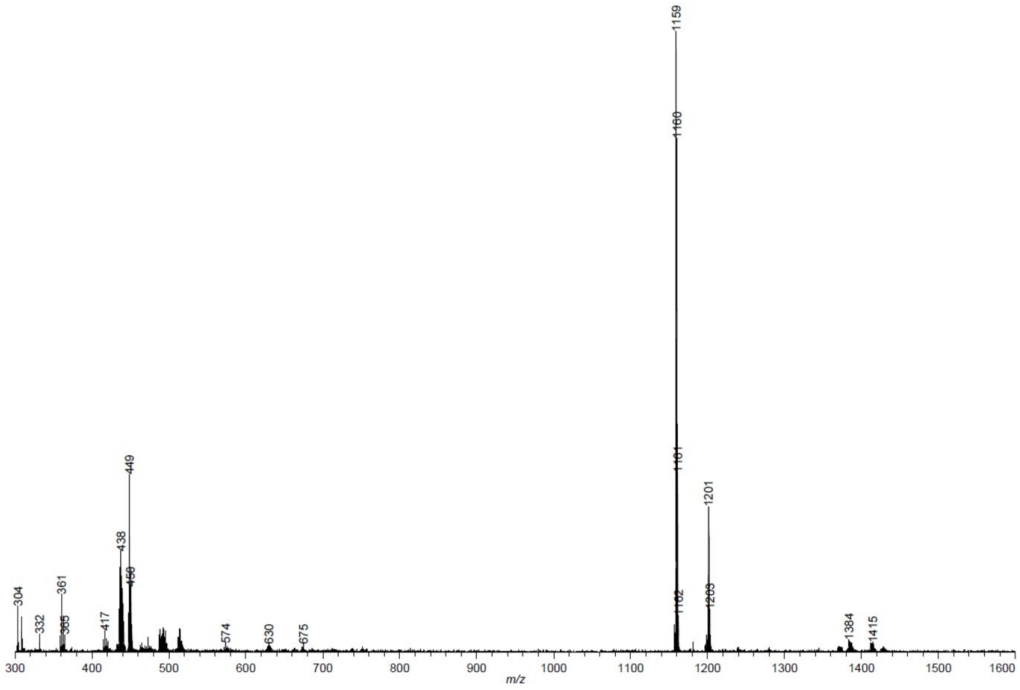

Figure 3.5 MALDI-TOF mass spectrum of **CC14** in dithranol/THF solution. Peaks at 1384 and 1415 are dithranol adducts from the matrix used.

CC14 was initially isolated as an amorphous material, as confirmed by PXRD analysis. Crystallisation of the cage from DCM-acetone (vial-in-vial) gave octahedral crystals that were characterised by scXRD (performed by Dr Marc Little; Figure 3.6). **CC14** crystallised in the chiral cubic space group $F4_132$, reminiscent of **CC3***α*,[36] where the cage molecule has tetrahedral symmetry (point group *T*) and packs in a window-to-window fashion, with a 3-D diamondoid pore network passing through the intrinsic cage voids. The methylated aromatic group was disordered over the four possible aromatic sites in each cage and no ordering of the methyl groups between cages was observed. As predicted, the methyl groups protrude into the diamondoid pore network. Therefore, with the retention of the pore network, it can be argued that **CC14** is isoreticular with respect to its parent cage **CC3**. Furthermore, with the methyl groups protruding into the cage windows, this should offer modified gas sorption properties.

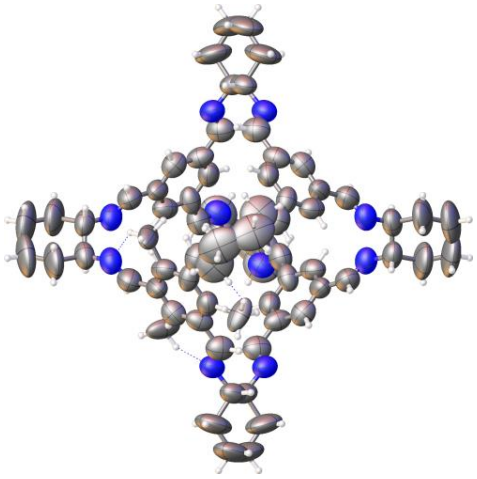

Figure 3.6 Displacement ellipsoid plot from the single crystal structure **CC14**·$(CH_2Cl_2)_{0.5}$. CH_2Cl_2 solvent omitted for clarity, in addition to positional disorder of the methyl groups. Ellipsoids displayed at 50 % probability level.

A bulk sample of crystalline **CC14** was prepared by layering acetone onto a solution of the cage in DCM, followed by slow evaporation under a flow of nitrogen. The bulk material was then desolvated at 60 °C under vacuum. SEM analysis (performed by Dr Tom Hasell) of the bulk sample of **CC14** confirmed that its morphology was octahedral (Figure 3.7), which was in accordance with the initial examination made upon scXRD analysis.

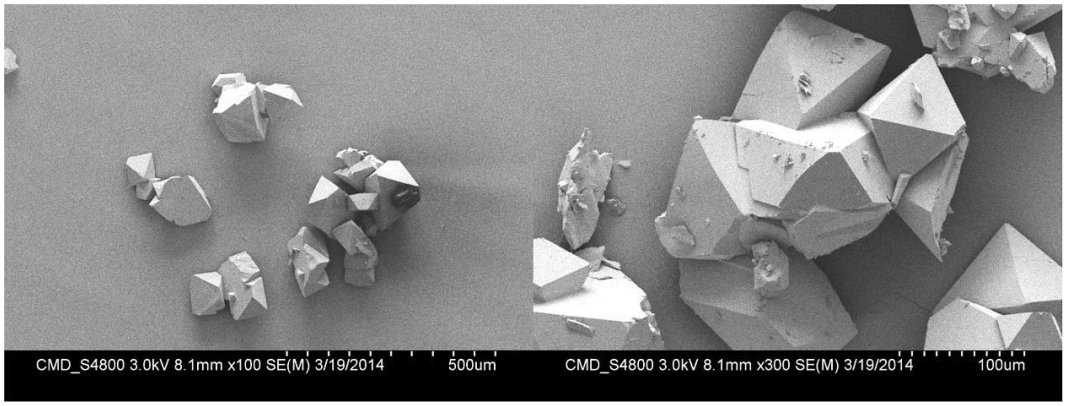

Figure 3.7 SEM images of crystalline **CC14** obtained *via* crystallisation from DCM-acetone.

PXRD analysis (performed by Dr Sam Chong) confirmed that the bulk desolvated sample of **CC14** was phase-pure by comparison with the simulated powder pattern from scXRD (Figure 3.8). In addition, CSP calculations (performed by Dr Angeles Pulido) confirmed that the observed window-to-window packing mode was the lowest energy polymorph. The powder pattern simulated from these calculations also

matched those of the bulk material and single crystal simulation. Along with the original amorphous material, the bulk desolvated sample was used to investigate the gas sorption properties of **CC14**.

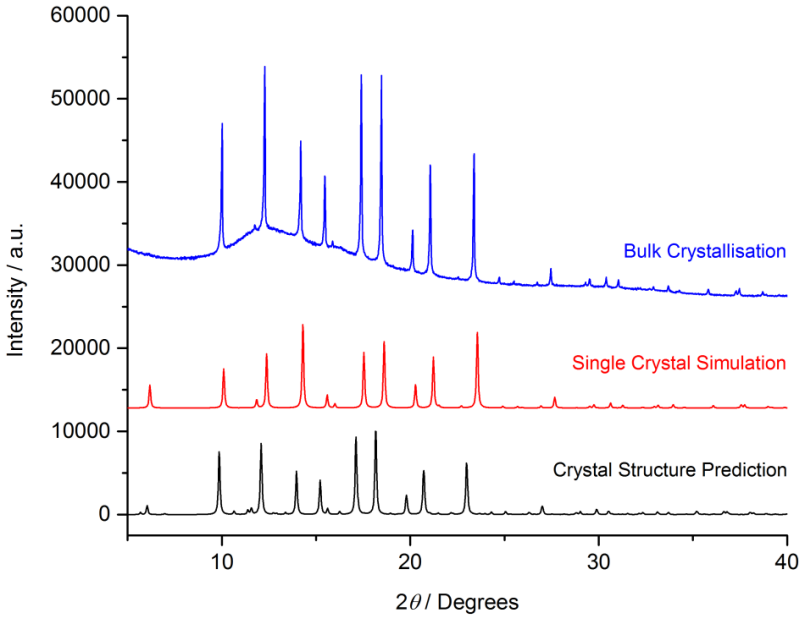

Figure 3.8 PXRD data for the bulk desolvated crystalline sample (blue), single crystal simulation (red) and CSP calculations (black).

3.4 Rationalisation of the Gas Sorption Properties of CC14

Table 3.2 Gas sorption values for **CC3***α* and **CC14** at 1 bar ([a]crystalline sample; [b]amorphous sample).

	SA_{BET} / $m^2\ g^{-1}$	N_2 / mmol g^{-1}	H_2 / mmol g^{-1}	CO_2 / mmol g^{-1}	Xe / mmol g^{-1}	Kr / mmol g^{-1}
	77 K		77 K	273 K	273 K	273 K
CC3*α*[4]	409	4.50	5.00	2.01	2.60	1.52
CC14[a]	320	4.11	3.64	1.57	1.58	0.96
CC14[b]	556	8.28	4.68	1.86	-	-

N_2 sorption measurements of crystalline **CC14** can be rationalised based on its crystal structure. **CC14** displays a Type I isotherm (Figure 3.9), highlighting the microporous nature of the material and mirroring the isotherm shape of isoreticular **CC3**. However, the overall N_2 uptake and apparent BET surface area of **CC14** (4.11 mmol g^{-1}, 320 $m^2\ g^{-1}$) are slightly lower than that of **CC3** (4.50 mmol g^{-1},

409 m^2 g^{-1}) at 77 K and 1 bar. This decrease in N_2 capacity was expected, as the introduction of the methyl groups has reduced the pore volume and subsequently increased the mass of the cage. This correlates with the observations of Tilford *et al.* for example, where the inclusion of longer chain alkyl groups in a range of COFs resulted in a decrease in surface area.[25]

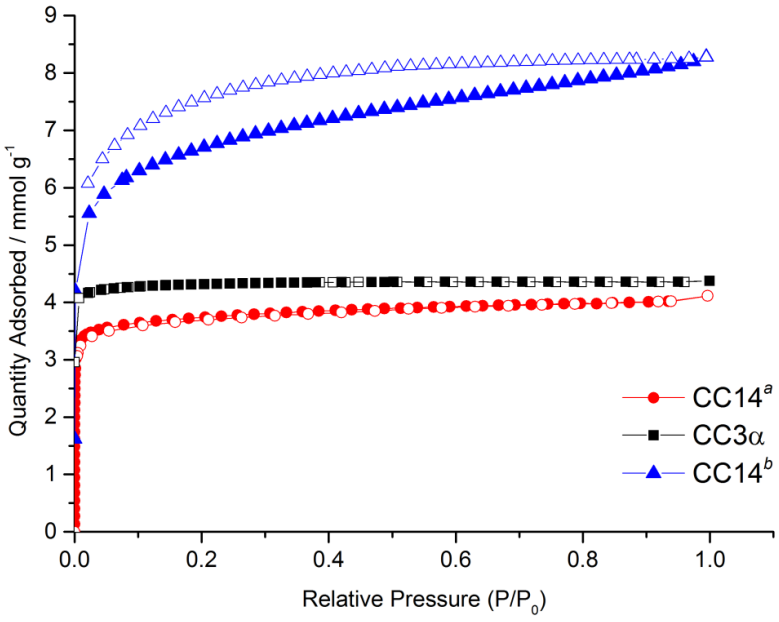

Figure 3.9 N_2 sorption isotherms for crystalline (**CC3***α* and **CC14**^{a}) and amorphous (**CC14**^{b}) samples at 77 K and 1 bar. Filled and open symbols represent adsorption and desorption isotherms respectively.

The gas sorption properties of crystalline **CC14** with respect to other gases (H_2, CO_2, Xe and Kr) also follow this downward trend in comparison to **CC3** (Table 3.2). On the other hand, the gas sorption properties for the amorphous sample of **CC14** surpass those of crystalline **CC3**. This behaviour could be rationalised, as it has been reported that amorphous samples of **CC3**, generated by rapidly-induced precipitation, exhibit enhanced microporosity due to an increase in both disorder and defects.[4] **CC14** shows no evidence of an enhanced capacity for a particular gas, which differs from the methylated MOFs and COFs that were introduced in Section 3.2.

The respective PSDs of **CC14** and **CC3**, measured using CO_2 as a probe gas (Figure 3.10a), not only demonstrates the reduction in pore volume upon the

introduction of the methyl groups, but also a contraction of the pore width to a narrower size. This phenomenon was also studied by MD simulations, whereby changes to the PLE and cage cavity size, in comparison to **CC3**, were investigated.

As previously discussed, cage molecules are not static bodies due to their inherent flexibility and are continuously vibrating; resulting in changes to the size of the pore window.[12] Therefore, gases that may be considered too large to fit, such as Xe, are able to diffuse through, as the pore windows are "open" for a certain amount of the simulated time period. For example, in **CC3**, it was found that the distribution of window sizes varies from 3.0 Å to 4.5 Å for the empty host, and that the cage window is "open" to Xe for only 7 % of the simulation time.[11] The restricted diffusion characteristics of Xe in **CC3** have also been confirmed by dynamic breakthrough measurements, where the larger Xe atom was separated from Kr at low concentrations in air.[6]

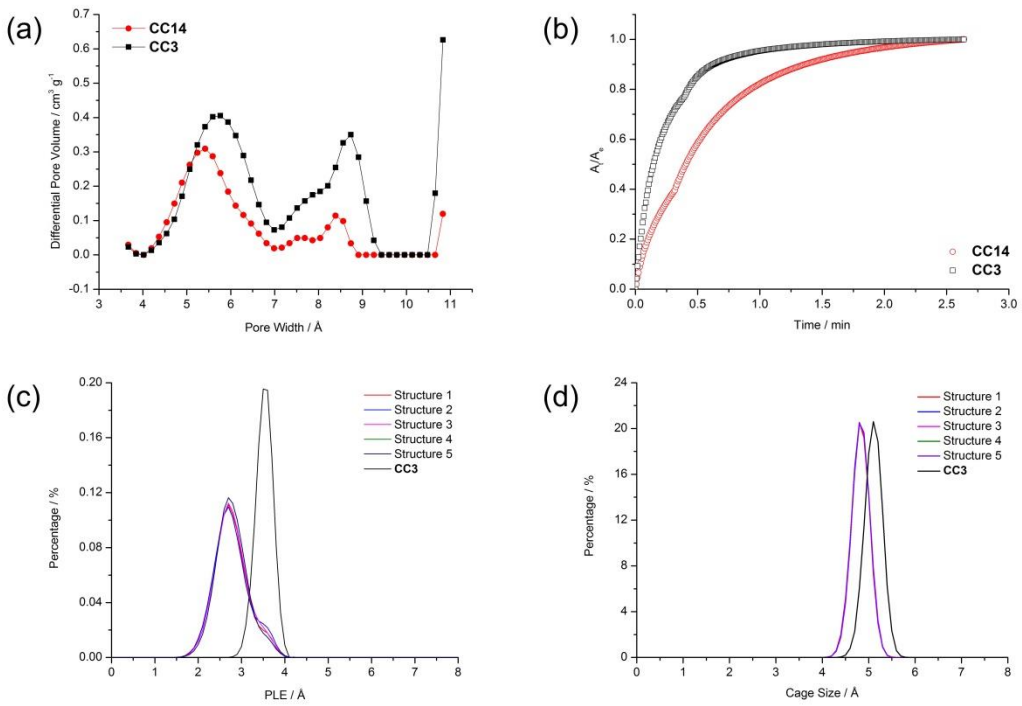

Figure 3.10 (a) PSD for **CC14** (filled red circles) and **CC3** (filled black squares) using CO_2 as a probe gas. (b) Xe kinetics plot for **CC14** (open red dots) and **CC3** (open black squares) measured at 273 K for the pressure increment 5 – 10 mbar. Plotted as normalised Xe A_t/A_e *vs*. time, where A_t is the quantity adsorbed at time *t*, and A_e is the quantity adsorbed at equilibrium (taken as 2.60 min). (c) Plot showing the PLE for **CC14** and **CC3** over five structural models. (d) Plot showing the cage cavity size for **CC14** and **CC3** over five structural models.

The introduction of methyl groups into the interconnected pore structure of **CC3** would be expected to shift the cage cavity size and PLE to a narrower distribution (to the left), as was found upon investigation of the PSD. For **CC14**, as the position of the methylated aromatic group is disordered with respect to adjacent cage molecules, MD simulations (performed by Dr Dan Holden) were run for five structural models, with the placement of the methylated aromatic group randomised to ensure that a suitable statistical representation of different packing motifs was sampled. Analysis of the **CC14** pore structure showed that the cavity size for all five models remains consistent, even though the position of the methylated aromatic group was randomised over the structure (Figure 3.10d). This resulted in a slightly reduced average diameter (4.80 Å) in comparison to **CC3**. In theory, this means that it would be more difficult for larger gas molecules such as Xe to enter the cage cavity *via* opportunistic hopping.

Similarly, the PLE was also observed to shift to the left, and the distribution of this is determined by the position of the methylated aromatic face (Figure 3.10c). When compared to **CC3**, it can be seen that the average size of the channel between the pore windows has been reduced from ~3.60 Å to ~2.75 Å, and that there is a broader distribution of channel sizes. This will have a direct impact on the kinetics of the 3-D pore structure, as the bottleneck feature of it is more pronounced; therefore making gas diffusion more difficult, and as a consequence, relatively slower. Furthermore, with more methylated aromatic faces in close proximity, which is statistically possible, the site will become even smaller and therefore amplify this effect.

CC14 shows a similar ideal selectivity to **CC3** for Xe over Kr, which we previously showed could be used to perform industrially relevant separations.[6] Xe adsorption kinetics measurements (performed by Dr Tom Hasell) reveal the difference created by the narrowing of the pore channels in **CC14**, with the diffusion of Xe through the structure being visibly hindered (Figure 3.10b). This also complements the findings of the MD simulations. Controlling the diffusion of Xe through the cage crystals in this way could give practical advantages in terms of breakthrough separations, with relevance to the treatment of radioactive air streams.[37, 38]

3.5 Synthesis of Other TFB Derivatives

To investigate the effect of sterics on this scrambling strategy, two more TFB derivatives were synthesised, with each possessing more sterically demanding substituents.

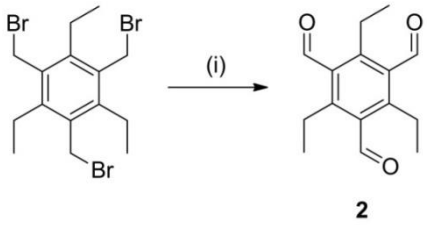

Scheme 3.3 Reaction scheme for the synthesis of 1,3,5-triethyl-2,4,6-tris(formyl)benzene (Et_3TFB), **2**. Reaction conditions: (i) NaH, 2-nitropropane, DMF, rt, 74 %.

Et_3TFB (**2**) was also synthesised *via* a modified Hass procedure (Scheme 3.3) using sodium hydride as a base instead of sodium methoxide, which gave unsatisfactory yields in this case.[31] Following the procedure utilised for the scrambling of Me_3TFB, the reaction of TFB and Et_3TFB with *R,R*-CHDA only yielded **CC3** upon analysis by analytical HPLC. This shows that the longer ethyl chains take up too much space and impede the incorporation of even a single Et_3TFB molecule into the cage structure. This indicated that methyl groups may be as big a functionality that can be introduced onto TFB without precluding cage formation.

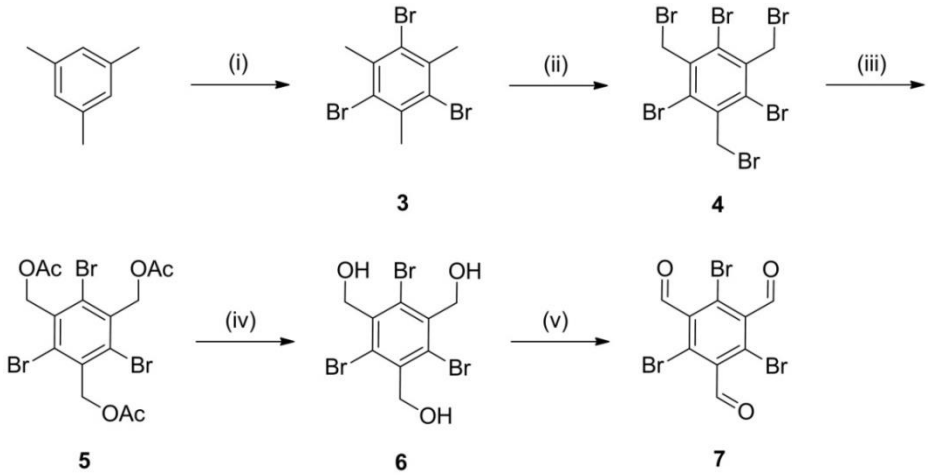

Scheme 3.4 Reaction scheme for the synthesis of 1,3,5-tribromo-2,4,6-tris(formyl)benzene (Br_3TFB), **7**. Reaction conditions: (i) Br_2, Fe, rt, 70 %. (ii) Br_2, DCM, *hv*, 40 °C, 90 %. (iii) KOAc, DMF, 70 °C, 91 %. (iv) KOH, H_2O, 100 °C, 94 %. (v) PCC, Celite, 4 Å MS, DCM, rt, 92 %.

To investigate this effect further, Br_3TFB (**7**) was synthesised following a five-step procedure previously reported by Bruns *et al* (Scheme 3.4).[39] Starting from trimethylbenzene, successive bromination reactions of the aromatic and methyl protons yielded **4**. The nucleophilic substitution reaction of the bromomethyl substituents with potassium acetate gave **5**, and subsequent base hydrolysis to the tri-alcohol **6**, followed by oxidation using pyridinium chlorochromate (PCC), gave the desired trialdehyde **7**. All steps were in good to excellent yields with the final product obtained in high purity.

However, when Br_3TFB was scrambled with TFB and *R,R*-CHDA, analysis by analytical HPLC again showed the formation of no asymmetric cage species, with only **CC3** observable. As previously hypothesised, this may be due to the steric bulk, this time of the large bromine atom, inhibiting cage formation.

3.6 Conclusions and Outlook

A derivative of the POC precursor TFB, possessing three additional methyl groups, was chosen as a candidate for cage synthesis. Its incorporation was hypothesised to narrow the dimensions of the pore windows in the resultant cage molecule, therefore tuning the gas sorption properties while retaining the same topology as the parent cage **CC3**.

Although cage formation was unsuccessful, it was found that by scrambling this derivative (Me_3TFB) with TFB and *R,R*-CHDA and then subsequently purifying by preparative HPLC, the POC molecule **CC14** could be isolated as a phase-pure porous material. Packing in an isoreticular window-to-window fashion, **CC14** possesses the same 3-D diamondoid pore network as **CC3***α*, with the methyl groups protruding into the cage cavity. In comparison to **CC3**, gas sorption analysis showed that crystalline **CC14** exhibited a marked decrease in gas uptake across a range of gases, which verifies the loss of pore volume upon the introduction of the methyl groups. This characteristic was also confirmed by MD simulations, where the cage cavity size and PLE of **CC14** were shown to constrict in comparison to **CC3**. Investigation of the Xe kinetics showed that the diffusion of this large noble gas through the pore structure of **CC14** was more hindered, and whilst complementing the findings of the MD simulations, it also showed that **CC14** could find potential application in the separation of Xe from Kr gas.

The unsuccessful incorporation of other TFB derivatives shows that this approach towards synthesising a series of isoreticular cages may be of limited scope. However, this was shown to be a steric issue, so if it was possible to introduce smaller groups - such as fluorine for example - then the preparation of a family of cages with tunable properties can be envisaged. Furthermore, the trialdehyde precursor need not contain three additional groups on the aromatic ring. The introduction of a single functional group should suffice, with the aim of tuning properties being retained. TFB derivatives of this type have already been successfully utilised in POC synthesis within our research group. Finally, derivatives of other trialdehyde precursors used in the synthesis of POCs, such as 1,3,5-tri(4-formylphenyl)benzene,[40] could also be synthesised and utilised with the same aims in mind.

3.7 Experimental

3.7.1 Materials

Sodium hydride (57 – 63 % dispersion in mineral oil) was purchased from Alfa Aesar. TFB was purchased from Manchester Organics and *R,R*-CHDA was purchased from TCI-UK. All other reagents were obtained from Sigma Aldrich and all reagents were used as received.

3.7.2 Syntheses

1,3,5-Trimethyl-2,4,6-tris(formyl)benzene (1)[31, 32]

2-Nitropropane (1.34 g, 15.0 mmol) was charged to a solution of sodium methoxide (0.54 g, 10.0 mmol) in methanol (30 mL). After stirring at rt for 1 h, 1,3,5-trimethyl-2,4,6-tris(bromomethyl)benzene (1.00 g, 2.51 mmol) was added and the reaction mixture stirred at rt for a further 22 h. After this time, water (60 mL) was added and the resulting white precipitate was isolated by filtration. The aqueous filtrate was collected and extracted with DCM (2 × 100 mL). The isolated white solid was dissolved in the combined organic layers and the DCM solution was then washed with water (2 × 100 mL). The organic phase was dried over anhydrous magnesium sulfate, filtered and the filtrate concentrated to dryness under vacuum to afford the crude product as a white solid. This was purified by column chromatography (DCM) to yield **1** as a powdery white solid (0.35 g, 69 %).

^{1}H NMR ($CDCl_3$, 400 MHz) δ 10.60 (3 H, s, 3 × C*H*O), 2.63 (9 H, s, 3 × CH_3); ^{13}C NMR ($CDCl_3$, 100.6 MHz) δ 194.43, 143.34, 135.16, 16.41; IR (ν_{max}/cm^{-1}) 2887, 1731, 1689, 1559, 1419, 1390, 1071, 845; CI-MS: *m/z* 205 $[M+H]^+$.

1,3,5-Triethyl-2,4,6-tris(formyl)benzene (2)[31]

A solution of sodium hydride (0.41 g, 10.3 mmol) in anhydrous dimethylformamide (DMF, 30 mL) was stirred at 0 °C for 20 min. After this time, 2-nitropropane (1.22 g, 13.7 mmol) was added and the reaction mixture was allowed to warm up to rt with stirring, at which point 1,3,5-triethyl-2,4,6-tris(bromomethyl)benzene (1.00 g, 2.27 mmol) was added in one portion. The reaction mixture was stirred vigorously at rt for 22 h and then poured into DCM (150 mL). The organic phase was washed with water (3 × 100 mL) and brine (3 × 100 mL), dried over anhydrous magnesium sulfate, filtered and the filtrate concentrated to dryness under vacuum to afford the crude product as a yellow oil. This was purified by column chromatography (DCM) to yield **2** as a waxy white solid (0.40 g, 74 %).

^{1}H NMR ($CDCl_3$, 400 MHz) δ 10.61 (3 H, s, 3 × C*H*O), 3.00 (6 H, q, 3 × CH_2), 1.27 (9 H, t, 3 × CH_3); ^{13}C NMR ($CDCl_3$, 100.6 MHz) δ 194.36, 149.39, 134.24, 22.68, 16.62; IR (ν_{max}/cm^{-1}) 2977, 2937, 2874, 1687, 1552, 1461, 1420, 1369, 1247, 1086, 1040, 949; CI-MS: *m/z* 247 $[M+H]^+$.

1,3,5-Tribromo-2,4,6-trimethylbenzene (3)[39]

To a 3-necked round-bottom flask containing iron powder (0.60 g) and bromine (29.10 g, 182 mmol) was added trimethylbenzene (4.00 g, 33.3 mmol) at rt over a period of 1 h. The reaction mixture was stirred for 72 h to leave the crude product as a red-brown solid. Water (50 mL) was added and the solid was collected by vacuum filtration, washed with water (2 × 50 mL) and recrystallised from chloroform to yield **3** as white needles (8.30 g, 70 %).

^{1}H NMR ($CDCl_3$, 400 MHz) δ 2.66 (9 H, s, 3 × CH_3); ^{13}C NMR ($CDCl_3$, 100.6 MHz) δ 137.14, 125.12, 26.43; IR (ν_{max}/cm^{-1}) 2948, 1540, 1434, 1375, 1348, 1268, 1017, 949, 904; CI-MS: *m/z* 357 $[M+H]^+$.

1,3,5-Tribromo-2,4,6-tris(bromomethyl)benzene (4)

To a stirred solution of **3** (2.00 g, 5.60 mmol) in DCM (50 mL), in a fused-quartz round-bottom flask equipped with a reflux condenser, was added bromine (8.96 g, 56.0 mmol) over a period of 30 min at rt, whilst irradiating with a sunlamp (60 W). The irradiation source was then removed and the reaction mixture heated under reflux for 24 h. After this time, the reaction mixture was allowed to cool to rt and hexane (50 mL) was added. The resulting precipitate was isolated by filtration, washed with hexane (50 mL) and allowed to dry under vacuum to yield **4** as a powdery white solid (2.99 g, 90 %).

^{1}H NMR ($CDCl_3$, 400 MHz) δ 4.93 (6 H, s, 3 × CH_2); ^{13}C NMR ($CDCl_3$, 100.6 MHz) δ 138.14, 128.64, 35.66; IR (ν_{max}/cm^{-1}) 3043, 2988, 1531, 1434, 1367, 1214, 992, 860; CI-MS: *m/z* 593 $[M+H]^+$.

Tribromo-2,4,6-tris(acetoxymethyl)benzene (5)

Potassium acetate (1.39 g, 14.2 mmol) was added to a solution of **4** (1.40 g, 2.36 mmol) in anhydrous DMF (8.4 mL). With stirring, the reaction mixture was heated at 70 °C for 24 h, then cooled to rt, filtered and poured into DCM (60 mL). The organic phase was washed with water (5 × 35 mL) and brine (2 × 35 mL), dried over anhydrous magnesium sulfate, filtered and the filtrate concentrated to dryness under vacuum to yield **5** as a powdery white solid (1.21 g, 91 %), which was used without further purification in the next step.

^{1}H NMR ($CDCl_3$, 400 MHz) δ 5.55 (6 H, s, 3 × CH_2), 2.12 (9 H, s, 3 × CH_3); ^{13}C NMR ($CDCl_3$, 100.6 MHz) δ 170.60, 135.79, 131.60, 68.25, 20.76; IR (ν_{max}/cm^{-1}) 2968, 1725, 1540, 1461, 1386, 1354, 1222, 1034, 971, 953, 910; ESI-MS: *m/z* 551 $[M+Na]^+$.

1,3,5-Tribromo-2,4,6-tris(hydroxymethyl)benzene (6)

To **5** (1.00 g, 1.88 mmol) was added water (18 mL) and potassium hydroxide (1.14 g, 20.3 mmol) and the mixture was heated under reflux for 24 h. After this time, the reaction mixture was allowed to cool and the white solid was isolated by vacuum filtration and washed with water (5 mL), diethyl ether (5 mL) and acetone (5 mL) to yield **6** as a powdery white solid (0.72 g, 94 %).

^{1}H NMR (DMSO-d_6, 400 MHz) δ 5.23 (3 H, s, 3 × O*H*), 4.89 (6 H, s, 3 × CH_2); ^{13}C NMR (DMSO-d_6, 100.6 MHz) δ 139.65, 128.49, 65.41; IR (ν_{max}/cm^{-1}) 3137, 2959, 2901, 1540, 1474, 1369, 1303, 1219, 1036, 1017, 944; ESI-MS: *m/z* 425 $[M+Na]^+$.

1,3,5-Tribromo-2,4,6-tris(formyl)benzene (7)

To PCC (1.58 g, 7.32 mmol) in DCM (50 mL) was added celite (1.20 g) and activated 4 Å molecular sieves (1.50 g). With vigorous stirring, **6** (0.40 g, 0.99 mmol) was added and the reaction mixture was stirred at rt for 48 h. After this time, the orange-brown reaction mixture was filtered through a pad of silica eluting with DCM. The filtrate was concentrated to dryness under vacuum to yield **7** as a powdery white solid (0.36 g, 92 %).

^{1}H NMR ($CDCl_3$, 400 MHz) δ 10.15 (3 H, s, 3 × C*H*O); ^{13}C NMR (THF-d_8, 100.6 MHz) δ 191.08, 138.53, 125.10; IR (ν_{max}/cm^{-1}) 2886, 1680, 1555, 1416, 1385, 1068, 841; CI-MS: *m/z* 397 $[M+H]^+$.

CC14

DCM (145 mL) was slowly added to a mixture of TFB (0.45 g, 2.79 mmol) and **1** (0.19 g, 0.93 mmol) in a 500 mL round-bottom flask at rt. A solution of *R,R*-CHDA (0.64 g, 5.58 mmol) in DCM (55 mL) was added slowly *via* Pasteur pipette. After 6 d, the solvent was removed under vacuum (< 20 °C) to leave a yellow solid, which was then washed with ethanol (20 mL), isolated by filtration and dried under vacuum to yield a powdery white solid (0.62 g). The mixed cage product (0.60 g) was dissolved in chloroform (30 mL) and purified by preparative HPLC. The product-containing fractions were concentrated to dryness under vacuum (< 20 °C) to yield **CC14** as a powdery white solid (0.15 g, 14 %).

^{1}H NMR ($CDCl_3$, 400 MHz) δ 8.44-8.11 (12 H, m, 12 × C*H*=N), 7.97-7.84 (9 H, m, 9 × Ar*H*), 3.42-3.19 (12 H, m, 12 × C*H*-N), 2.36-2.27 (9 H, m, 3 × CH_3), 1.84-1.47 (48 H, m, 24 × CH_2); ^{13}C NMR ($CDCl_3$, 100.6 MHz) δ 160.65, 159.73, 159.39, 159.00, 138.28, 136.88, 136.76, 136.74, 133.43, 130.03, 129.91, 129.35, 75.05, 74.99, 74.05, 73.38, 33.44, 33.29, 24.67, 24.53, 18.39; IR (ν_{max}/cm^{-1}) 2926, 2855, 1646, 1445, 1369, 1341, 1155, 1091, 1038, 989; MALDI-TOF MS: *m/z* 1159 $[M]^+$;

CHN analysis for $C_{75}H_{90}N_{12}$: C 77.68, H 7.82, N 14.49; found C 74.42, H 7.73, N 13.35.

3.8 Single Crystal X-ray Crystallography

Crystal data for **CC14**·$(CH_2Cl_2)_{0.5}$ was collected using Diamond I19 Beamline synchrotron radiation. Formula $C_{72.5}H_{91}N_{12}Cl$; M = 1166.02 g·mol^{-1}; cubic space group $F4_132$, colourless crystal; a = 24.708(7) Å; V = 15083(7) Å^3; ρ = 1.027 g·cm^{-3}; μ = 0.089 mm^{-3}; F (000) = 5016; crystal size = 0.06 x 0.05 x 0.05 mm^3; T = 100(2) K; 9522 reflections measured (1.38° < Θ < 22.41°), 915 unique (R_{int} = 0.0850), 817 ($I > 2\sigma(I)$); R_1 = 0.1800 for observed and R_1 = 0.1848 for all reflections; wR_2 = 0.5444 for all reflections; max/min residual electron density = 0.410 and -0.222 e·Å^{-3}; data/restraints/parameters = 915/79/76; GOF = 2.658. Single crystals of **CC14** were very weakly diffracting, even though the data was collected using a synchrotron radiation source. The asymmetric unit for **CC14**·$(CH_2Cl_2)_{0.5}$ comprises 1/12 of a cage fragment and part of a partially occupied CH_2Cl_2 solvent molecule. A resolution limit of 0.9 Å was applied during refinement. Due to poor data quality, large wR_2 values were obtained after refinement of the structural model. The aromatic ring and directly bonded carbon atoms were refined with a planetary restraint (FLAT in SHELX). One carbon-carbon bond of the cyclohexyl ring was refined with a bond length restraint (DFIX in SHELX). For the cage molecule, atomic displacement parameters were restrained during refinement (SIMU and DELU in SHELX). The methyl substituted aromatic ring was disordered over the four aromatic ring positions for each cage molecule. Due to the symmetry of the space group, no respective ordering of the methyl groups could be determined. One partially occupied CH_2Cl_2 solvent molecule, site occupancy 50 %, was located in the intrinsic cage cavity.

3.9 References

1. P. Skowronek and J. Gawronski, *Org. Lett.*, 2008, **10**, 4755-4758.
2. T. Tozawa, J. T. A. Jones, S. I. Swamy, S. Jiang, D. J. Adams, S. Shakespeare, R. Clowes, D. Bradshaw, T. Hasell, S. Y. Chong, C. Tang, S. Thompson, J. Parker, A. Trewin, J. Bacsa, A. M. Slawin, A. Steiner and A. I. Cooper, *Nat. Mater.*, 2009, **8**, 973-978.
3. A. Kewley, A. Stephenson, L. Chen, M. E. Briggs, T. Hasell and A. I. Cooper, *Chem. Mater.*, 2015, **27**, 3207-3210.

4. T. Hasell, S. Y. Chong, K. E. Jelfs, D. J. Adams and A. I. Cooper, *J. Am. Chem. Soc.*, 2012, **134**, 588-598.
5. T. Mitra, K. E. Jelfs, M. Schmidtmann, A. Ahmed, S. Y. Chong, D. J. Adams and A. I. Cooper, *Nat. Chem.*, 2013, **5**, 276-281.
6. L. Chen, P. S. Reiss, S. Y. Chong, D. Holden, K. E. Jelfs, T. Hasell, M. A. Little, A. Kewley, M. E. Briggs, A. Stephenson, K. M. Thomas, J. A. Armstrong, J. Bell, J. Busto, R. Noel, J. Liu, D. M. Strachan, P. K. Thallapally and A. I. Cooper, *Nat. Mater.*, 2014, **13**, 954-960.
7. A. F. Bushell, P. M. Budd, M. P. Attfield, J. T. A. Jones, T. Hasell, A. I. Cooper, P. Bernardo, F. Bazzarelli, G. Clarizia and J. C. Jansen, *Angew. Chem.*, 2013, **52**, 1253-1256.
8. T. Hasell, H. Zhang and A. I. Cooper, *Adv. Mater.*, 2012, **24**, 5732-5737.
9. J. T. A. Jones, T. Hasell, X. Wu, J. Bacsa, K. E. Jelfs, M. Schmidtmann, S. Y. Chong, D. J. Adams, A. Trewin, F. Schiffman, F. Cora, B. Slater, A. Steiner, G. M. Day and A. I. Cooper, *Nature*, 2011, **474**, 367-371.
10. T. Hasell, M. Schmidtmann, C. A. Stone, M. W. Smith and A. I. Cooper, *Chem. Commun.*, 2012, **48**, 4689-4691.
11. D. Holden, K. E. Jelfs, A. Trewin, D. J. Willock, M. Haranczyk and A. I. Cooper, *J. Phys. Chem. C*, 2014, **118**, 12734-12743.
12. D. Holden, K. E. Jelfs, A. I. Cooper, A. Trewin and D. J. Willock, *J. Phys. Chem. C*, 2012, **116**, 16639-16651.
13. O. M. Yaghi, M. O'Keeffe, N. W. Ockwig, H. K. Chae, M. Eddaoudi and J. Kim, *Nature*, 2003, **423**, 705-714.
14. M. Eddaoudi, J. Kim, N. Rosi, D. Vodak, J. Wachter, M. O'Keeffe and O. M. Yaghi, *Science*, 2002, **295**, 469-472.
15. H. Furukawa, Y. B. Go, N. Ko, Y. K. Park, F. J. Uribe-Romo, J. Kim, M. O'Keeffe and O. M. Yaghi, *Inorg. Chem.*, 2011, **50**, 9147-9152.
16. B. P. Biswal, S. Chandra, S. Kandambeth, B. Lukose, T. Heine and R. Banerjee, *J. Am. Chem. Soc.*, 2013, **135**, 5328-5331.
17. D. Yuan, D. Zhao, D. Sun and H.-C. Zhou, *Angew. Chem. Int. Ed.*, 2010, **49**, 5357-5361.
18. L. Ma, J. M. Falkowski, C. Abney and W. Lin, *Nat. Chem.*, 2010, **2**, 838-846.
19. T. C. Wang, W. Bury, D. A. Gómez-Gualdrón, N. A. Vermeulen, J. E. Mondloch, P. Deria, K. Zhang, P. Z. Moghadam, A. A. Sarjeant, R. Q. Snurr, J. F. Stoddart, J. T. Hupp and O. K. Farha, *J. Am. Chem. Soc.*, 2015, **137**, 3585-3591.
20. T. Hasell, J. L. Culshaw, S. Y. Chong, M. Schmidtmann, M. A. Little, K. E. Jelfs, E. O. Pyzer-Knapp, H. Shepherd, D. J. Adams, G. M. Day and A. I. Cooper, *J. Am. Chem. Soc.*, 2014, **136**, 1438-1448.
21. K. E. Jelfs, X. Wu, M. Schmidtmann, J. T. A. Jones, J. E. Warren, D. J. Adams and A. I. Cooper, *Angew. Chem.*, 2011, **50**, 10653-10656.
22. Y. Jin, B. A. Voss, R. McCaffrey, C. T. Baggett, R. D. Noble and W. Zhang, *Chem. Sci.*, 2012, **3**, 874.
23. R. McCaffrey, H. Long, Y. Jin, A. Sanders, W. Park and W. Zhang, *J. Am. Chem. Soc.*, 2014, **136**, 1782-1785.
24. C. A. Fernandez, J. Liu, P. K. Thallapally and D. M. Strachan, *J. Am. Chem. Soc.*, 2012, **134**, 9046-9049.
25. R. W. Tilford, S. J. Mugavero, P. J. Pellechia and J. J. Lavigne, *Adv. Mater.*, 2008, **20**, 2741-2746.

26. B. S. Ghanem, M. Hashem, K. D. M. Harris, K. J. Msayib, M. Xu, P. M. Budd, N. Chaukura, D. Book, S. Tedds, A. Walton and N. B. McKeown, *Macromolecules*, 2010, **43**, 5287-5294.
27. H. Liu, Y. Zhao, Z. Zhang, N. Nijem, Y. J. Chabal, H. Zeng and J. Li, *Adv. Funct. Mater.*, 2011, **21**, 4754-4762.
28. B. Bhattacharya, R. Haldar, R. Dey, T. K. Maji and D. Ghoshal, *Dalton Trans.*, 2014, **43**, 2272-2282.
29. Y. Wang, C. Tan, Z. Sun, Z. Xue, Q. Zhu, C. Shen, Y. Wen, S. Hu, Y. Wang, T. Sheng and X. Wu, *Chem. Eur. J.*, 2014, **20**, 1341-1348.
30. M. W. Schneider, I. M. Oppel, A. Griffin and M. Mastalerz, *Angew. Chem.*, 2013, **52**, 3611-3615.
31. R. Balamurugan and A. K. Mohanakrishnan, *Tetrahedron*, 2007, **63**, 11078-11085.
32. H. B. Hass and M. L. Bender, *Org. Synth.*, 1950, **30**, 99-101.
33. S. Jiang, J. T. A. Jones, T. Hasell, C. E. Blythe, D. J. Adams, A. Trewin and A. I. Cooper, *Nat. Commun.*, 2011, **2**, 207.
34. Y. R. Zheng, W. J. Lan, M. Wang, T. R. Cook and P. J. Stang, *J. Am. Chem. Soc.*, 2011, **133**, 17045-17055.
35. W. Meng, T. K. Ronson and J. R. Nitschke, *Proc. Natl. Acad. Sci.*, 2013, **110**, 10531-10535.
36. M. A. Little, S. Y. Chong, M. Schmidtmann, T. Hasell and A. I. Cooper, *Chem. Commun.*, 2014, **50**, 9465-9468.
37. J. Liu, P. K. Thallapally and D. Strachan, *Langmuir*, 2012, **28**, 11584-11589.
38. J. Liu, C. A. Fernandez, P. F. Martin, P. K. Thallapally and D. M. Strachan, *Ind. Eng. Chem. Res.*, 2014, **53**, 12893-12899.
39. D. Bruns, H. Miura, K. P. C. Vollhardt and A. Stanger, *Org. Lett.*, 2003, **5**, 549-552.
40. S. Jiang, J. Bacsa, X. Wu, J. T. A. Jones, R. Dawson, A. Trewin, D. J. Adams and A. I. Cooper, *Chem. Commun.*, 2011, **47**, 8919-8921.

Chapter 4

Synthesis of Periphery-Substituted Porous Organic Cages

4.1 Preparation of Vicinal Diamines for POC Synthesis

In Chapter 3, the effect of modifying the TFB precursor on POC synthesis was explored. An alternative approach was to instead prepare and utilise new vicinal diamine precursors. The vast majority of commercially available diamines have already been evaluated within our research group. Therefore, in order to access new POCs, new diamines would need to be synthesised.

The preparation and utilisation of vicinal diamines in POC synthesis has been explored rarely, with more attention being paid to the synthesis of the aldehyde component for imine bond-based cages.[1-3] A notable exception is that of Giri *et al.*, who in the pursuit of porous liquid candidates, designed and prepared a range of aliphatic diamines towards the synthesis of alkylated organic cages.[4]

The preparation of enantiomerically-pure derivatives of the **CC3** precursor CHDA was of particular interest, as this has been successfully used in the synthesis of other POCs.[3] Ideally, the candidate 1,2-diamine would be functionalised at the 4,5-positions, with the expectation that this would frustrate the molecular packing and generate additional extrinsic porosity to complement the intrinsic cage cavity. This would also allow a direct comparison with the gas sorption properties of **CC3**. Furthermore, the introduction of reactive functional groups that would allow tuning of the gas sorption properties or enable the material to be used for a secondary purpose has been explored rarely with respect to POCs.[5-7] Post-synthetic modification (PSM) of the cage periphery would be particularly significant, as it offers the potential to tune the properties and subsequent application of the resultant POC. This strategy has already been well documented for MOFs[8] and other porous networks and polymers.[9-11]

4.2 Synthesis and Characterisation of Porous Organic Cage CC16

(1*R*,2*R*,4*R*,5*R*)-1,2-Diamino-4,5-dimethylcyclohexane was identified as a suitable precursor for POC synthesis. The two methyl groups at the 4,5-positions would be expected to increase the space between the cage molecules and therefore create additional accessible surface area. The creation of additional extrinsic porosity has been previously explored by Bojdys *et al.*, who used bulky directing groups to

frustrate the crystal packing, resulting in an improvement in surface area in comparison to unfunctionalised cages of the same dimensions.[12]

Following literature procedures, the diamine precursor **4** was isolated as a dihydrochloride salt (Scheme 4.1). Bis-imine **1** was synthesised in quantitative yield from (*S*)-1-phenylethylamine *via* reaction with glyoxal trimer dihydrate. The addition of allylzinc bromide at -78 °C afforded the *N*,*N'*-disubstituted 4,5-diamino-1,7-octadiene **2** in a 70 % yield with the 4*R*,5*R* configuration isolated as the major diastereoisomer.[13] Treatment of **2** with *n*-butylmagnesium chloride and catalytic bis-(cyclopentadienyl)zirconium (IV) dichloride resulted in reductive cyclisation to the cyclohexane derivative.[14] Despite purification by flash column chromatography, impurities were still observable upon isolation. Subsequent precipitation of the diamine hydrochloride salt from a DCM solution gave the pure product **3**. Hydrogenolysis of **3** was conducted using 20 % palladium hydroxide on carbon at 8 atmospheres pressure of hydrogen for 48 h, yielding the desired diamine salt **4**.

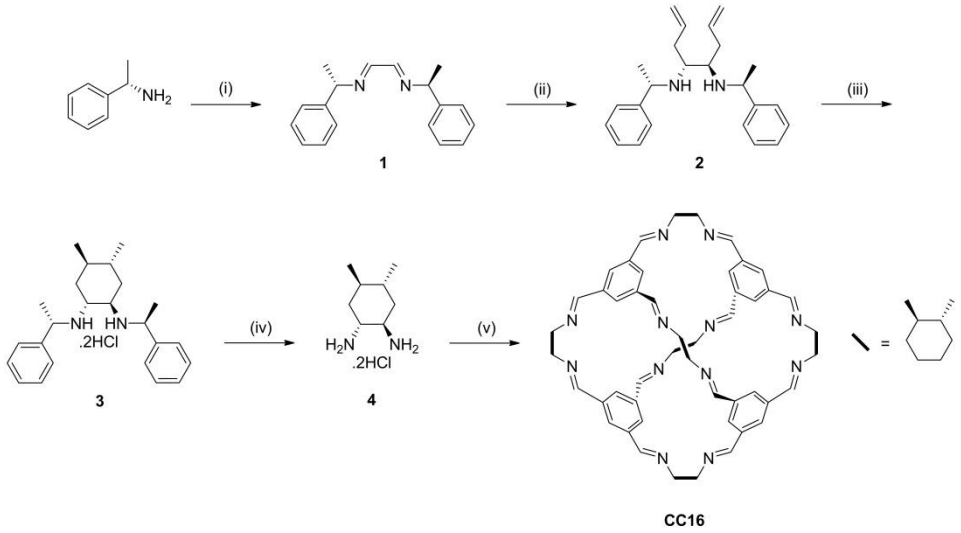

Scheme 4.1 Reaction scheme for the synthesis of **CC16**. Reaction conditions: (i) Glyoxal trimer dihydrate, $MgSO_4$, DCM, rt, 100 %. (ii) AllylZnBr, THF, -78 °C, 70 %. (iii) *n*-ButylMgCl, Cp_2ZrCl_2, Et_2O then 4 M HCl, DCM, rt, 64 % (2 steps). (iv) $Pd(OH)_2/C$, H_2, CH_3OH, rt, 99 %. (v) Et_3N then TFB, DCM-CH_3OH, rt, 79 %.

Diamine salts have been previously used to synthesise POCs.[15] The standard procedure involves free-basing the diamine salt using two equivalents of triethylamine in a methanol solution, followed by slow addition to a solution of TFB in DCM. Following this outline, the biphasic reaction of **4** and TFB was left to stand at room temperature for five days. After this time, no precipitated material was

observable, which is atypical of a cage synthesis under these conditions.[15] However, analysis by ^{1}H NMR spectroscopy showed that the trialdehyde had been fully consumed, with sharp singlet peaks with an integration ratio of 1:1 in the imine and aromatic regions confirming the formation of a single cage product. Slowly removing the DCM solvent under vacuum induced precipitation of a white solid and the desired cage **CC16** was isolated upon vacuum filtration in a 79 % yield.

Analysis by ^{1}H NMR spectroscopy mirrored the observations made for the crude reaction mixture, with singlet peaks at δ 8.16 ppm and δ 7.89 ppm confirming the presence of imine and aromatic protons respectively in a 1:1 ratio. Upon integrating the imine and aromatic signals to twelve protons each, the doublet at δ 1.19 ppm, representing the methyl groups located at the 4,5-positions of the cyclohexane ring, integrated to the required thirty-six protons (Figure 4.1).

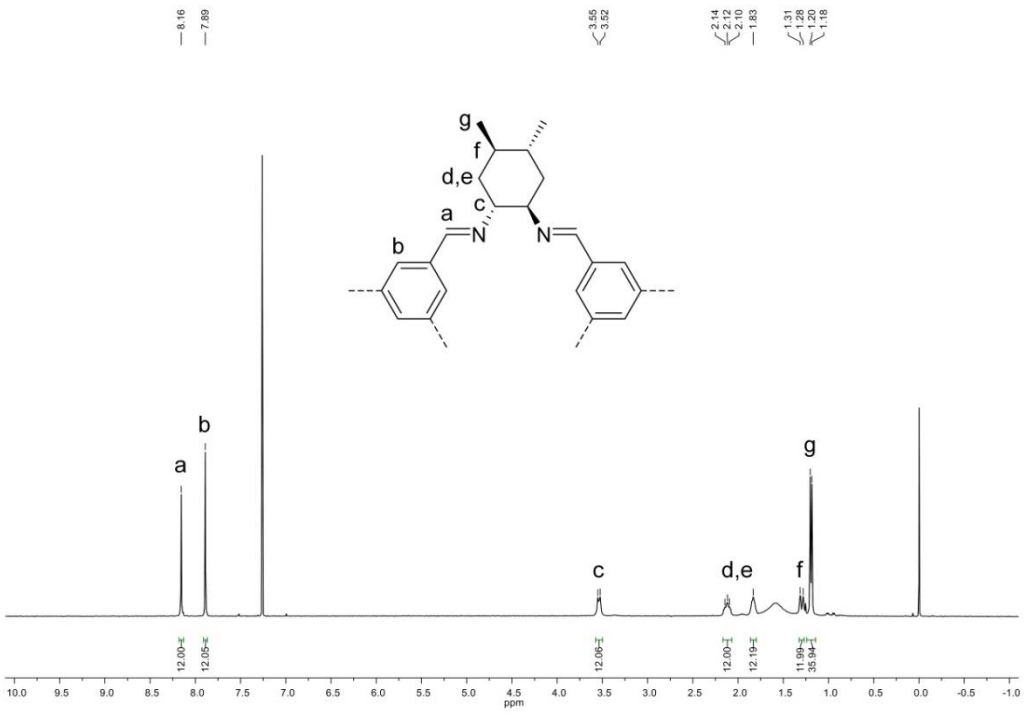

Figure 4.1 ^{1}H NMR spectrum ($CDCl_3$) of **CC16**.

Analysis by MALDI-TOF mass spectrometry gave a molecular ion peak of *m/z* = 1286, which correlates to a [4+6] cage structure (Figure 4.2). No other cage species were observable upon inspection of the spectrum, confirming that a single product had been isolated.

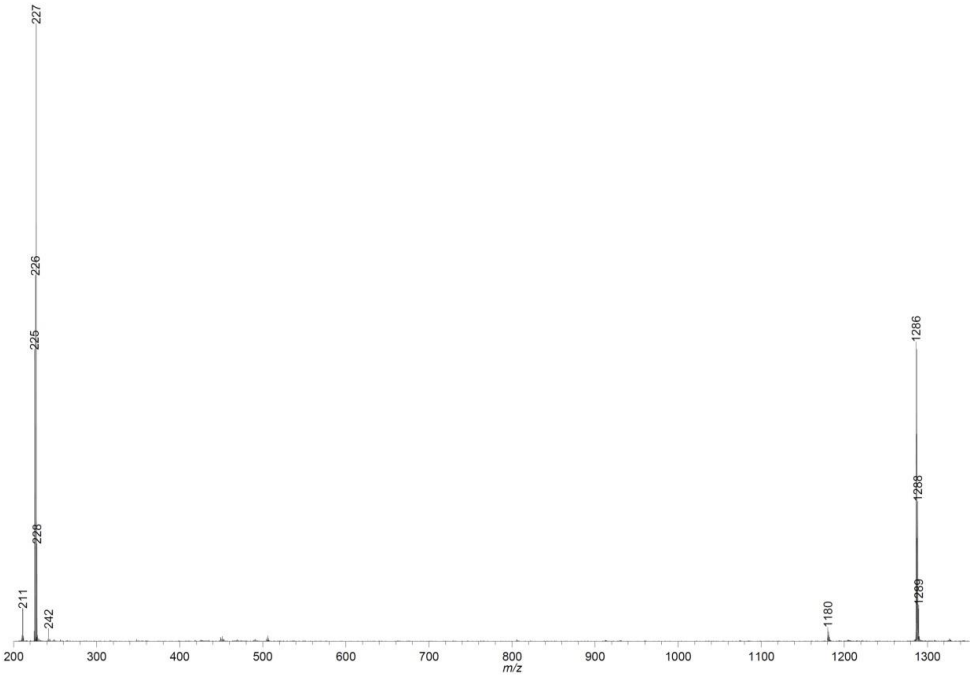

Figure 4.2 MALDI-TOF mass spectrum of **CC16** in dithranol/THF solution.

The bulk cage material isolated from the original reaction mixture, once fully desolvated, was found to be crystalline upon analysis by PXRD, with the powder pattern closely matching that simulated from scXRD analysis (Figure 4.3).

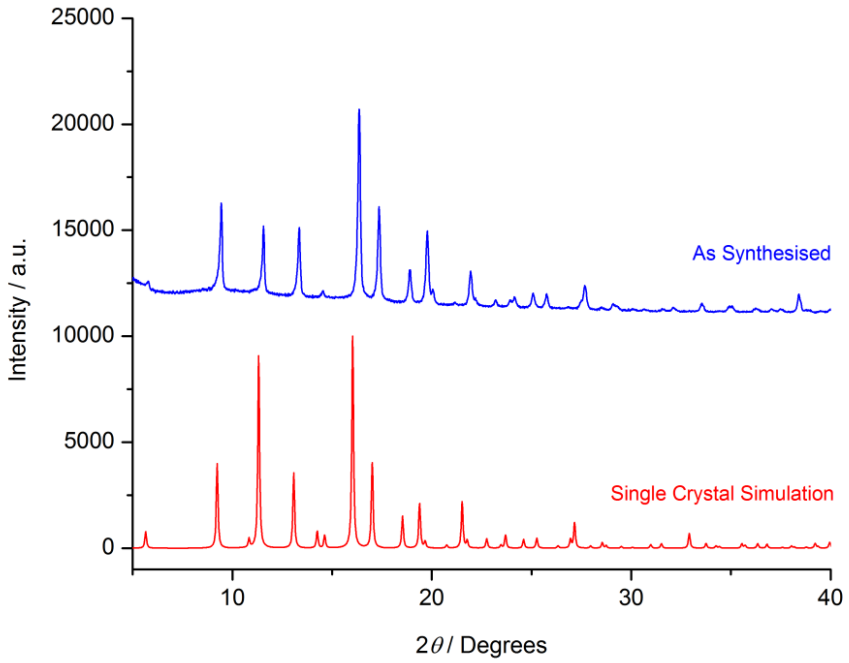

Figure 4.3 PXRD data for as-synthesised desolvated **CC16** (blue) and that simulated from single crystal analysis (red).

Crystallisation of the cage from DCM-ethyl acetate (vial-in-vial) gave very small octahedral crystals which could be characterised by scXRD (performed by Dr Marc Little; Figure 4.4a). **CC16** crystallised in the chiral cubic space group $F4_132$, in which the cage molecules have tetrahedral symmetry (point group *T*) and pack in a window-to-window fashion, with a 3-D diamondoid pore network passing through the intrinsic cage voids (Figure 4.4b). The packing is reminiscent of that observed for the parent cage **CC3** in its *α*-phase.[16] The peripheral methyl groups act as a wedge, forcing apart the cages and resulting in additional extrinsic porosity being generated, as well as the formation of an additional pore channel. The observed pore structure is similar to another cage, **CC13**, where its *β*-polymorph exhibits a double, interpenetrating pore structure upon exposure to a 1,4-dioxane directing solvent.[17] Advantageously, **CC16** does not require an additional directing solvent to achieve this. However, whereas the positionally-disordered geminal dimethyl groups in **CC13** significantly improve the cage's solubility properties, the solubility of **CC16**, even in chlorinated solvents, is poor.

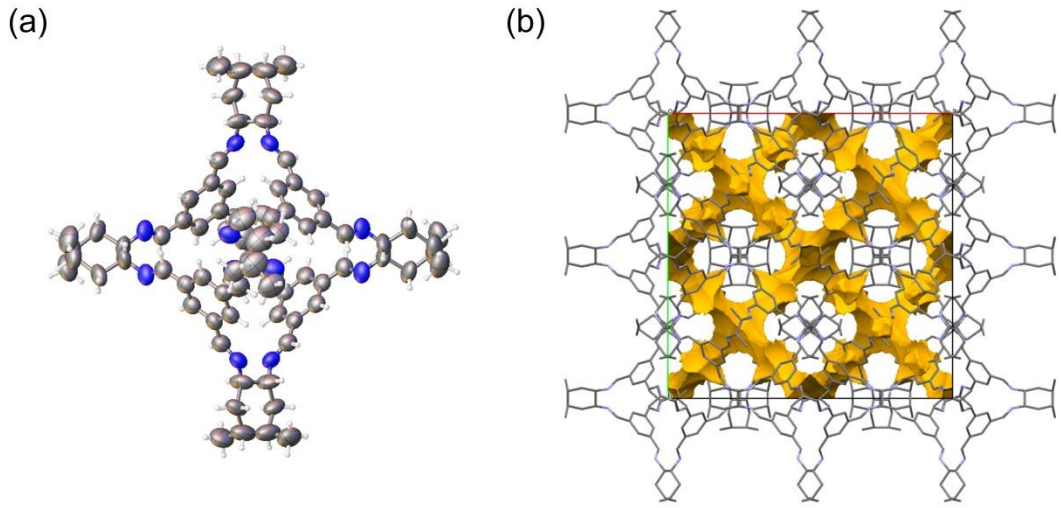

Figure 4.4 (a) Displacement ellipsoid plot from the single crystal structure **CC16**·$(CH_2Cl_2)_3$. CH_2Cl_2 solvent omitted for clarity. Ellipsoids displayed at 50 % probability level. (b) A unit cell of **CC16**, viewed along the *c*-axis, with the solvent accessible surface area for a N_2 probe of radius 1.20 Å.

SEM analysis (performed by Dr Shan Jiang) of crystalline samples of **CC16** confirmed that its morphology was octahedral (Figure 4.5), which was in accordance with the initial examination made upon scXRD analysis. Although not as perfectly crystalline as a sample specially prepared from DCM-ethyl acetate, the as-

synthesised material, which had been quickly precipitated from methanol, did exhibit crystalline character, complementing the observations from PXRD analysis. Therefore, the as-synthesised desolvated material was used directly to investigate the gas sorption properties of **CC16**.

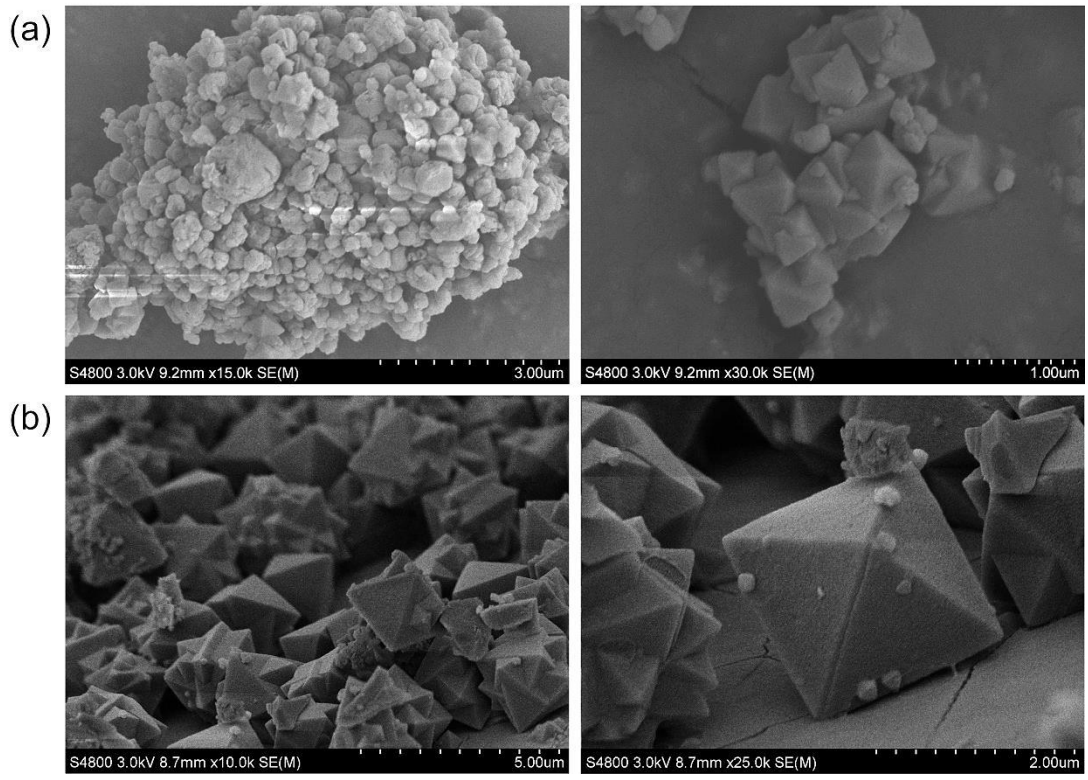

Figure 4.5 (a) SEM images of as-synthesised desolvated crystalline **CC16** obtained *via* precipitation from methanol. (b) SEM images of crystalline **CC16** obtained by crystallisation from DCM-ethyl acetate.

4.3 Gas Sorption Properties of CC16

Table 4.1 Gas sorption values for **CC3***α* and **CC16** at 1 bar.

	SA_{BET} / m^2 g^{-1}	N_2 / mmol g^{-1}	H_2 / mmol g^{-1}	CO_2 / mmol g^{-1}
		77 K	77 K	273 K
CC3*α*[16]	409	4.50	5.00	2.01
CC16	1023	20.03	5.92	2.00

N_2 sorption measurements of **CC16** at 77 K and 1 bar showed a Type I isotherm with a total uptake of 20.03 mmol g^{-1} and an apparent BET surface area of 1023 m^2 g^{-1}; that is, more than four and two times greater than **CC3**, respectively (Table 4.1). The improvement in surface area and overall N_2 and H_2 uptakes is a direct consequence

of the peripheral methyl groups generating extra accessible space between the individual cage molecules (Figure 4.6a). This matches the observations made upon scXRD analysis, where larger pores, as well as additional pore channels, were observable between the individual cage molecules as a result of the peripheral methyl groups frustrating the packing in the solid state. This conclusion is confirmed by analysis of the PSD (Figure 4.6b), which demonstrates a broader range of micropore sizes in comparison to **CC3**. In contrast, the CO_2 uptake for **CC16** is very similar to **CC3**, and this can be rationalised based on the fact that this measurement was run at 273 K, where the effect of a larger pore size on total gas uptake would be reduced.

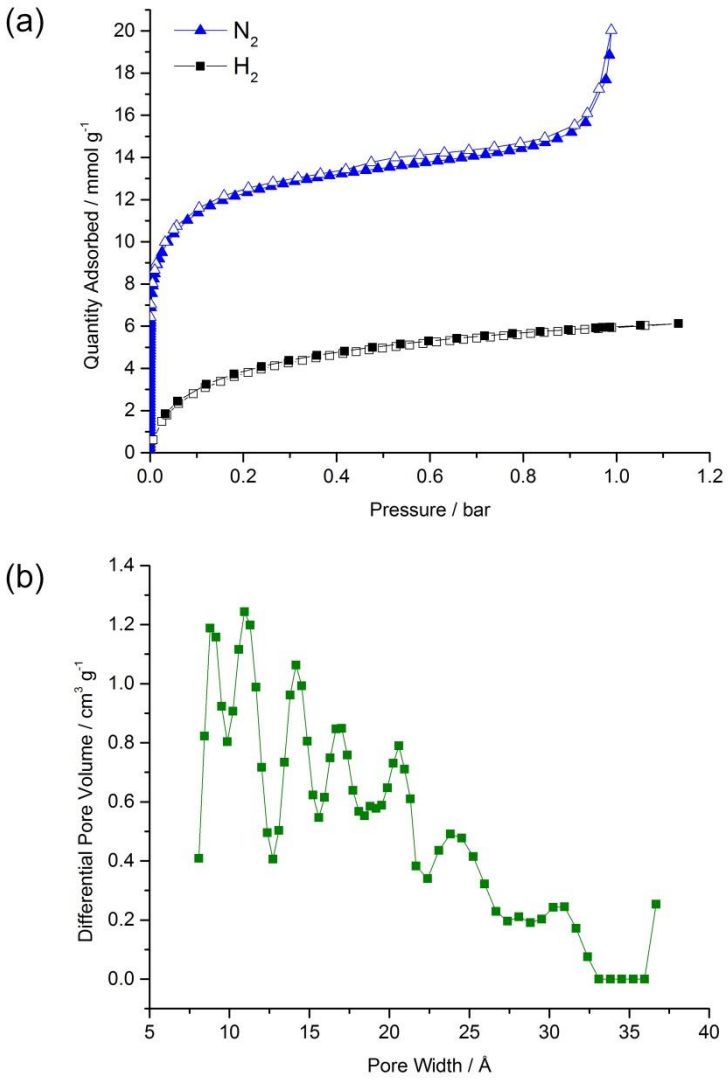

Figure 4.6 (a) Gas sorption isotherms for N_2 (blue triangles) and H_2 (black squares) at 77 K and 1 bar for **CC16**. Closed symbols show adsorption and open symbols show desorption isotherms respectively. (b) PSD for **CC16** using N_2 as a probe gas.

Schneider *et al.* previously investigated the influence of peripheral groups on the porosity of POCs by incorporating salicyldialdehydes with a range of substituents at the 4-position.[2] In the crystalline state, the general trend was that with increased steric demand of the substituent, the accessible BET surface area substantially decreased. This was rationalised to be a consequence of the cage molecules packing more tightly together and subsequently blocking the pore windows. These observations, along with those for **CC16**, show that even minor alterations to the structure of the cage precursors can induce significant changes in the gas sorption properties exhibited by the resultant cage. Based on this, other 4,5-substituted CHDA derivatives possessing groups of diverse steric and electronic characteristics may lead to the preparation of porous materials with even greater accessible surface areas or tunable gas sorption properties.

4.4 Synthesis and Characterisation of Porous Organic Cage CC17

(1*R*,2*R*,4*S*,5*S*)-1,2-Diaminocyclohexane-4,5-diol is particularly interesting as a precursor for POC synthesis because its two hydroxyl groups could potentially favour the binding of Lewis acidic CO_2 molecules. Therefore, this POC may possess selective gas sorption properties. In addition, the presence of hydroxyl groups on the cage periphery could afford it as a candidate for PSM, which has been rarely explored while retaining the original imine bonded cage structure. To the best of our knowledge, the lone example is provided by Schneider *et al.*, who focussed on the etherification of hydroxyl groups that pointed into the cage cavity and which resulted in a loss in accessible surface area.[7] Most examples of PSM start with the reduction of the imine bond to a secondary amine, which may then be followed by acylation to form dodecaamide cages,[18] metalation to construct a MOF[19] or "tying" with aldehydes or ketones in order to regenerate the shape-persistency of the cage.[20]

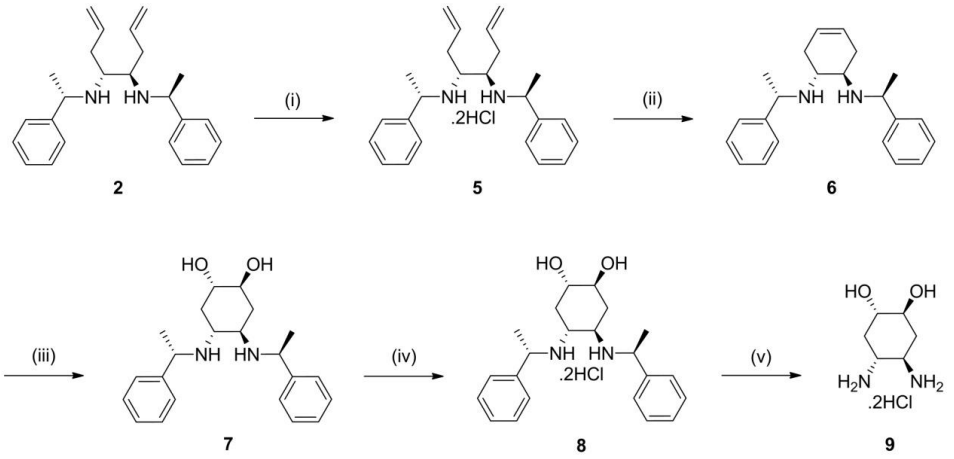

Scheme 4.2 Reaction scheme for the synthesis of (1*R*,2*R*,4*S*,5*S*)-1,2-diaminocyclohexane-4,5-diol, **9**. Reaction conditions: (i) 2 M HCl, DCM, rt, 100 %. (ii) Grubbs cat., DCM then 1 M NaOH, 40 °C, 89 %. (iii) TFA, *m*CPBA, DCM then Na_2SO_3, Na_2CO_3, rt, 70 %. (iv) 2 M HCl, CH_3OH, rt, 97 %. (v) $Pd(OH)_2/C$, H_2, CH_3OH, rt, 98 %.

The diol diamine **9** was synthesised according to a recently published procedure (Scheme 4.2).[21] The first step involved **2** being transformed into its diamine salt **5**, which then underwent ring-closing metathesis to give the cyclohexenediamine salt.[22] This was free-based and purified by flash column chromatography to yield the free cyclohexenediamine **6** in an 89 % yield. Treatment of **6** with *meta*-chloroperbenzoic acid (*m*CPBA) and trifluoroacetic acid (TFA) resulted in diastereoselective *anti*-dioxylation to **7** through epoxidation of the carbon-carbon double bond, followed by *in-situ* ring opening to afford the desired diol in a 70 % yield after flash column chromatography.[21] Consecutive dihydrochloride salt formation and hydrogenolysis of the chiral diamine auxiliary resulted in the isolation of the desired diamine salt **9**.

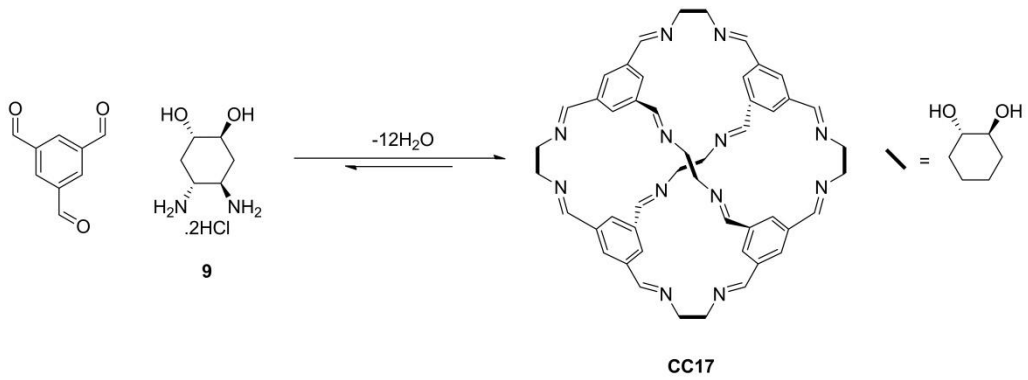

Scheme 4.3 Reaction scheme for the synthesis of **CC17**.

Following the procedure for the synthesis of **CC16**, the DCM-methanol solvent system proved to be unsuccessful using **9** as a precursor, with insoluble precipitate observable within minutes upon layering. Several solvent systems were attempted without success. However, using a 100 % methanol system appeared to slow the onset of precipitation. After four days, an amorphous solid, which also contained small crystals, had formed. These were subsequently solved by scXRD (performed by Dr Marc Little) to show that the desired [4+6] cage was present in the reaction mixture. **CC17** crystallised in the chiral tetragonal space group $P4_32_12$ and was heavily solvated with methanol and water molecules (Figure 4.7).

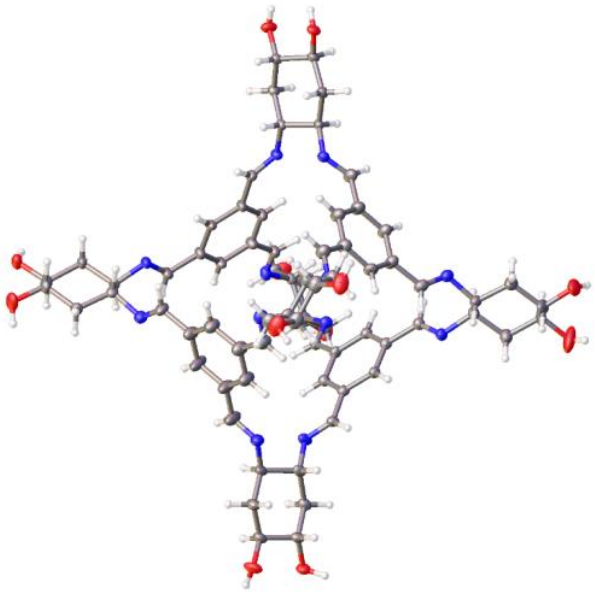

Figure 4.7 Displacement ellipsoid plot of the asymmetric unit from the single crystal structure **CC17**·$(CH_3OH)_{15.5}$·$(H_2O)_{13.25}$. Disordered CH_3OH and H_2O molecules omitted for clarity. Ellipsoids displayed at 50 % probability level.

Slowly reducing the volume of solvent in the reaction mixture under nitrogen flow afforded a powdery brown solid. The solubility of this material differed in comparison to previous cages synthesised within our group, with chlorinated solvents found to be unfavourable. Following a solubility screen, the cage was found to dissolve in DMF, DMSO, *N*-methyl-2-pyrrolidone (NMP) and 2,2,2-trifluoroethanol (TFE).

Analysis by ^{1}H NMR spectroscopy showed that the isolated product exhibited sharp singlets at δ 8.23 ppm and δ 7.82 ppm in a 1:1 ratio, which corresponded to the imine and aromatic protons respectively. However, the singlet at δ 4.79 ppm - assigned to

the hydroxyl groups - exhibited a noticeable shoulder peak and pronounced broadness. Analytical HPLC confirmed that in addition to a sharp peak assigned to **CC17** (t_R = 10.34 min), there were other broader peaks observable (Figure 4.8). This was rationalised to be soluble oligomeric and polymeric by-products which had precipitated from the original reaction mixture. This also goes some way to explain the amorphous character of the material observed upon PXRD analysis.

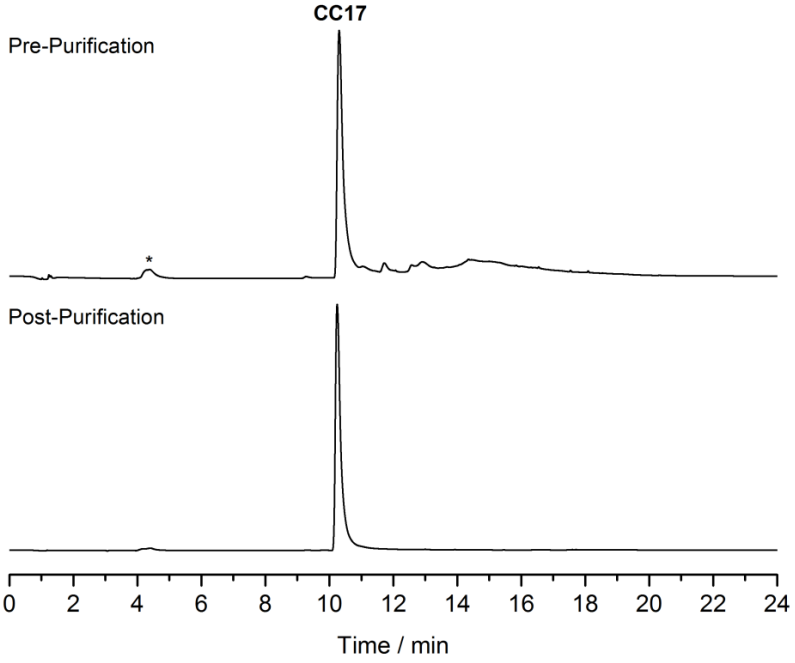

Figure 4.8 HPLC analysis for **CC17** before and after purification *via* preparative HPLC. Column: Syncronis C_8; 150 × 4.6 mm; 3 μm; mobile phase: CH_3OH-H_2O (10:90 to 90:10); flow: 0.5 mL min^{-1}; detection: λ = 254 nm; oven temperature = 30 °C. *DMSO solvent peak.

Preparative HPLC was employed to purify the crude product mixture. A sample of the crude product was dissolved in DMSO-methanol (2:1) and the desired diol cage **CC17** was isolated using a methanol-water gradient method. After the combined fractions were concentrated to dryness under vacuum, **CC17** was isolated as a white amorphous solid. However, the final recovery of **CC17** was poor, with an overall yield of only 17 %. Furthermore, the large quantities of solvent that were used to run the HPLC method made this approach to the isolation of **CC17** undesirable.

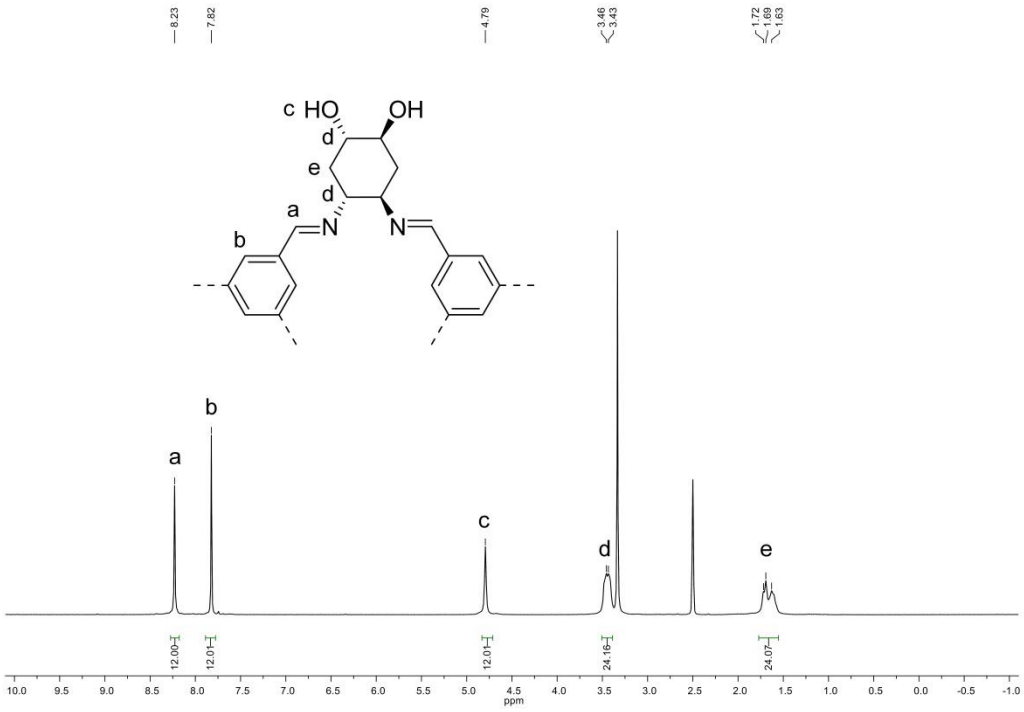

Figure 4.9 ^{1}H NMR spectrum (DMSO-d_6) of **CC17** after purification *via* preparative HPLC.

Despite the limitations of this method, analysis of the isolated material by ^{1}H NMR spectroscopy (Figure 4.9) showed that the broadness that was previously observed had now been removed. Sharp singlets at δ 8.23 ppm and δ 7.82 ppm in a 1:1 ratio could be assigned to the imine and aromatic protons respectively. In addition, the integration for the other peaks in the spectrum was consistent with the number of protons in the desired cage structure.

Analysis by MALDI-TOF mass spectrometry gave a molecular ion peak of *m/z* = 1310, which correlates to a [4+6] cage structure (Figure 4.10) and confirmed the observations from scXRD analysis.

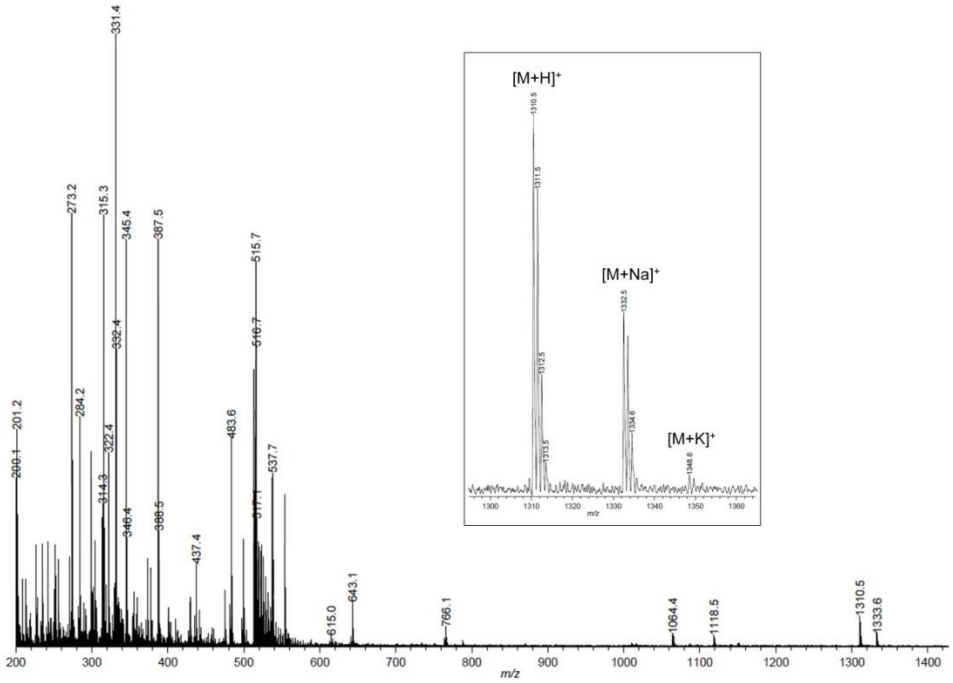

Figure 4.10 MALDI-TOF mass spectrum of **CC17** in DCTB/THF solution.

4.5 Synthesis and Characterisation of Porous Organic Cage CC18

The limitations of the initial approach towards the synthesis and isolation of **CC17** prompted a re-think as to how it could be prepared in a more efficient manner. One such strategy involved protecting the diol functionality, synthesising a cage with the resulting diamine derivative and then finally deprotecting to afford the hydroxyl-decorated cage. However, there are issues that need to be considered with this approach: (i) the initial protection strategy must be selective towards the diol functionality and not compete with the free secondary diamine; (ii) the chosen protecting group needs to be stable enough towards the conditions of further synthetic steps; (iii) the functionality of the protecting group cannot impede on successful cage formation, and; (iv) the solubility and stability of the resultant cage must be suitable for subsequent deprotection to the desired diol.

With this is mind, *tert*-butyldimethylsilyl (TBDMS) ethers were rationalised to be a suitable candidate. They preferentially react with alcohols over secondary amines, are stable towards hydrogenation conditions and their removal is well-explored, typically requiring a source of fluorine to effect cleavage.[23] In addition, the bulky alkyl groups on the resulting cage's periphery should ensure enhanced solubility

characteristics to aid the deprotection strategy employed, as well as increase the solubility of proto-cage fragments during POC synthesis.

The reaction of **7** with *tert*-butyldimethylsilyl chloride and imidazole led to the isolation of **10** in a yield of 89 % after flash column chromatography.[24] Hydrogenolysis to the free diamine **11** was achieved in a 99 % yield. This was then reacted with TFB to afford **CC18** (Scheme 4.4). After seven days, a white precipitate had been formed. In order to maximise the yield, the volume of solvent was reduced under vacuum and a white solid, **CC18**, was isolated by vacuum filtration in a 77 % yield after desolvation. The solubility of **CC18** was noticeably better than that of **CC16**, readily dissolving in chloroform and even in THF.

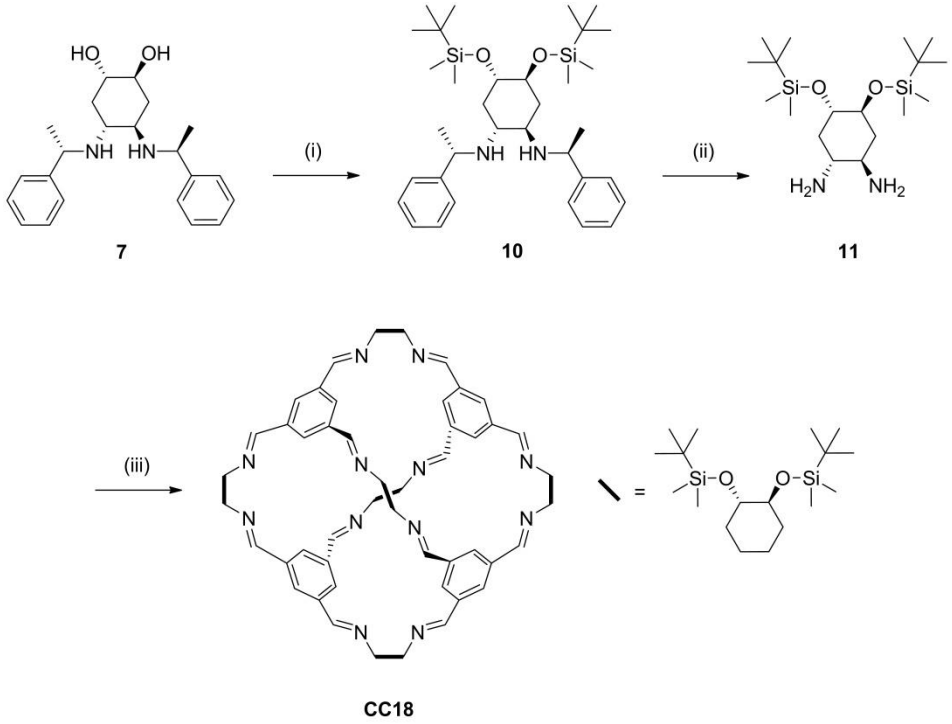

Scheme 4.4 Reaction scheme for the synthesis of **CC18**. Reaction conditions: (i) TBDMSCl, Imidazole, DCM, rt, 89 %. (ii) $Pd(OH)_2/C$, H_2, CH_3OH, rt, 99 %. (iii) TFB, DCM, rt, 77 %.

Analysis by ^1H NMR spectroscopy (Figure 4.11) showed that sharp singlets were observable at δ 8.06 ppm and δ 7.84 ppm, assigned to the imine and aromatic protons respectively. Furthermore, sharp singlets for the *tert*-butyl and dimethyl protons showed that the TBDMS protecting group had been retained in the final cage product.

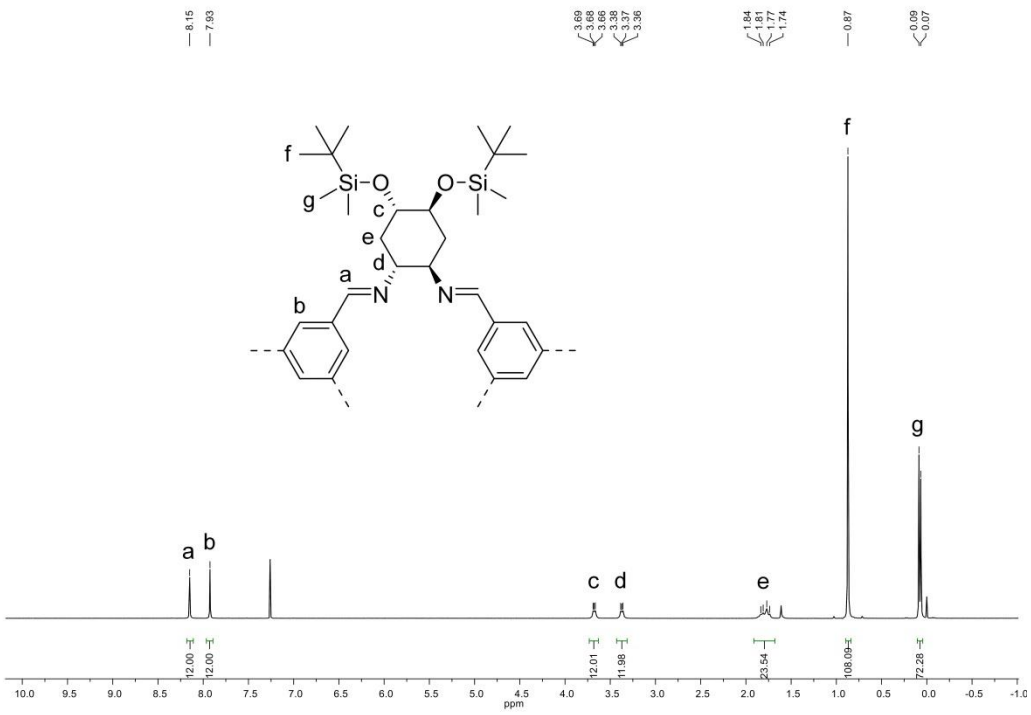

Figure 4.11 ^{1}H NMR spectrum ($CDCl_3$) of **CC18**.

Analysis by MALDI-TOF mass spectrometry gave a molecular ion peak of *m/z* = 2680, which correlates to the expected [4+6] cage structure (Figure 4.12), with no other cage species observable.

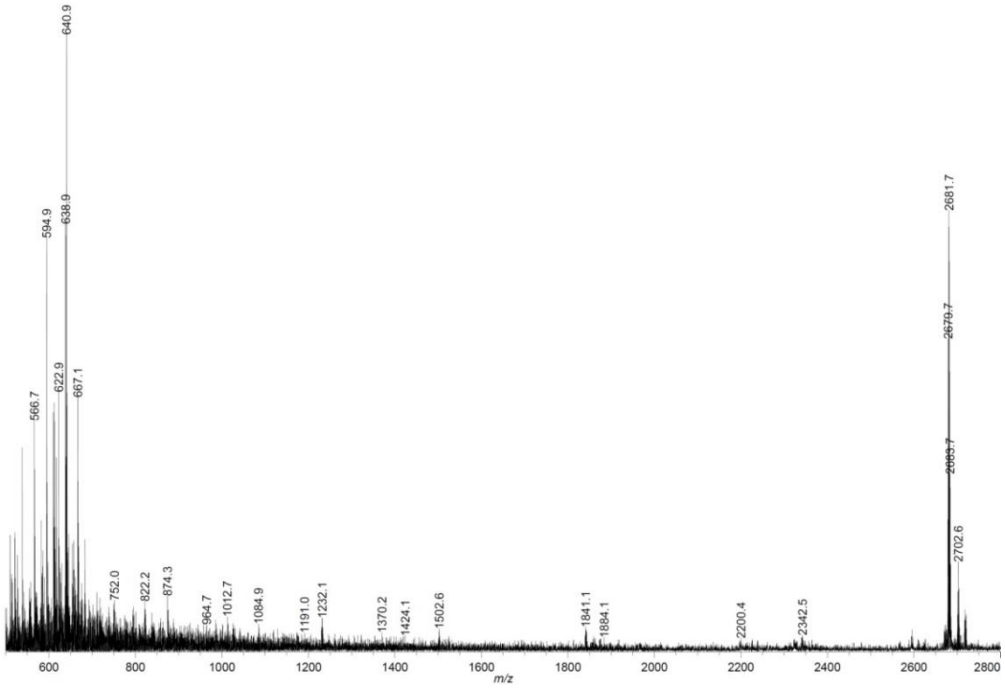

Figure 4.12 MALDI-TOF mass spectrum of **CC18** in DCTB/THF solution.

PXRD analysis showed that the as-synthesised desolvated material was not phase-pure, with the diffraction pattern exhibiting distinct regions of broadness and therefore indicating that it was amorphous in nature. Suitable crystals for scXRD analysis could not be grown despite screening various solvent combinations. This is not surprising, as the TBDMS groups are flexible and hence disordered with respect to one another. Gas sorption analysis of **CC18** was therefore conducted without prior crystallisation to a phase-pure material.

4.6 Gas Sorption Properties of CC18

Table 4.2 Gas sorption values for **CC18** at 1 bar.

	SA_{BET} / m^2 g^{-1}	N_2 / mmol g^{-1}	H_2 / mmol g^{-1}	CO_2 / mmol g^{-1}
	77 K		77 K	273 K
CC18	364	8.44	2.84	1.06

N_2 sorption measurements of **CC18** at 77 K and 1 bar showed a predominantly Type I isotherm with little uptake at low relative pressures (Figure 4.13a), resulting in an apparent BET surface area of 364 m^2 g^{-1} which is less than both **CC3** and **CC16**. The H_2 and CO_2 uptakes were also much lower in comparison (Table 4.2). Analysis of the PSD showed that in addition to the intrinsic cage cavity (14.5 Å), there are a range of pore sizes above 20 Å (Figure 4.13b). These mesopores arise due to the bulky TBDMS groups initiating inefficient packing between the cage molecules. This effect also helps to explain the hysteresis in the N_2 isotherm upon desorption, the observation of which is typically associated with materials containing mesopores. This behaviour can be understood by examining precedents in the literature. For a series of alkylated organic cages, Giri *et al.* discovered *via* scXRD analysis that the mobile alkyl tail ends could penetrate the cage cavity.[4] However, the introduction of bulky *tert*-butyl terminal branching groups prevented this phenomenon.[25] In the case of **CC18**, the TBDMS groups may not be penetrating adjacent cage cavities, but the shape of the isotherm suggests that they are generating larger pores, which may be disconnected, while occupying more of the space between the cage molecules and thus resulting in low gas uptake at lower pressures. However, without scXRD analysis, this conclusion is speculative.

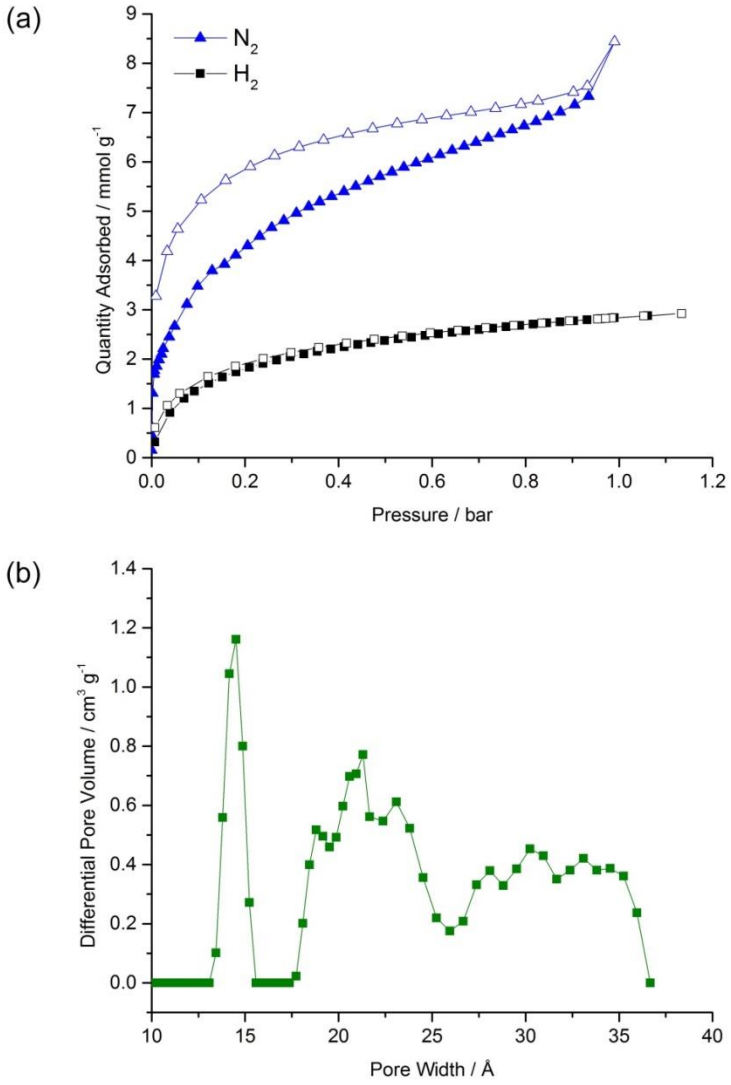

Figure 4.13 (a) Gas sorption isotherms for N_2 (blue triangles) and H_2 (black squares) at 77 K and 1 bar for **CC18**. Closed symbols show adsorption and open symbols show desorption isotherms respectively. (b) PSD for **CC18** using N_2 as a probe gas.

4.7 Deprotection and Isolation of CC17

A popular deprotection reagent for the removal of the TBDMS protecting group is tetrabutylammonium fluoride (TBAF), the use of which was pioneered by Corey and co-workers,[23] where the fluoride anion effects rapid cleavage of the silyl ether to the desired alcohol. Typically, the procedure is conducted at room temperature in THF. This is ideal because **CC18** is soluble in THF and the use of ambient conditions should limit any potential decomposition of the cage.

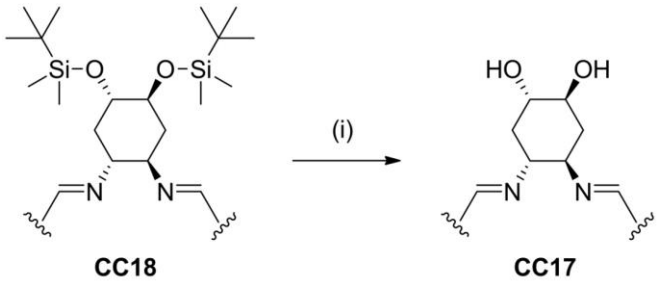

Scheme 4.5 Reaction scheme for the deprotection of **CC18**. Reaction conditions: (i) 1 M TBAF, THF then 1 M aq. NH_4Cl, rt, 51 %.

A solution of 1 M TBAF in THF, the amount of which equated to two equivalents of TBAF per protecting group, was added dropwise to a cooled solution of **CC18** in THF. Over a period of 24 hours, aliquots of the reaction mixture were taken and analysed by analytical HPLC. Over time, the intensity of the peak corresponding to **CC17**, whose retention time had been previously determined (Figure 4.8), increased until complete conversion had been achieved. After quenching with 1 M ammonium chloride, the THF solvent was removed under vacuum to leave a white suspension. Several attempts at purification *via* preparative HPLC failed, with impure material isolated each time. This was possibly due to side-products reacting with the methanol in the mobile phase and affecting the hydroxyl groups. It was found that by transferring the suspension to a centrifuge filter and successively washing with water-acetonitrile (95:5) and water, **CC17** could be isolated after residual water was removed *via* freeze-drying. This shows that the imine bonded cage architecture is stable towards excess basic TBAF, and is a rare example of a POC molecule undergoing PSM with retention of the imine bonds.

However, despite this relative success, especially in comparison to the previous method of isolation *via* preparative HPLC, there are drawbacks to this approach. Firstly, if water washing is not sufficient, then impurities can be retained. However, analysis of the filtrate showed that the cage is partially soluble in water, making it difficult to obtain material in high yield and purity. Secondly, conducting the deprotection on larger scales proved to be unsuccessful, as greater quantities of side-products made washing away impurities more difficult and typically led to the isolation of impure product in low yield. Thus, the isolation of **CC17** would benefit from a change in methodology. Alternative protection-deprotection strategies could be employed whereby more extreme acidic or basic conditions could be used to

induce cleavage of the protecting group. Reducing the imine bonded cage structure and post-synthetically "tying" has been shown to yield POCs which are not only porous, but show improved stability towards both acidic and basic conditions.[20] Of course, the preferred approach would be to find solvent conditions and a work-up procedure which would enable the synthesis of **CC17** using the original diol diamine precursor and therefore avoid additional synthetic steps.

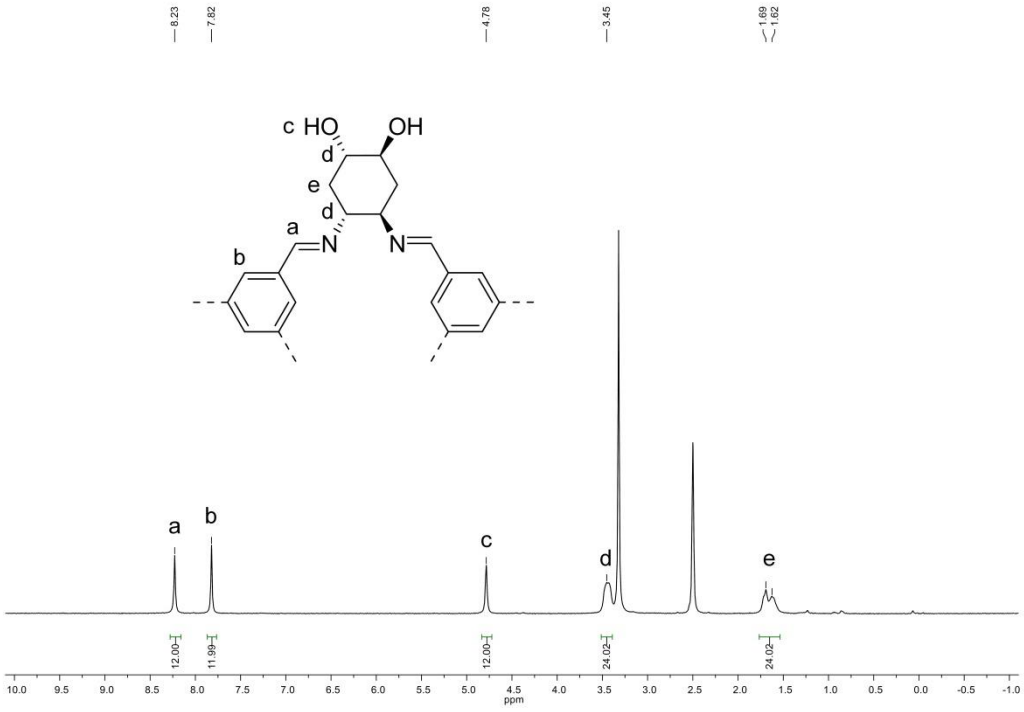

Figure 4.14 ^{1}H NMR spectrum (DMSO-d_6) of **CC17** after deprotection of **CC18**.

Analysis by ^{1}H NMR spectroscopy showed that the spectrum matched that of the material isolated *via* preparative HPLC (Figure 4.14). PXRD analysis revealed that the freeze-dried sample was amorphous. As both approaches had yielded amorphous material, attempts were made to crystallise **CC17**. Although single crystals could be isolated from solvent systems including TFE-THF and DMF-acetone, attempts to desolvate the cage structures through heating led to a loss of crystallinity. While DMF possesses a high boiling point, TFE is expected to hydrogen bond to the hydroxyl groups. Both factors make it difficult for the cage to retain its crystal packing mode upon desolvation. Activation of the material through solvent swapping, as demonstrated by Mastalerz and Oppel,[26] would be a better approach for future attempts. Following multiple reaction procedures, enough **CC17** was collected together to run gas sorption analysis on the desolvated amorphous sample.

4.8 Gas Sorption Properties of CC17

Table 4.3 Gas sorption values for **CC17** at 1 bar.

	SA_{BET} / m^2 g^{-1}	N_2 / mmol g^{-1}	H_2 / mmol g^{-1}	CO_2 / mmol g^{-1}
		77 K	77 K	273 K
CC17	423	7.06	4.15	1.81

N_2 sorption measurements of **CC17** at 77 K and 1 bar showed a Type I isotherm with a total uptake of 7.06 mmol g^{-1} and an apparent BET surface area of 423 m^2 g^{-1} (Table 4.3). The surface area is lower in comparison to crystalline samples of both **CC3** and **CC16**. This is despite the material being in the amorphous state, which has previously been shown to enhance the surface area of **CC3** due to inefficient cage packing.[16]

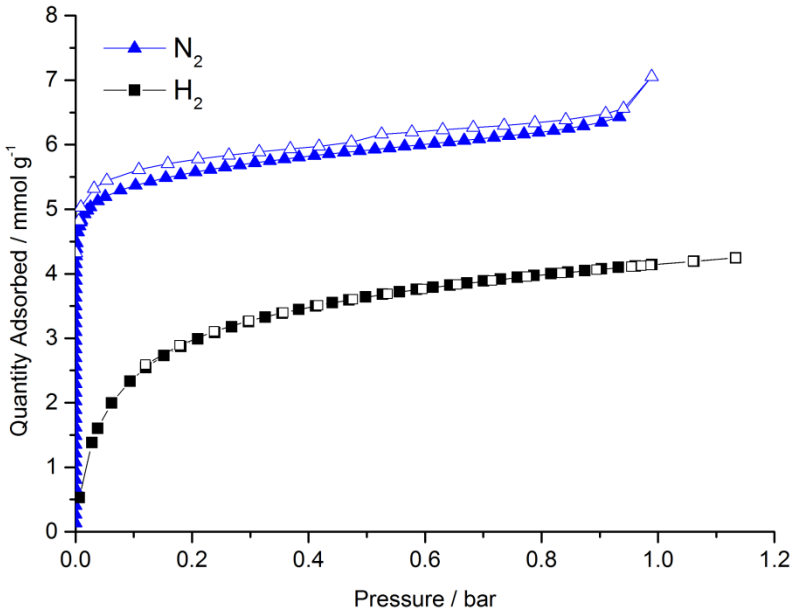

Figure 4.15 Gas sorption isotherms for N_2 (blue triangles) and H_2 (black squares) at 77 K and 1 bar for **CC17**. Closed symbols show adsorption and open symbols show desorption isotherms respectively.

Due to the large number of hydroxyl groups, it is possible that **CC17** could exhibit hygroscopic character and adsorb moisture upon exposure to air. If the activation conditions for gas adsorption are not appropriate, or the sample is exposed to air in between measurements, then any adsorbed water may block the pores and reduce the

accessible surface area. This is in turn may explain the reduced gas uptake values in comparison to other amorphous POC materials. Using TGA, the change in mass of a sample of **CC17** was measured as a function of temperature to investigate the effect of air exposure. The cage sample was initially heated up to 120 °C, held isothermally for one hour, cooled down to room temperature under either air or an inert nitrogen atmosphere, and then the method was repeated to evaluate whether any moisture had been adsorbed. A dried sample of **CC17** which had been left exposed to the atmosphere was shown to lose around 9 wt % upon heating, as indicated by the black line in Figure 4.16. This is due to the loss of water. After cooling under air and left standing for 20 minutes, repeating this cycle resulted in a similar observation, where around 11 wt % was lost upon heating (red line). This demonstrates the hygroscopic nature of the material. However, if the cage sample was kept under a nitrogen atmosphere throughout, little water uptake was observed (blue line). Based on these observations, activation of a **CC17** sample through heating under vacuum is an effective approach for the removal of all residual water. Maintaining an inert atmosphere between degassing and analysing the sample is also critical to ensure accurate gas uptake values. As care was taken to follow these conclusions during the measurements, the gas uptake values for **CC17** are deemed to be reliable.

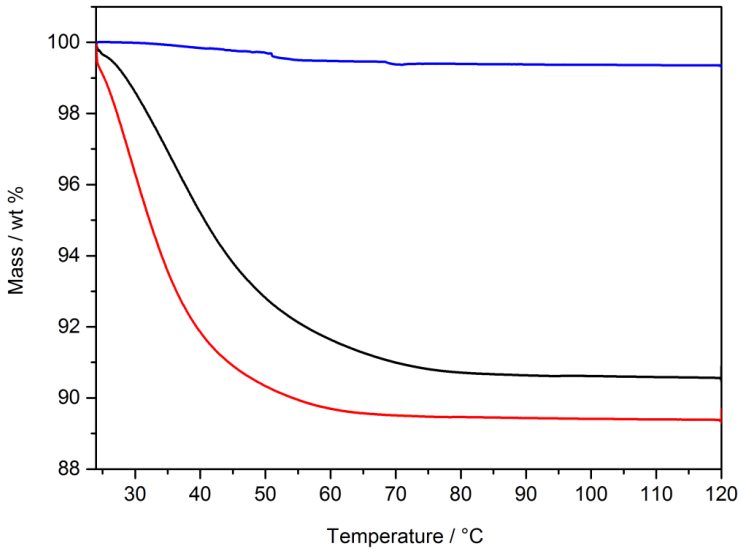

Figure 4.16 TGA data for a **CC17** sample which was successively exposed to air (black line), heated and cooled under air (red line) and then heated and cooled under a nitrogen atmosphere (blue line).

The decrease in surface area may therefore be a direct consequence of interactions between the hydroxyl groups on adjacent cage molecules. For **CC10**, a [4+6] cage possessing bis(4-fluorophenyl) vertices, analysis by scXRD found that hydrogen bonding between the peripheral fluorine atoms and C-H bonds effectively sealed the extrinsic pore channels to guest molecules, resulting in a loss of surface area in comparison to an analogous cage, **CC9**, which had biphenyl vertices with no fluorine present.[12] Therefore, hydrogen bonding interactions between the hydroxyl groups may be reducing the accessible surface area, rather than generating additional extrinsic porosity as in **CC16**.

This feature may rationalise the lack of improvement in CO_2 uptake for **CC17**. The presence of polar hydroxyl groups would be expected to promote the adsorption of Lewis acidic CO_2 molecules. This was demonstrated by Schneider *et al*., who showed that by replacing interior hydroxy groups with methoxy ones, the decrease in polarity resulted in a loss in CO_2 uptake, as well as a decrease in the isosteric heat of adsorption.[7] In the case of **CC17**, if the CO_2 cannot access these polar groups, then no noticeable improvement is likely to be observed. Only scXRD analysis would be able to definitively confirm this conclusion.

4.9 Synthesis and Characterisation of Porous Organic Cage CC19

9,10-Dihydro-9,10-ethanoanthracene-11,12-diamine (**12**) has been investigated with respect to a number of different applications, including its use as a chiral backbone in ligands for asymmetric catalysis[27] and as a component in chiral stationary phases for HPLC.[28]

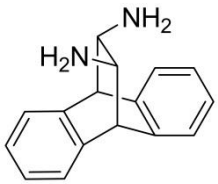

12

Figure 4.17 Structure of 9,10-dihydro-9,10-ethanoanthracene-11,12-diamine (**12**).

With respect to other POCs, **12** was previously explored within our research group as a precursor towards their synthesis, but successful cage formation was not achieved. This diamine is of particular interest, as the ethanoanthracene group could

conceivably frustrate the molecular packing to an even greater extent than that observed for **CC16** and potentially lead to superior gas sorption properties. Recently, Kohl *et al.* utilised **12**, along with other aromatic diamines, in the preparation of a series of shape-persistent triptycene derivatives.[29] These were found to possess high internal molecular free volumes and therefore pack inefficiently in the solid state. The introduction of **12** resulted in denser packing and a lower apparent BET surface area of 293 m^2 g^{-1} compared to less sterically-endowed analogues. This was rationalised on the basis of a difference in its molecular geometry.

A cage synthesis screen was conducted using TFB and the (*S*)-enantiomer of **12**, which was purchased from TCI-UK. The screen was carried out with mainly chlorinated solvents over a range of concentrations, with or without the presence of an acid catalyst or activated molecular sieves. Analysis of the reaction mixtures by ^{1}H NMR spectroscopy showed consumption of the aldehyde, with multiple imine and aromatic proton environments indicating that a number of different species were present. The equilibrium of the reaction could be shifted towards a single product using DCM as a solvent, along with a catalytic amount of TFA. Other species were still observable under these conditions but were less prominent. Despite the presence of these undesired species, they could be efficiently removed by swapping the solvent to acetone. With the impurities remaining in solution, the pure cage product **CC19** precipitated as a white solid and was isolated in a 33 % yield.

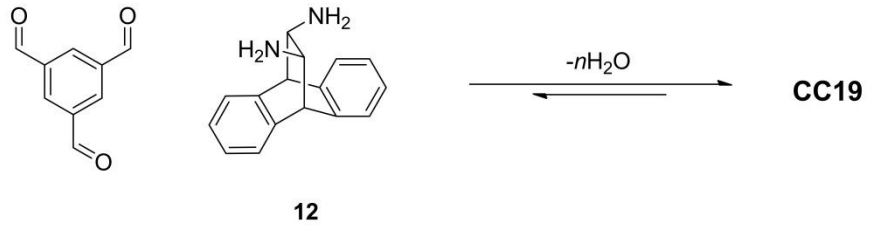

Scheme 4.6 Reaction scheme for the synthesis of **CC19**.

Analysis by ^{1}H NMR spectroscopy confirmed the isolation of the pure cage, with sharp singlets at δ 8.28 ppm and δ 7.80 ppm confirming the presence of imine and aromatic protons respectively in a 1:1 ratio (Figure 4.18). In addition, two singlets at δ 4.09 ppm and δ 3.75 ppm could be assigned to the protons (Ar-C*H* and C*H*-N) at the bridgehead positions.

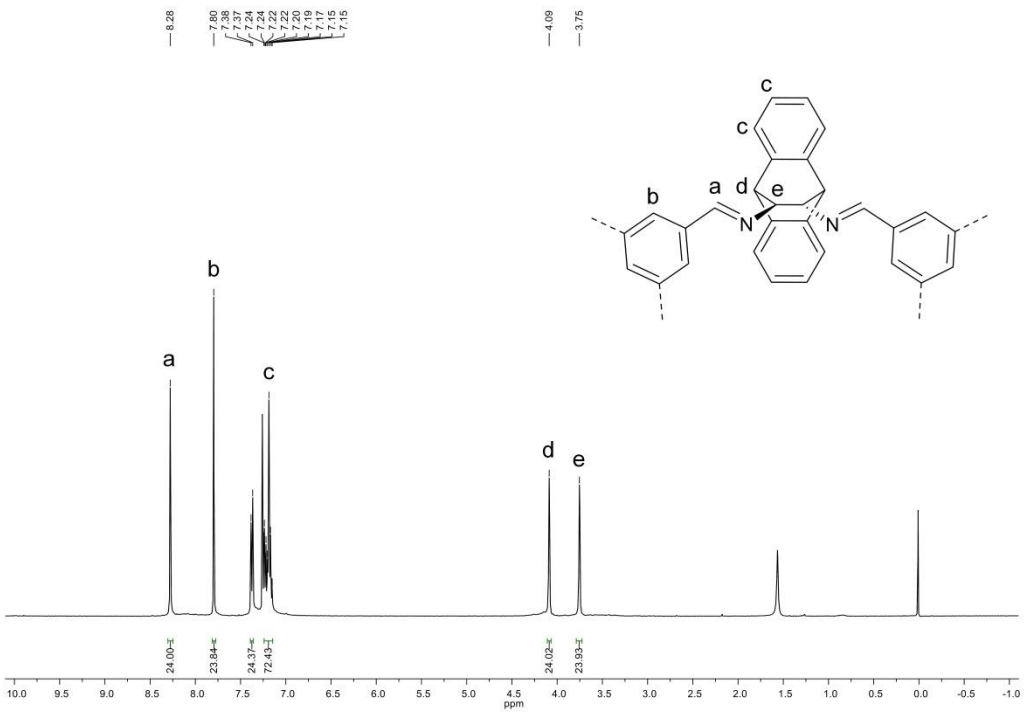

Figure 4.18 ^{1}H NMR spectrum ($CDCl_3$) of **CC19**.

Unfortunately, analysis by MALDI-TOF mass spectrometry was inconclusive, with molecular ion peaks of only very weak intensity observable.

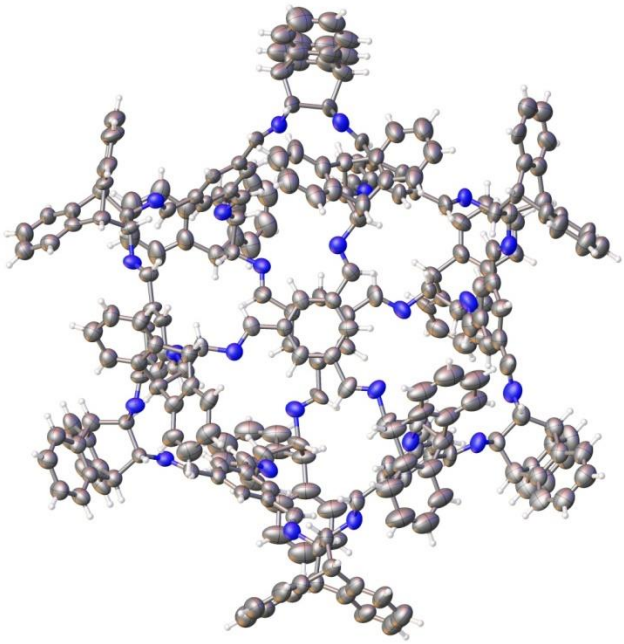

Figure 4.19 Displacement ellipsoid plot from the single crystal structure **CC19**·$(CH_2Cl_2)_{60}$. CH_2Cl_2 solvent omitted for clarity. Ellipsoids displayed at 30 % probability level.

CC19 was initially isolated as an amorphous material, as confirmed by PXRD analysis. Crystallisation of the cage from DCM-acetone (vial-in-vial) gave needle-like crystals which were characterised by scXRD (performed by Dr Marc Little; Figure 4.19). **CC19** crystallised in the chiral trigonal space group *P*321 and was found to be a cage comprised of eight molecules of TFB and twelve molecules of the (*S*,*S*)-diamine.

Imine bond-based cages possessing an [8+12] stoichiometry are rare and none have yet been proven to be porous in the solid state. This is typically due to a lack of shape-persistency upon desolvation. An early example was presented by Xu *et al.*, who synthesised a polyimine chiral nanocube using an edge-directed approach, where eight tritopic C_3-triformylcyclobenzylene units were linked together by twelve linear aromatic diamines.[30] Although crystals suitable for scXRD could not be obtained, its structure was elucidated through DOSY and MD calculations and was found to possess a molecular diameter of 3.7 nm. Skowronek *et al.* synthesised a large cuboctahedral [8+12] cage from the reaction of *cis*,*cis*-1,3,5-triaminocyclohexane and 4-*tert*-butyl-2,6-diformylphenol.[31] The resultant cage was determined by scXRD to have a large intrinsic cage cavity and an outer diameter of 3.0 nm. However, a desolvated structure was not reported. Jelfs *et al.* used an extended building block approach in the preparation of two large [8+12] cage molecules, **CC7** and **CC8**, which were synthesised from the reaction of an extended trialdehyde with an amine core, tri(4-formylphenyl)amine, with (*R*,*R*)-1,2-cyclohexanediamine and (*R*,*R*)-1,2-cyclohexenediamine respectively.[32] Although successfully characterised by scXRD and displaying inner and outer diameters of 1.5 nm and 2.9 nm respectively, rapid solvent loss and subsequent instability of the **CC7** crystals upon removal from the reaction mixture resulted in structural collapse to an amorphous material. The collapse of these larger cavities upon desolvation was rationalised to be due to the inherent flexibility of the bonds, with the loss of void space promoted by favourable π-π stacking interactions between opposing aromatic faces.

Interestingly, the stoichiometry of the most thermodynamically stable cage product can also be altered depending on the diamine choice. Using (*R*,*R*)-1,2-cyclopentanediamine, instead of (*R*,*R*)-1,2-cyclohexanediamine as for **CC7**, in conjunction with tri(4-formylphenyl)amine yields **CC5**, a [4+6] cage which is stable

towards desolvation and exhibits an apparent BET surface area of 1333 m^2 g^{-1}.[33] This behaviour was rationalised on the basis of subtle differences in bond angle between the respective cage vertices, which when amplified through a larger multi-component structure can result in significant changes to the final cage stoichiometry. In the case of **CC19**, this is the first example of an [8+12] imine bond-based cage prepared from the TFB precursor. This occurrence may again be due to a difference in bond angle, with **12** possessing the correct geometry to enable the preferential self-assembly of a larger cage containing more components.

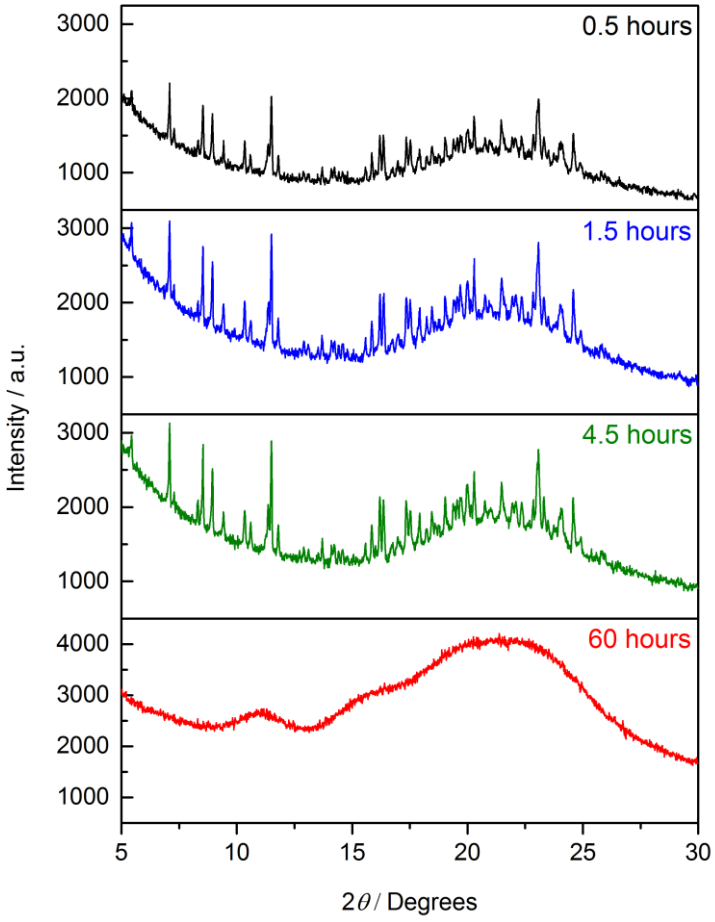

Figure 4.20 PXRD data monitoring the structural changes for **CC19** when exposed to air at room temperature.

As **CC7** was found to collapse to an amorphous state upon solvent loss, solvated crystals of **CC19** prepared from DCM-acetone (vial-in-vial) were packed into an open capillary. Powder patterns were then run successively to monitor any structural changes (performed by Dr Sam Chong). The crystallinity of the sample was retained

over a short period of time (Figure 4.20). However, after sixty hours, the sample was observed to be amorphous due to presumed structural rearrangement upon solvent loss. Solvent exchange using *n*-pentane, which has been successfully utilised for the activation of other large cages with retention of shape-persistence, also proved to be unsuccessful. This demonstrated that the crystallinity could not be retained during a gas sorption measurement, as the cage would not survive the activation conditions, however mild the approach. Furthermore, these observations infer that the inherent flexibility of imine bonds is unsuitable for the construction of large organic cages. According to Jelfs *et al*., there are a number of design features which should be considered in order to prevent structural collapse, including: (i) preventing rotation in the plane of the cage face; (ii) using larger polyaromatic building blocks to promote rigidity, and; (iii) discouraging non-covalent interactions which favour cage collapse.[32]

Recently, Zhang *et al.* reported the synthesis of an [8+12] cage composed of boronate ester bonds. The reaction of a tetraol precursor with a triboronic acid afforded a mesoporous cage with an internal cavity size of 2.3 nm that could be activated by solvent exchange.[34] The apparent BET surface area of 3758 $m^2 g^{-1}$ is the highest measured to date for this class of porous material. This result endorsed the recommendations of Jelfs *et al*. by highlighting the importance of structural rigidity, with the cage's fixed bonds and cuboctahedral geometry playing a vital role in its shape-persistency,[35] as well as the use of appropriate conditions to activate the material. Therefore, any future approach towards the synthesis of large cages must keep these factors in mind.

4.10 Gas Sorption Properties of CC19

Table 4.4 Gas sorption values for **CC19** at 1 bar.

	SA_{BET} / $m^2 g^{-1}$	N_2 / mmol g^{-1}	H_2 / mmol g^{-1}	CO_2 / mmol g^{-1}
	77 K		77 K	273 K
CC19	10	0.45	2.61	1.03

N_2 sorption measurements of **CC19** at 77 K and 1 bar mirrored the observations for the collapsed cage structures, **CC7** and **CC8**, in that it was formally non-porous (Figure 4.21). This suggests the collapse of the cage structure upon desolvation. On

the other hand, **CC19** was found to adsorb small amounts of H_2 and CO_2 (Table 4.4), indicating that the sterically-demanding ethanoanthracene vertices may generate pores of appropriate size to allow the adsorption of smaller gas molecules.

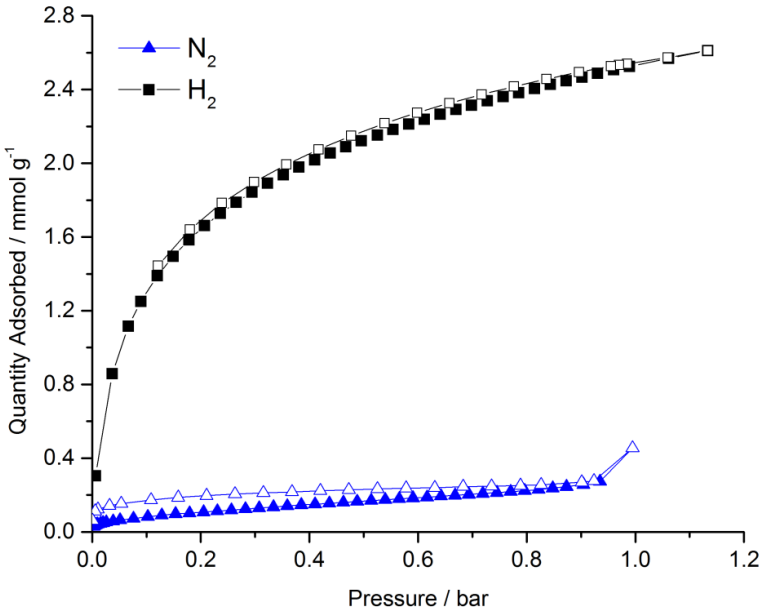

Figure 4.21 Gas sorption isotherms for N_2 (blue triangles) and H_2 (black squares) at 77 K and 1 bar for **CC19**. Closed symbols show adsorption and open symbols show desorption isotherms respectively.

4.11 Conclusions and Outlook

Enantiomerically-pure derivatives of the POC precursor CHDA were prepared, or purchased from a commercial source, and successfully reacted with TFB in the synthesis of four new POC molecules. **CC16** was isolated as a phase-pure [4+6] cage using (1*R*,2*R*,4*R*,5*R*)-1,2-diamino-4,5-dimethylcyclohexane (**4**) as the precursor. The introduction of methyl groups onto the cage's periphery resulted in frustrated molecular packing and generated an extra pore channel in addition to the 3-D diamondoid pore network running through the intrinsic cage voids. This subtle structural alteration resulted in an improvement in gas sorption properties in comparison to its parent cage **CC3**, with an apparent BET surface area of 1023 $m^2\ g^{-1}$ among the highest measured to date for this class of porous material. On the other hand, the utilisation of (1*R*,2*R*,4*S*,5*S*)-1,2-diaminocyclohexane-4,5-diol (**9**) in POC synthesis, in an effort to replace the methyl groups with hydroxyls, proved

problematic. The direct preparation of **CC17** was difficult to control and resulted in co-precipitation of crystalline cage and amorphous oligomeric material. Although pure **CC17** could be subsequently isolated by preparative HPLC, low recovery and high solvent consumption prompted a change in direction with regards to its preparation. By adopting a protection-deprotection strategy, the hydroxyl groups of **9** were converted to TBDMS ethers and the resulting diamine (**11**) was successfully used in the synthesis of **CC18**. This cage showed no real improvements with respect to gas sorption properties, although its superior solubility enabled successful deprotection and the isolation of pure **CC17**. Despite this being achieved in an average yield and on small scales, this is a rare example of PSM being performed on a POC molecule. Analysis of the gas sorption properties of this cage in the amorphous state failed to show any selectivity towards a particular gas. This was rationalised on the effect of hydrogen bonding interactions between the hydroxyl groups reducing the accessible surface area, instead of frustrating the molecular packing and improving it, as was the case with the methyl groups in **CC16**. Attempts to characterise desolvated crystals of **CC17** also proved unsuccessful due to a loss of crystallinity upon thermal treatment. Finally, using (11*S*,12*S*)-9,10-dihydro-9,10-ethanoanthracene-11,12-diamine (**12**) as a precursor, an [8+12] cage, **CC19**, was successfully isolated as one of the biggest imine bond-based cages prepared to date. Due to the inherent flexibility of the bonds, structural collapse upon desolvation rendered it amorphous and consequentially non-porous. Despite this, its synthesis provides additional evidence regarding the need for appropriate rigidity and geometry towards large, shape-persistent organic cage structures.

The synthesis and impressive gas sorption properties of **CC16** highlights how small changes in structure can trigger improvements in porosity. Introducing other functional groups at the 4,5[36] or even 3,6 positions[37] of CHDA in the synthesis of other POCs would allow further investigation of this effect and may result in superior materials. Although the isolation of **CC17** proved to be non-trivial, it is still an interesting material, and opens up possibilities for tuning the gas sorption properties or targeting a specific hybrid material or application through PSM.[38] Isolating it as a phase-pure material will prove to be important, as the gas sorption properties in the amorphous state were not particularly significant. This will involve finding a better approach to its synthesis, either by developing conditions that would allow a

controlled synthesis using the original diol diamine, or by using an alternative protection-deprotection strategy. POC molecules which have been post-synthetically tied have shown improved stabilities towards conditions that may enable a more effective approach. Due to **CC17** being soluble in mainly high boiling point solvents, activation upon crystallisation may also benefit from a methodology which puts less stress on the cage structure, with solvent swapping or supercritical drying potentially being more appropriate.[39]

4.12 Experimental

4.12.1 Materials

(*S*)-1-Phenylethylamine, 20 % palladium hydroxide on carbon and (11*S*,12*S*)-9,10-dihydro-9,10-ethanoanthracene-11,12-diamine were purchased from TCI-UK. TFA was purchased from Alfa Aesar. *m*CPBA was purchased from Fluorochem and TFB was purchased from Manchester Organics. Allyl bromide and triethylamine were purchased from Alfa Aesar and distilled prior to use. All other reagents were purchased from Sigma Aldrich and all reagents, with the exception of allyl bromide and triethylamine, were used as received. Hydrogen gas (99.995 % minimum; L05410A) was supplied by BOC gases.

4.12.2 Syntheses

N,N'-Bis-[(*S*)-1-phenylethyl]ethanediimine (1)[13]

A mixture of glyoxal trimer dihydrate (2.13 g, 10.2 mmol), anhydrous magnesium sulfate (4.60 g) and (*S*)-1-phenylethylamine (2.46 g, 20.3 mmol) in anhydrous DCM (20 mL) was stirred under a nitrogen atmosphere at rt for 7 h. The yellow reaction mixture was filtered and the filtrate was concentrated to dryness under vacuum to yield **1** as a yellow oil (2.69 g, 100 %).

^{1}H NMR ($CDCl_3$, 400 MHz) δ 8.05 (2 H, s, 2 × C*H*=N), 7.34-7.21 (10 H, m, 10 × Ar*H*), 4.50 (2 H, q, 2 × Ph-C*H*), 1.57 (6 H, d, 2 × CH_3); ^{13}C NMR ($CDCl_3$, 100.6 MHz) δ 160.82, 143.72, 128.71, 127.37, 126.78, 69.81, 24.10; IR (ν_{max}/cm^{-1}) 3028, 2971, 2927, 2864, 1626, 1596, 1493, 1452, 1369, 1271, 1079, 1011, 928; ESI-MS: *m/z* 265 $[M+H]^+$.

_N,N'_-Bis-[(_S_)-1-phenylethyl]-(_R,R_)-4,5-diamino-1,7-octadiene (2)

With stirring, zinc powder (3.29 g, 50.3 mmol) was heated for 5 min at 150 °C under a nitrogen atmosphere. Once cooled to rt, anhydrous THF (15 mL) and allyl bromide (2.73 g, 22.6 mmol) were added and the reaction mixture stirred for 2 h. After this time, stirring was stopped and excess zinc powder allowed to deposit on the bottom of the flask. The allylzinc bromide solution was decanted using a syringe and added dropwise *via* syringe pump over 20 min to a stirred solution of **1** (1.99 g, 7.52 mmol) in anhydrous THF (20 mL) at -78 °C under a nitrogen atmosphere. The reaction mixture was stirred for a further 1.5 h and quenched with a solution obtained by mixing 1 M NH_4Cl (6 mL) and 30 % NH_4OH (6 mL). The organic phase was isolated and the aqueous phase extracted with ethyl acetate (3 × 30 mL). The organic phases were combined, dried over anhydrous magnesium sulfate, filtered and the filtrate concentrated to dryness under vacuum to afford the crude product as an orange solid. This was purified by column chromatography (hexane-ethyl acetate, 95:5 to 80:20) to yield **2** as a crystalline white solid (1.82 g, 70 %).

^{1}H NMR ($CDCl_3$, 400 MHz) δ 7.30-7.20 (10 H, m, 10 × Ar*H*), 5.45-5.36 (2 H, m, 2 × C=C*H*), 4.83-4.68 (4 H, m, 2 × C=CH_2), 3.74 (2 H, q, 2 × Ph-C*H*), 2.21-2.03 (6 H, m, 2 × CH_2 and 2 × C*H*-NH), 1.27 (6 H, d, 2 × CH_3); ^{13}C NMR ($CDCl_3$, 100.6 MHz) δ 146.52, 136.56, 128.34, 127.29, 126.86, 116.53, 56.65, 56.12, 35.07, 25.25; IR (ν_{max}/cm^{-1}) 3058, 2980, 2959, 2924, 2837, 1639, 1491, 1449, 1371, 1356, 1314, 1110, 988; ESI-MS: *m/z* 349 $[M+H]^+$.

_N,N'_-Bis-[(_S_)-1-phenylethyl]-(1_R_,2_R_,4_R_,5_R_)-1,2-diamino-4,5-dimethylcyclohexane dihydrochloride (3)[14]

To a mixture of bis-(cyclopentadienyl)zirconium (IV) dichloride (0.36 g, 1.23 mmol) and anhydrous diethyl ether (110 mL) was added *n*-butylmagnesium chloride (2 M in diethyl ether, 15.1 mL, 30.3 mmol). With stirring, the reaction mixture was stirred at rt under a nitrogen atmosphere for 30 min. After this time, a solution of **2** (2.11 g, 6.05 mmol) in anhydrous diethyl ether (10 mL) was added dropwise *via* syringe pump over 15 min and the resulting mixture was stirred for 48 h. The reaction was then quenched with a saturated solution of ammonium chloride (60 mL). The organic layer was separated and the aqueous layer was extracted with diethyl ether (3 × 60 mL). The combined organic layers were washed with brine (120 mL), dried

over anhydrous magnesium sulfate, filtered and the filtrate concentrated to dryness under vacuum to afford the crude product as a yellow oil. This was purified by column chromatography (hexane-ethyl acetate, 95:5 to 80:20) to afford a pale yellow oil (1.59 g). This was dissolved in DCM (5 mL) and HCl (4 M in dioxane, 2.38 mL, 9.53 mmol) was added dropwise. After stirring at rt for 30 min, the resultant white precipitate was isolated by filtration and dried under vacuum to yield **3** as a powdery white solid (1.65 g, 64 %).

^{1}H NMR (D_2O, 400 MHz) δ 7.57-7.33 (10 H, m, 10 × Ar*H*), 4.47 (2 H, q, 2 × Ph-C*H*), 3.17 (2 H, m, 2 × C*H*-NH), 2.02-1.43 (6 H, m, 2 × CH_2 + 2 × C*H*-CH_3), 1.60 (6 H, d, 2 × CH_3), 0.98 (6 H, d, 2 × CH_3); ^{13}C NMR (D_2O, 100.6 MHz) δ 135.81, 131.08, 130.88, 128.30, 58.79, 53.78, 31.94, 29.76, 20.26, 19.08; IR (ν_{max}/cm^{-1}) 3421, 2933, 2749, 2460, 1646, 1572, 1456, 1382, 1056, 919; ESI-MS: *m/z* 351 $[M - Cl - HCl]^+$.

(1*R*,2*R*,4*R*,5*R*)-1,2-Diamino-4,5-dimethylcyclohexane dihydrochloride (4)

To an autoclave under a nitrogen atmosphere was added 20 % palladium hydroxide on carbon (0.32 g), **3** (0.96 g, 2.26 mmol) and methanol (75 mL). The reaction mixture was stirred vigorously at rt under hydrogen at 8 atmospheres pressure for 48 h. After this time, the reaction mixture was filtered through Whatman Microfibre GF/F filter paper and the autoclave rinsed with methanol. The rinses and filtrate were combined and concentrated to dryness under vacuum to yield **4** as a yellow-green solid (0.48 g, 99 %).

^{1}H NMR (CD_3OD, 400 MHz) δ 3.60 (2 H, m, 2 × C*H*-NH_2), 1.94-1.75 (4 H, m, 2 × CH_2), 1.52 (2 H, m, 2 × C*H*-CH_3), 1.04 (6 H, d, 2 × CH_3); ^{13}C NMR (CD_3OD, 100.6 MHz) δ 49.54, 32.77, 32.17, 19.30; IR (ν_{max}/cm^{-1}) 3421, 2877, 2597, 1559, 1489, 1384, 1355, 1055, 1028, 982; CI-MS: *m/z* 143 $[M - Cl - HCl]^+$.

***N*,*N'*-Bis-[(*S*)-1-phenylethyl]-(*R*,*R*)-4,5-diamino-1,7-octadiene dihydrochloride (5)**

With stirring, HCl (2 M in diethyl ether, 7.01 mL, 14.0 mmol) was added to a solution of **2** (2.33 g, 6.68 mmol) in DCM (8 mL), resulting in the precipitation of a white solid. After stirring at rt for 30 min, the reaction mixture was concentrated to dryness under vacuum to yield **5** as a powdery white solid (2.81 g, 100 %).

^{1}H NMR ($CDCl_3$, 400 MHz) δ 7.65-7.42 (10 H, m, 10 × Ar*H*), 4.96-4.86 (2 H, m, 2 × C=C*H*), 4.75-4.23 (4 H, m, 2 × C=CH_2), 4.36 (2 H, q, 2 × Ph-C*H*), 2.85-2.70 (4 H, m, 2 × CH_2), 2.53 (2 H, m, 2 × C*H*-NH), 1.99 (6 H, d, 2 × CH_3); ^{13}C NMR ($CDCl_3$, 100.6 MHz) δ 135.18, 130.89, 130.26, 130.08, 128.14, 121.32, 58.02, 53.57, 33.13, 20.73; IR (ν_{max}/cm^{-1}) 3523, 2641, 2431, 1594, 1561, 1454, 1387, 1340, 1209, 1063, 1025, 991; CI-MS: *m/z* 349 $[M - Cl - HCl]^+$.

_N,N'_-Bis-[(_S_)-1-phenylethyl]-(_R,R_)-1,2-diaminocyclohex-4-ene (6)[22]

A solution of **5** (1.49 g, 3.56 mmol) in anhydrous DCM (35 mL) was degassed for 15 min by substitution with nitrogen gas, at which point Grubbs 2nd Generation catalyst (0.12 g, 0.14 mmol) was added, and the reaction mixture was degassed for a further 5 min. The reaction mixture was stirred under reflux for 3 h under a nitrogen atmosphere. After this time, the reaction mixture was allowed to cool to rt and concentrated to dryness under vacuum to leave a brown solid. The residue was re-dissolved in water (40 mL), basified with 1 M NaOH and extracted with DCM (3 × 50 mL). The organic phases were combined, dried over anhydrous magnesium sulfate, filtered and the filtrate concentrated to dryness under vacuum to afford the crude product as a brown solid. This was purified by column chromatography (hexane-ethyl acetate, 95:5 to 80:20) to yield **6** as a white solid (1.01 g, 89 %).

^{1}H NMR ($CDCl_3$, 400 MHz) δ 7.35-7.21 (10 H, m, 10 × Ar*H*), 5.47 (2 H, m, 2 × C=C*H*), 3.87 (2 H, q, 2 × Ph-C*H*), 2.42 (2 H, m, 2 × C*H*-NH), 2.29 (2 H, m, 1 × CH_2), 1.84 (2 H, br. s, 2 × N*H*), 1.67 (2 H, m, 1 × CH_2), 1.34 (6 H, d, 2 × CH_3); ^{13}C NMR ($CDCl_3$, 100.6 MHz) δ 145.92, 128.58, 126.90, 126.79, 125.01, 54.81, 54.06, 31.93, 25.76; IR (ν_{max}/cm^{-1}) 3024, 2957, 2917, 1601, 1493, 1450, 1363, 1329, 1117, 1063, 1028, 1013; CI-MS: *m/z* 321 $[M+H]^+$.

_N,N'_-Bis-[(_S_)-1-phenylethyl)]-(1_R_,2_R_,4_S_,5_S_)-1,2-diaminocyclohexane-4,5-diol (7)[21]

TFA (4.27 g, 37.5 mmol) and then *m*CPBA (1.72 g, 7.49 mmol) were added to a solution of **6** (1.20 g, 3.74 mmol) in anhydrous DCM (6 mL). After stirring at rt for 4 h, a white precipitate was observable. The reaction mixture was quenched with a saturated solution of sodium sulfite (20 mL) and stirred for 10 min, at which point THF (20 mL) and 20 % w/v $Na_2CO_{3\ (aq)}$ (50 mL) were added and the reaction

mixture stirred for a further 2 h. After this time, the reaction mixture was extracted with ethyl acetate (3 × 80 mL) and the organic layers were combined and washed with 1 M NaOH (2 × 100 mL), dried over anhydrous magnesium sulfate, filtered and the filtrate concentrated to dryness under vacuum to afford the crude product as a white solid. This was purified by column chromatography (ethyl acetate-methanol, 100:0 to 85:15) to yield **7** as a flaky white solid (0.92 g, 70 %).

^{1}H NMR (CD_3OD, 400 MHz) δ 7.38-7.23 (10 H, m, 10 × Ar*H*), 3.86 (2 H, q, 2 × Ph-C*H*), 3.10 (2 H, m, 2 × C*H*-OH), 2.25 (2 H, m, 1 × CH_2), 2.01 (2 H, m, 2 × C*H*-NH), 1.33 (6 H, d, 2 × CH_3), 0.97 (2 H, m, 1 × CH_2); ^{13}C NMR (CD_3OD, 100.6 MHz) δ 146.41, 129.67, 128.18, 127.90, 74.17, 57.10, 56.00, 36.76, 25.25; IR (ν_{max}/cm^{-1}) 3295, 3060, 3025, 2958, 2922, 2863, 1602, 1493, 1451, 1369, 1120, 1063, 1006, 988; ESI-MS: *m/z* 355 $[M+H]^+$.

N_1,N'-Bis-[(*S*)-1-phenylethyl)]-(1*R*,2*R*,4*S*,5*S*)-1,2-diaminocyclohexane-4,5-diol dihydrochloride (8)

With stirring, HCl (2 M in diethyl ether, 2.58 mL, 5.16 mmol) was added to a solution of **7** (0.87 g, 2.46 mmol) in methanol (4 mL), resulting in the precipitation of a white solid. After stirring at rt for 30 min, the reaction mixture was concentrated to dryness under vacuum to yield **8** as a powdery white solid (1.02 g, 97 %).

^{1}H NMR (D_2O-CD_3OD, 400 MHz) δ 7.40-7.28 (10 H, m, 10 × Ar*H*), 4.51 (2 H, q, 2 × Ph-C*H*), 3.68 (2 H, m, 2 × C*H*-OH), 3.05 (2 H, m, C*H*-NH), 2.16 (2 H, m, 1 × CH_2), 1.77 (2 H, m, 1 × CH_2), 1.51 (6 H, d, 2 × CH_3); ^{13}C NMR (D_2O-CD_3OD, 100.6 MHz) δ 135.06, 131.06, 130.89, 128.30, 69.28, 57.88, 53.12, 25.15, 20.71; IR (ν_{max}/cm^{-1}) 3112, 2630, 2503, 1567, 1474, 1447, 1382, 1317, 1274, 1214, 1074, 1038, 1020, 963; CI-MS: *m/z* 355 $[M - Cl - HCl]^+$.

(1*R*,2*R*,4*S*,5*S*)-1,2-diaminocyclohexane-4,5-diol dihydrochloride (9)

To an autoclave under a nitrogen atmosphere was added 20 % palladium hydroxide on carbon (0.61 g), **8** (0.75 g, 1.75 mmol) and methanol (60 mL). The reaction mixture was stirred vigorously at rt under hydrogen at 8 atmospheres pressure for 48 h. After this time, the reaction mixture was filtered through Whatman Microfibre GF/F filter paper and the autoclave rinsed with water and methanol. The rinses and

filtrate were combined and concentrated to dryness under vacuum to yield **9** as a brown solid (0.38 g, 98 %).

^{1}H NMR (D_2O, 400 MHz) δ 3.65 (4 H, m, 2 × C*H*-OH + 2 × C*H*-NH_2), 2.42 (2 H, m, 1 × CH_2), 1.70 (2 H, m, 1 × CH_2); ^{13}C NMR (D_2O-CD_3OD, 100.6 MHz) δ 71.18, 50.46, 34.01; IR (ν_{max}/cm^{-1}) 3241, 2808, 2724, 2595, 2546, 1613, 1589, 1570, 1536, 1402, 1269, 1110, 1065, 1032; CI-MS: *m/z* 147 $[M - Cl - HCl]^+$.

N,N'-Bis-[(*S*)-1-phenylethyl)]-(1*R*,2*R*,4*S*,5*S*)-1,2-diamino-4,5-di((tertbutyldimethylsilyl)oxy)cyclohexane (10)[24]

A solution of *tert*-butyldimethylsilyl chloride (0.86 g, 5.68 mmol) in DCM (2 mL) was added to a cooled solution of **7** (0.81 g, 2.27 mmol) and imidazole (0.39 g, 5.68 mmol) in DCM (6 mL). The reaction mixture was stirred at rt for 16 h. After this time, water (8 mL) was added. The organic phase was isolated and the aqueous phase extracted with DCM (3 × 15 mL). The organic phases were combined and washed with water (15 mL) and a saturated solution of sodium hydrogen carbonate (15 mL), dried over anhydrous magnesium sulfate, filtered and the filtrate concentrated to dryness under vacuum to afford the crude product as a white solid. This was purified by column chromatography (hexane-ethyl acetate, 93:7 to 50:50) to yield **10** as a white solid (1.18 g, 89 %).

^{1}H NMR ($CDCl_3$, 400 MHz) δ 7.34-7.24 (10 H, m, 10 × Ar*H*), 3.80 (2 H, q, 2 × Ph-C*H*), 3.18 (2 H, m, 2 × C*H*-O), 2.09 (2 H, m, 1 × CH_2), 1.95 (2 H, m, 2 × C*H*-NH), 1.33 (6 H, d, 2 × CH_3), 0.91 (2 H, m, 1 × CH_2), 0.85 (18 H, s, 6 × CH_3), 0.01 (6 H, s, 2 × CH_3), 0.00 (6 H, s, 2 × CH_3); ^{13}C NMR ($CDCl_3$, 100.6 MHz) δ 145.58, 128.64, 127.08, 126.84, 74.25, 55.73, 54.92, 37.68, 26.16, 25.42, 18.24, -3.85, -4.65; IR (ν_{max}/cm^{-1}) 2956, 2927, 2853, 1461, 1360, 1251, 1099, 1063, 1055, 923; CI-MS: *m/z* 583 $[M+H]^+$; CHN analysis for $C_{34}H_{58}N_2O_2Si_2$: C 70.04, H 10.03, N 4.80; found C 69.76, H 10.03, N 4.74.

(1*R*,2*R*,4*S*,5*S*)-1,2-Diamino-4,5-di((tertbutyldimethylsilyl)oxy)cyclohexane (11)

To an autoclave under a nitrogen atmosphere was added 20 % palladium hydroxide on carbon (0.81 g), **10** (2.00 g, 3.43 mmol) and methanol (145 mL). The reaction mixture was stirred vigorously at rt under hydrogen at 10 atmospheres pressure for 72 h. After this time, the reaction mixture was filtered through Whatman Microfibre

GF/F filter paper and the autoclave rinsed with methanol. The rinses and filtrate were combined and concentrated to dryness under vacuum to yield **11** as a colourless oil (1.27 g, 99 %).

^{1}H NMR ($CDCl_3$, 400 MHz) δ 3.48 (2 H, m, 2 × C*H*-O), 2.39 (2 H, m, 2 × C*H*-NH_2), 2.01 (2 H, m, 1 × CH_2), 1.29 (2 H, m, 1 × CH_2), 0.89 (18 H, s, 6 × CH_3), 0.08 (6 H, s, 2 × CH_3), 0.07 (6 H, s, 2 × CH_3); ^{13}C NMR ($CDCl_3$, 100.6 MHz) δ 74.47, 55.23, 41.11, 26.17, 18.24, -3.78, -4.58; IR (ν_{max}/cm^{-1}) 2952, 2928, 2856, 1578, 1472, 1388, 1360, 1250, 1104, 1065, 1005; ESI-MS: *m/z* 375 $[M+H]^+$.

CC16

To a solution of **4** (0.58 g, 2.70 mmol) in methanol (15 mL) was added triethylamine (0.55 g, 5.40 mmol) and the resulting solution was stirred for 20 min. After this time, the solution was layered slowly *via* Pasteur pipette onto a suspension of TFB (0.28 g, 1.74 mmol) in DCM (12 mL). The reaction mixture was sealed and left standing at rt for 5 d. After this time, the volume of the clear yellow reaction mixture was reduced under vacuum (< 20 °C) until precipitation was induced. The white precipitate was isolated by vacuum filtration, washed with methanol (2 × 5 mL) and dried under vacuum to yield **CC16** as a powdery white solid (0.44 g, 79 %).

^{1}H NMR ($CDCl_3$, 400 MHz) δ 8.16 (12 H, s, 12 × C*H*=N), 7.89 (12 H, s, 12 × Ar*H*), 3.54 (12 H, m, 12 × C*H*-N), 2.12 (12 H, m, 6 × CH_2), 1.83 (12 H, m, 6 × CH_2), 1.30 (12 H, m, 12 × C*H*-CH_3), 1.19 (36 H, d, 12 × CH_3); ^{13}C NMR ($CDCl_3$, 100.6 MHz) δ 159.64, 135.98, 129.50, 69.39, 32.77, 32.68, 19.52; IR (ν_{max}/cm^{-1}) 2960, 2922, 2875, 1647, 1457, 1376, 1156, 1099, 1001, 961; MALDI-TOF MS: *m/z* 1286 $[M+H]^+$; CHN analysis for $C_{84}H_{108}N_{12}$: C 78.46, H 8.47, N 13.07; found C 73.62, H 8.33, N 12.17.

CC17

Route 1. To a suspension of **9** (0.40 g, 1.83 mmol) in methanol (40 mL) was added triethylamine (0.37 g, 3.65 mmol) and the resulting solution was stirred for 20 min. After this time, the solution was layered slowly *via* Pasteur pipette onto a solution of TFB (0.19 g, 1.18 mmol) in methanol (40 mL). The reaction mixture was sealed and left standing for 5 d. After this time, both amorphous and crystalline precipitate was observable. The reaction mixture was concentrated to dryness under a nitrogen flow,

at which point the crude solid was washed with DCM-methanol (95:5, 2 × 10 mL), isolated by filtration and then dried under vacuum to yield the crude product as a brown solid (0.36 g, 94 %). Separate samples were combined, with the crude product (0.48 g) dissolved in DMSO-methanol (2:1, 24 mL), and the resulting solution was syringe filtered (0.45 μm) and purified by preparative HPLC. The product-containing fractions were concentrated to dryness under vacuum to yield **CC17** as a powdery white solid (0.11 g, 17 %).

Route 2.[40] With stirring, TBAF (1 M in THF, 0.90 mL, 0.90 mmol) was added dropwise to a cooled solution of **CC18** (0.10 g, 0.04 mmol) in THF (12 mL). After stirring at rt for 24 h, the reaction mixture was quenched with 1 M NH_4Cl (1.5 mL) and the THF was removed under vacuum (< 20 °C) to leave a white suspension. This was transferred to a Corning® Spin-X® UF centrifugal concentrator (30K MWCO) and the white precipitate was successively washed with water-acetonitrile (95:5, 12 mL) and water (3 × 12 mL). The collected white solid was suspended in a minimum amount of water and then freeze-dried for 2 d to yield **CC17** as a powdery white solid (0.03 g, 51 %).

^{1}H NMR (DMSO-d_6, 400 MHz) δ 8.23 (12 H, s, 12 × C*H*=N), 7.82 (12 H, s, 12 × Ar*H*), 4.79 (12 H, br. s, 12 × CH-O*H*), 3.44 (24 H, m, 12 × C*H*-OH + 12 × C*H*-N), 1.68 (24 H, m, 12 × CH_2); ^{13}C NMR (DMF-d_7, 100.6 MHz) δ 159.99, 137.11, 129.38, 73.50, 72.78, 39.43; IR (ν_{max}/cm^{-1}) 3358, 2929, 2866, 1646, 1449, 1378, 1325, 1160, 1110, 1037, 1007, 696, 919; MALDI-TOF MS: *m/z* 1310 $[M+H]^+$; CHN analysis for $C_{72}H_{84}N_{12}O_2$: C 66.04, H 6.47, N 12.84; found C 59.64, H 6.63, N 11.15.

CC18

A solution of **11** (0.64 g, 1.71 mmol) in DCM (28 mL) was added slowly *via* Pasteur pipette onto a solution of TFB (0.18 g, 1.10 mmol) in DCM (35 mL) and then left standing at rt for 7 d. After this time, a white precipitate was observable. The volume of DCM was reduced by half under vacuum (< 20 °C) and the precipitate isolated by vacuum filtration, washed with methanol (2 × 10 mL) and dried under vacuum to yield **CC18** as a powdery white solid (0.57 g, 77 %).

^{1}H NMR ($CDCl_3$, 400 MHz) δ 8.15 (12 H, s, 12 × C*H*=N), 7.93 (12 H, s, 12 × Ar*H*), 3.68 (12 H, m, 12 × C*H*-O), 3.37 (12 H, m, 12 × C*H*-N), 1.79 (24 H, m, 12 × CH_2), 0.87 (108 H, s, 36 × CH_3), 0.09 (36 H, s, 12 × CH_3), 0.07 (36 H, s, 12 × CH_3); ^{13}C NMR ($CDCl_3$, 100.6 MHz) δ 159.87, 136.54, 130.02, 74.38, 72.65, 40.25, 26.16, 18.25, -3.73, -4.59; IR (ν_{max}/cm^{-1}) 2953, 2929, 2857, 1648, 1472, 1388, 1251, 1164, 1053, 1006, 964; MALDI-TOF MS: *m/z* 2680 $[M+H]^+$; CHN analysis for $C_{144}H_{252}N_{12}O_{12}Si_{12}$: C 64.52, H 9.48, N 6.27; found C 63.03, H 9.43, N 6.13.

CC19

A solution of (11*S*,12*S*)-9,10-dihydro-9,10-ethanoanthracene-11,12-diamine (0.25 g, 1.06 mmol) in DCM (20 mL) was added slowly *via* Pasteur pipette onto a solution of TFB (0.11 g, 0.66 mmol) and a catalytic amount of TFA in DCM (20 mL). The reaction mixture was sealed and left standing at rt for 7 d. After this time, a small amount of white precipitate was observable. With stirring, the reaction mixture was diluted with DCM (40 mL) and quenched with excess sodium hydrogen carbonate. The suspension was filtered under vacuum and the filtrate reduced to a volume of 10 mL under vacuum (< 20 °C). Acetone (20 mL) was added and the reaction mixture stirred under ice for 20 min to leave a white turbid solution. This was reduced to a volume of 10 mL under vacuum (< 20 °C) and the precipitate was isolated by vacuum filtration, washed with cold acetone (2 × 5 mL) and dried under vacuum to yield **CC19** as a powdery white solid (0.10 g, 33 %).

^{1}H NMR ($CDCl_3$, 400 MHz) δ 8.28 (24 H, s, 24 × C*H*=N), 7.80 (24 H, s, 24 × Ar*H*), 7.38-7.15 (96 H, m, 96 × Ar*H*), 4.09 (24 H, s, 24 × Ar-C*H*), 3.75 (24 H, s, 24 × C*H*-N); ^{13}C NMR ($CDCl_3$, 100.6 MHz) δ 161.57, 142.37, 140.52, 136.85, 129.73, 126.16, 126.12, 125.66, 123.76, 77.37, 53.93; IR (ν_{max}/cm^{-1}) 3021, 2944, 2856, 1703, 1637, 1595, 1458, 1153, 1116, 1024, 965, 882; CHN analysis for $C_{264}H_{192}N_{24}$: C 85.69, H 5.23, N 9.08; found C 79.64, H 4.91, N 8.17.

4.13 Single Crystal X-ray Crystallography

4.13.1 Single Crystal Data for CC16

CC16 crystallised from a CH_2Cl_2-ethyl acetate solution in the chiral cubic space group $F4_132$. For this single crystal phase, the asymmetric unit comprises 1/12 of a **CC16** cage fragment. The cage molecule has tetrahedral symmetry (point group *T*).

Single crystals of **CC16** were very small and weakly diffracting. Synchrotron radiation was therefore required for structure solution. A 0.95 Å resolution limit was applied during refinement and the cage molecule was refined with a rigid body restraint (RIGU in SHELX). It was not possible to model any solvent positions in the lattice voids. Therefore, a solvent mask was used during the final stages of refinement.[41] This solvent masking routine removed a total of 1042 electrons from a 3557 $Å^3$ void, hence a total of 24 CH_2Cl_2 molecules were tentatively added to increase the atom count per unit cell, or 3 per **CC16** cage.

Crystal data for **CC16**·$(CH_2Cl_2)_3$: Formula $C_{87}H_{114}N_{12}Cl_6$; M = 1540.60 g·mol^{-1}; cubic space group $F4_132$, colourless prism shaped crystal; a = 26.28(2) Å; V = 18152(32) $Å^3$; ρ = 1.127 g·cm^{-3}; μ(synchrotron λ = 0.6889 Å) = 0.234 mm^{-3}; F (000) = 6576; crystal size = 0.08 × 0.05 × 0.05 mm^3; T = 100(2) K; 13890 reflections measured (1.30° < Θ < 21.23°), 941 unique (R_{int} = 0.0941), 732 ($I > 2\sigma(I)$); R_1 = 0.1983 for observed and R_1 = 0.2124 for all reflections; wR_2 = 0.4511 for all reflections; max/min residual electron density 0.562 and -0.510 e·$Å^{-3}$; data/restraints/parameters = 941/39/74; GOF = 3.397.

4.13.2 Single Crystal Data for CC17

CC17 crystallised from a CH_3OH solution in the chiral tetragonal space group $P4_32_12$. For this single crystal phase, the asymmetric unit comprises one complete **CC17** and a number of disordered and partially occupied CH_3OH and H_2O molecules. Two CH_3OH solvent molecules were refined with C-O bond length restraints (DIFX in SHELX). The data was not of sufficient quality to refine proton atom positions, in particular, the hydroxyl proton atoms. All proton atoms were therefore placed in geometrically estimated positions and refined using the riding model. Due to the disordered nature of the solvent, all solvent molecules were refined isotropically.

Crystal data for **CC17**·$(CH_3OH)_{15.5}$·$(H_2O)_{13.25}$: Formula $C_{87.5}H_{172.5}N_{12}O_{40.75}$; M = 2044.88 g·mol^{-1}; tetragonal space group $P4_32_12$, colourless needle shaped crystal; a = 22.417(2), c = 56.059(4) Å; V = 23368(3) $Å^3$; ρ = 1.162 g·cm^{-3}; μ(CuKα) = 0.768 mm^{-3}; F (000) = 8860; crystal size = 0.37 × 0.24 × 0.16 mm^3; T = 100(2) K; 237732 reflections measured (2.68° < Θ < 74.65°), 23923 unique (R_{int} = 0.0459), 22543 ($I > 2\sigma(I)$); R_1 = 0.0945 for observed and R_1 = 0.0975 for all reflections; wR_2 =

0.2705 for all reflections; max/min residual electron density after solvent mask had been applied = 0.822 and -0.742 e·Å^{-3}; data/restraints/parameters = 23923/2/1125; GOF = 1.069.

4.13.3 Single Crystal Data for CC19

CC19 crystallised from a CH_2Cl_2-acetone solution in the chiral trigonal space group *P*321. The asymmetric unit for this single crystal phase comprises 1/3 of an [8+12] cage molecule centred round a threefold rotation axis. It was not possible to accurately model the highly disordered solvent content that was contained within the large lattice voids. A solvent mask, which removed 5174 electrons from a 15562 Å^3 void, was therefore used during the final stages of refinement. A total of 60 CH_2Cl_2 solvent molecules were added to the refined formula unit per [8+12] cage. Due to slight disorder of the cage molecule during refinement, a number of aromatic rings were refined with rigid-body constraints (AFIX 66 in SHELX) and restraints (RIGU in SHELX).

Crystal data for **CC19**·$(CH_2Cl_2)_{60}$: Formula $C_{324}H_{312}Cl_{120}N_{24}$; M = 8795.96 g·mol^{-1}; trigonal space group *P*321, colourless needle shaped crystal; a = 31.774(2), c = 26.444(1) Å; V = 23120(2) Å^3; ρ = 1.264 g·cm^{-3}; μ(MoKα) = 0.742 mm^{-3}; F (000) = 8928; crystal size = 0.36 × 0.14 × 0.11 mm^3; T = 100(2) K; 116797 reflections measured (0.74° < Θ < 21.97°), 18859 unique (R_{int} = 0.0448), 11603 ($I > 2\sigma(I)$); R_1 = 0.0846 for observed and R_1 = 0.1159 for all reflections; wR_2 = 0.2756 for all reflections; max/min residual electron density 0.270 and -0.193 e·Å^{-3}; data/restraints/parameters = 18859/486/769; GOF = 1.098.

4.14 References

1. S. M. Elbert, F. Rominger and M. Mastalerz, *Chem. Eur. J.*, 2014, **20**, 16707-16720.
2. M. W. Schneider, I. M. Oppel, H. Ott, L. G. Lechner, H. J. Hauswald, R. Stoll and M. Mastalerz, *Chem. Eur. J.*, 2012, **18**, 836-847.
3. H. Ding, Y. Yang, B. Li, F. Pan, G. Zhu, M. Zeller, D. Yuan and C. Wang, *Chem. Commun.*, 2015, **51**, 1976-1979.
4. N. Giri, C. E. Davidson, G. Melaugh, M. G. Del Pópolo, J. T. A. Jones, T. Hasell, A. I. Cooper, P. N. Horton, M. B. Hursthouse and S. L. James, *Chem. Sci.*, 2012, **3**, 2153.
5. Y. Jin, B. A. Voss, R. McCaffrey, C. T. Baggett, R. D. Noble and W. Zhang, *Chem. Sci.*, 2012, **3**, 874.

6. R. McCaffrey, H. Long, Y. Jin, A. Sanders, W. Park and W. Zhang, *J. Am. Chem. Soc.*, 2014, **136**, 1782-1785.
7. M. W. Schneider, I. M. Oppel, A. Griffin and M. Mastalerz, *Angew. Chem.*, 2013, **52**, 3611-3615.
8. K. K. Tanabe and S. M. Cohen, *Chem. Soc. Rev.*, 2011, **40**, 498-519.
9. T. Ratvijitvech, R. Dawson, A. Laybourn, Y. Z. Khimyak, D. J. Adams and A. I. Cooper, *Polymer*, 2014, **55**, 321-325.
10. S. J. Garibay, M. H. Weston, J. E. Mondloch, Y. J. Colon, O. K. Farha, J. T. Hupp and S. T. Nguyen, *CrystEngComm*, 2013, **15**, 1515-1519.
11. Y. Zhang, B. Li and S. Ma, *Chem. Commun.*, 2014, **50**, 8507-8510.
12. M. J. Bojdys, M. E. Briggs, J. T. A. Jones, D. J. Adams, S. Y. Chong, M. Schmidtmann and A. I. Cooper, *J. Am. Chem. Soc.*, 2011, **133**, 16566-16571.
13. F. Grepioni and D. Savoia, *J. Org. Chem.*, 1997, **62**, 4180-4182.
14. Y. N. Belokon, J. Fuentes, M. North and J. W. Steed, *Tetrahedron*, 2004, **60**, 3191-3204.
15. T. Mitra, X. Wu, R. Clowes, J. T. A. Jones, K. E. Jelfs, D. J. Adams, A. Trewin, J. Bacsa, A. Steiner and A. I. Cooper, *Chem. Eur. J.*, 2011, **17**, 10235-10240.
16. T. Hasell, S. Y. Chong, K. E. Jelfs, D. J. Adams and A. I. Cooper, *J. Am. Chem. Soc.*, 2012, **134**, 588-598.
17. T. Hasell, J. L. Culshaw, S. Y. Chong, M. Schmidtmann, M. A. Little, K. E. Jelfs, E. O. Pyzer-Knapp, H. Shepherd, D. J. Adams, G. M. Day and A. I. Cooper, *J. Am. Chem. Soc.*, 2014, **136**, 1438-1448.
18. J. L. Culshaw, G. Cheng, M. Schmidtmann, T. Hasell, M. Liu, D. J. Adams and A. I. Cooper, *J. Am. Chem. Soc.*, 2013, **135**, 10007-10010.
19. S. I. Swamy, J. Bacsa, J. T. A. Jones, K. C. Stylianou, A. Steiner, L. K. Ritchie, T. Hasell, J. A. Gould, A. Laybourn, Y. Z. Khimyak, D. J. Adams, M. J. Rosseinsky and A. I. Cooper, *J. Am. Chem. Soc.*, 2010, **132**, 12773-12775.
20. M. Liu, M. A. Little, K. E. Jelfs, J. T. A. Jones, M. Schmidtmann, S. Y. Chong, T. Hasell and A. I. Cooper, *J. Am. Chem. Soc.*, 2014, **136**, 7583-7586.
21. D. Savoia, D. Balestri, S. Grilli and M. Monari, *Eur. J. Org. Chem.*, 2014, 1907-1914.
22. S. Grilli, G. Martelli, D. Savoia and C. Zazzetta, *Adv. Synth. Catal.*, 2002, **344**, 1068-1072.
23. E. J. Corey and A. Venkateswarlu, *J. Am. Chem. Soc.*, 1972, **94**, 6190-6191.
24. V. Suresh, J. J. P. Selvam, K. Rajesh, V. Shekhar, D. C. Babu and Y. Venkateswarlu, *Synthesis*, 2010, 1763-1765.
25. G. Melaugh, N. Giri, C. E. Davidson, S. L. James and M. G. Del Pópolo, *Phys. Chem. Chem. Phys.*, 2014, **16**, 9422-9431.
26. M. Mastalerz and I. M. Oppel, *Angew. Chem.*, 2012, **51**, 5252-5255.
27. B. M. Trost and M. U. Frederiksen, *Angew. Chem. Int. Ed.*, 2005, **44**, 308-310.
28. L. Thunberg and S. Allenmark, *J. Chromatogr. A*, 2004, **1026**, 65-76.
29. B. Kohl, F. Rominger and M. Mastalerz, *Org. Lett.*, 2014, **16**, 704-707.
30. D. Xu and R. Warmuth, *J. Am. Chem. Soc.*, 2008, **130**, 7520-7521.
31. P. Skowronek, B. Warzajtis, U. Rychlewska and J. Gawronski, *Chem. Commun.*, 2013, **49**, 2524-2526.

32. K. E. Jelfs, X. Wu, M. Schmidtmann, J. T. A. Jones, J. E. Warren, D. J. Adams and A. I. Cooper, *Angew. Chem.*, 2011, **50**, 10653-10656.
33. J. T. A. Jones, T. Hasell, X. Wu, J. Bacsa, K. E. Jelfs, M. Schmidtmann, S. Y. Chong, D. J. Adams, A. Trewin, F. Schiffman, F. Cora, B. Slater, A. Steiner, G. M. Day and A. I. Cooper, *Nature*, 2011, **474**, 367-371.
34. G. Zhang, O. Presly, F. White, I. M. Oppel and M. Mastalerz, *Angew. Chem. Int. Ed.*, 2014, **53**, 1516-1520.
35. J. D. Evans, C. J. Sumby and C. J. Doonan, *Chem. Lett.*, 2015, **44**, 582-588.
36. F. Orsini, G. Sello and G. Bestetti, *Tetrahedron: Asymmetry*, 2001, **12**, 2961-2969.
37. C. Boga, C. Fiorelli and D. Savoia, *Synthesis*, 2006, 285-292.
38. R. A. Smaldone, R. S. Forgan, H. Furukawa, J. J. Gassensmith, A. M. Z. Slawin, O. M. Yaghi and J. F. Stoddart, *Angew. Chem. Int. Ed.*, 2010, **49**, 8630-8634.
39. J. E. Mondloch, O. Karagiaridi, O. K. Farha and J. T. Hupp, *CrystEngComm*, 2013, **15**, 9258-9264.
40. S. Hanessian, R. Margarita, A. Hall, S. Johnstone, M. Tremblay and L. Parlanti, *J. Am. Chem. Soc.*, 2002, **124**, 13342-13343.
41. O. V. Dolomanov, L. J. Bourhis, R. J. Gildea, J. A. K. Howard and H. Puschmann, *J. Appl. Cryst.*, 2009, **42**, 339-341.

Chapter 5

Separation of Xenon from Krypton using Porous Organic Cages

5.1 Introduction to Xe/Kr Separation

Noble gases are industrially important molecules due to their distinctive properties such as lack of chemical reactivity and very low conductivity.[1] In particular, Xe and Kr, in their pure forms, are used in medical applications (e.g. imaging, anaesthesia) and commercial lighting. Xe and Kr occur naturally in the atmosphere (0.087 ppmv and 1.14 ppmv respectively) and can be generated as by-products in the cryogenic distillation of air to separate nitrogen and oxygen.[2] However, this process is energy-intensive, costly and the purity of the resulting gases may be insufficient for some applications.[3]

Cryogenic distillation has also been applied to the capture and separation of Xe and Kr from process off-gas streams during the reprocessing of UNF. The various disadvantages of this technique have led researchers to investigate alternative technologies. Recently, there has been an increasing focus on the use of microporous materials for the separation of Xe and Kr from air, and from each other, under ambient conditions *via* selective physical adsorption. Although more traditional activated carbon and zeolite materials were initially assessed,[4-6] MOFs have recently received significant attention. The ability to fine-tune their properties in a controllable manner makes them ideal candidates as selective adsorbents and they are the best-performing microporous materials tested for Xe/Kr separation to date.[7-10] Complementary experimental and simulation studies of both known and theoretical MOF structures have concluded that the ideal material for Xe/Kr separation should possess, amongst other properties, a high concentration of open metal sites on the pore surface, as well as narrow pores of uniform width which are large enough to accommodate a single Xe atom.[11]

POCs are discrete molecules which pack together in the solid state *via* non-covalent interactions to generate extended structures which, upon desolvation, can display high surface areas in the crystalline state.[12-14] Guest molecules are able to access the pre-fabricated and intrinsic cage void *via* windows within the cage structure. The cage packing mode, and hence the structure of the guest accessible pore network, is currently difficult to predict and requires computationally expensive calculations, although it has been shown that the crystallisation of POCs from certain solvents can afford porous materials with tailored and defined pore sizes.[15] Using computational

modelling studies based on their single crystal structures, it can be predicted whether POCs are suitable for a particular application. Despite the lack of open metal sites, the pore structures of certain POCs have deemed them as excellent candidates for Xe/Kr separation.

5.2 Xe/Kr Separation using Porous Organic Cages

The ability of **CC3** to separate organic molecules[16] and act as a host for guests such as halogens[17] has been previously reported. In its α-phase, these properties are a direct consequence of the dimensions of the 3-D diamondoid pore network which runs through the intrinsic cage voids. The effect of its pore size in relation to its capacity to adsorb certain gas molecules has also been investigated by MD simulations.

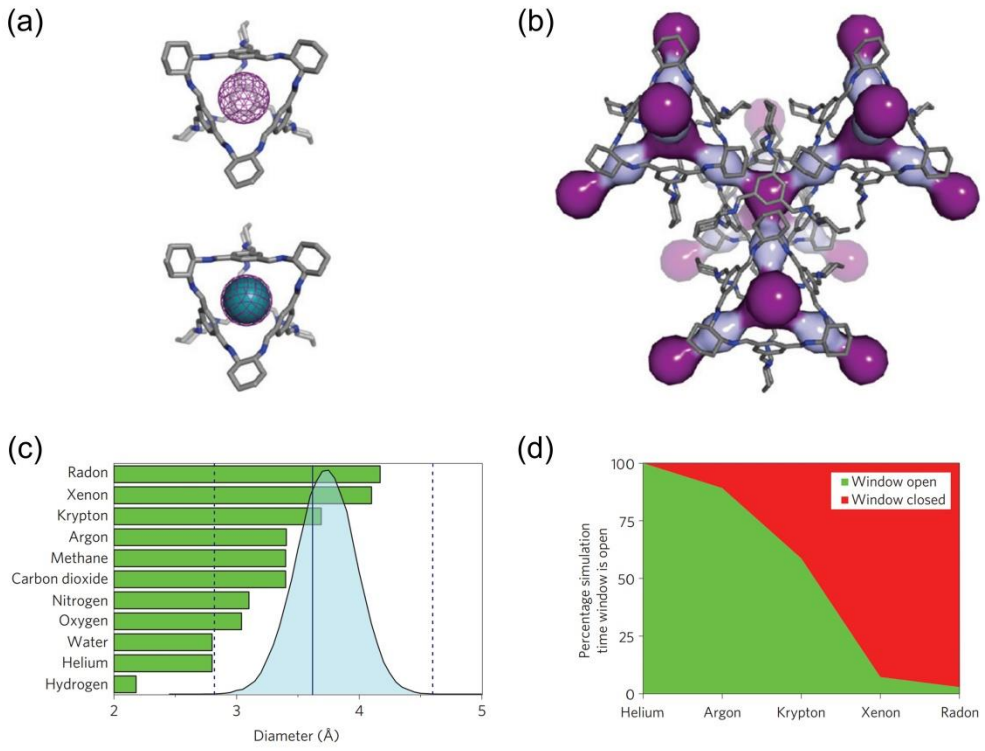

Figure 5.1 (a) The largest inclusion sphere inside the cage (dark purple mesh) is the correct size to accommodate a single Xe atom (cyan sphere). (b) Two pore cavities exist in the 3-D diamondoid pore structure of **CC3**: the intrinsic cage cavity (dark purple) and a window cavity between adjacent cage windows (light purple). (c) MD simulations (298 K, 1 bar) show a PLE (blue) that encompasses the minimum molecular dimensions of all noble gases. The straight vertical line corresponds to the PLD. (d) For Xe, the pore windows are "open" for a small fraction (7 %) of the simulated time period.[18]

Viewed as a static structure, it is not immediately apparent that **CC3** should exhibit any significant levels of porosity towards certain gases. The accessible surface area inside **CC3** can be described as having a bottleneck appearance, with the narrowest point in the pore channels lying between the cage and window cavities (Figure 5.1b). The dimensions of this, denoted as the PLD, was calculated by Holden *et al.* to have a value of 3.62 Å (Figure 5.1c).[19] Considering the kinetic diameter of N_2 is 3.64 Å, analysis of the static structure suggested that **CC3** should be formally non-porous to N_2. However, gas sorption studies of **CC3** have shown this not to be the case.[20] The individual cage molecules themselves are not static bodies and their structures possess a degree of flexibility. By allowing for the vibrational motion of the atoms in the cage molecules, MD simulations demonstrated that the size of the pore channel changes over time, ranging from a minimum of 3.0 Å to a maximum diameter of 4.5 Å (Figure 5.1c**)**. This was termed the PLE and showed that the size of the pore can expand above the "static" average level of 3.62 Å. In turn, the narrowest point in the 3-D pore structure was open to N_2 for a certain amount of the simulated time period, providing N_2 with the chance to opportunistically hop between cage cavities and afford **CC3** with its impressive adsorption properties.

In a following investigation, Holden *et al.* used MD simulations to investigate the diffusion of six gas molecules in **CC3** using a flexible host model.[21] The noble gases Kr and Xe, with diameters of 3.69 Å and 4.10 Å respectively, were included in this study. The dimensions of these rare gases are greater than that of the PLD, but smaller than the maximum value of the PLE (Figure 5.1c). It was calculated that the cage windows were open to Kr for 59 % of the simulated time period, whereas for Xe they were open for only 7 % (Figure 5.1d).[21] In practice, this means that both noble gases are able to diffuse between adjacent cage molecules, with Xe diffusing more slowly due to its larger size.

On closer inspection of its pore dimensions, the internal cavity of **CC3** has an inclusion sphere with a diameter of 4.40 Å, which is close to the diameter of Xe (Figure 5.1a). If you include the small time period within which the narrowest point in the pore channel is large enough to accommodate the diffusion of Xe, it can be argued that this satisfies the conclusions of Sikora *et al.*, who noted that the ideal pore structure for Xe/Kr separation needs to be uniform and just large enough to accommodate a single Xe atom.[22] Despite the lack of open metal sites, which have

been shown to promote the preferential adsorption of Xe over Kr, kinetically, it is possible that Xe may be separated from Kr based on a pore-confinement effect. By taking advantage of the larger size and lower diffusivity of Xe in relation to Kr, it is possible that they can be efficiently separated using **CC3**.

5.3 Xenon and Krypton Uptake in CC3

As a result of the simulation studies by Holden *et al.*, **CC3** was investigated as a candidate for Xe/Kr separation in collaboration with Dr Praveen Thallapally at the Pacific Northwest National Laboratory. Synthesised in accordance with the literature procedure,[20] the ability of a **CC3** powder sample to adsorb Xe and Kr was initially measured using a static gravimetric method.

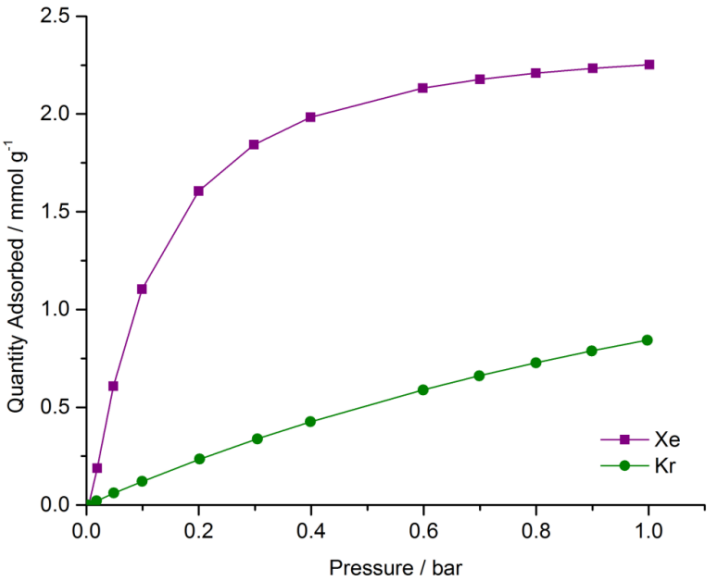

Figure 5.2 Xe and Kr adsorption isotherms for **CC3** at 298 K and 1 bar.

At 298 K and 1 bar, **CC3** was found to preferentially adsorb Xe (2.25 mmol g^{-1}, 30 wt %) over Kr (0.84 mmol g^{-1}, 7 wt %). The higher Xe uptake is due to stronger van der Waals interactions as a consequence of its higher polarisability. Whereas the Xe isotherm approaches saturation at 1 bar, the Kr isotherm does not, and this is due to its lack of adsorption capability. These values correlate with the volumetric Xe and Kr uptakes measured prior to this study (2.43 mmol g^{-1} and 0.93 mmol g^{-1} respectively). These results also validate the predictions of Holden *et al.* by demonstrating that the flexible nature of the cage molecules does indeed allow larger

guests such as Xe to diffuse through the pore structure and be adsorbed. Of course, this method only considers the thermodynamic equilibrium effect. For commercial applications, including the capture of Xe and Kr from process off-gas streams, kinetic effects also need to be accounted for. Not only are you dealing with the presence of other gases (N_2, O_2, CO_2, Ar) competing for adsorption sites, but the respective diffusion properties of these gases must also be considered. To account for this, dynamic breakthrough measurements were conducted.

5.4 Xe/Kr Breakthrough Measurements using CC3

Prior to performing dynamic breakthrough measurements, the powder sample was processed into 600 – 850 μm pellets to minimise pressure drop and potential contamination of the instrument during the measurements (Section 2.1.7). This process has been shown to leave the physical and chemical properties of MOFs unaffected in relation to the original powder sample.[23]

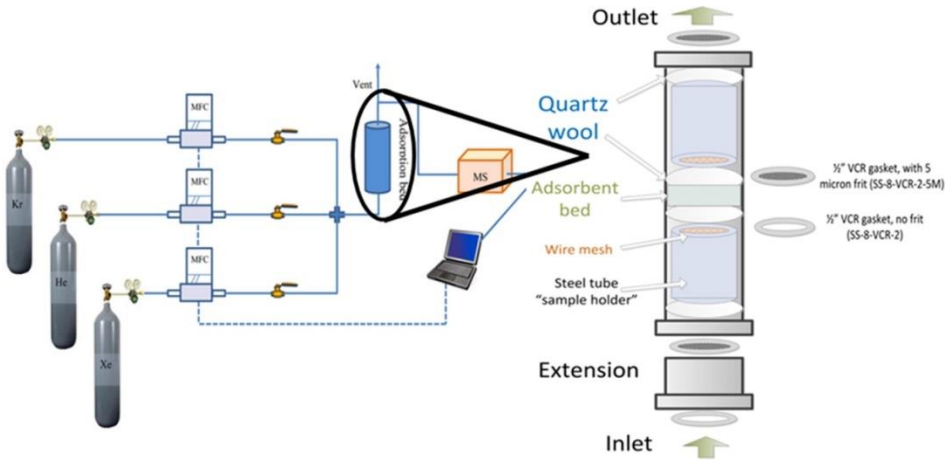

Figure 5.3 Apparatus for Xe/Kr breakthrough measurements.[24]

In reference to the apparatus illustrated in Figure 5.3, the gases are introduced through the bottom inlet of the adsorption bed, which consists of the cage pellets held between two layers of quartz wool and two sample holders.[25] The inlet gas stream is controlled using specialised computer software, while the composition of the outlet stream is analysed by mass spectrometry. To determine whether the **CC3** pellets were appropriate for breakthrough measurements, in terms of both retention time and the uptake in comparison to the static gravimetric method, pure Xe and Kr breakthrough curves were collected separately at 298 K and 1 bar (Figure 5.4).

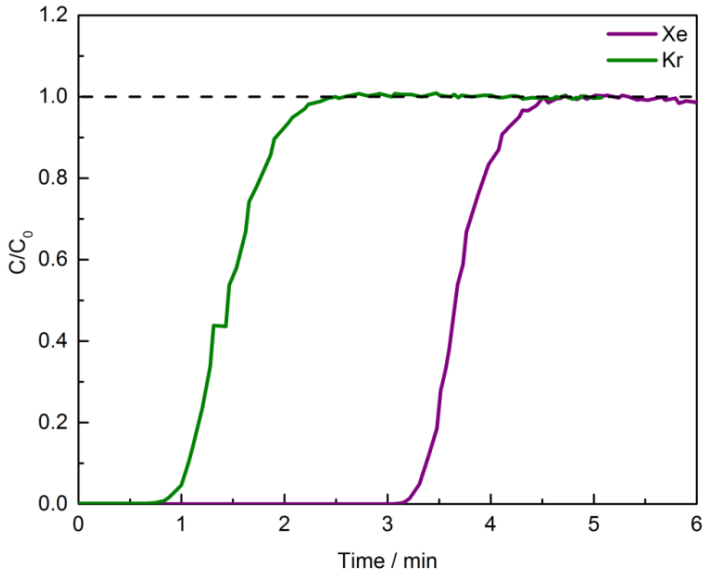

Figure 5.4 Pure Xe and Kr breakthrough curves for **CC3** at 298 K and 1 bar. The flow rate of Xe and Kr is 20 sccm.

It can be seen in Figure 5.4 that Xe is retained within the adsorption bed for a longer time than Kr. This not only confirms that **CC3** can adsorb more Xe than Kr, but that the diffusion rate of Xe is slower than Kr. The Xe and Kr uptakes using this method were calculated by integrating the areas above their respective breakthrough curves, as demonstrated in previous publications.[25] Based on the mass balance, the gas adsorption properties can be determined as follows:

$$q = \frac{C_0 V t_s}{22.4 W} \qquad (5.1)$$

$$t_s = \int_0^t \left(1 - \frac{F}{F_0}\right) dt \qquad (5.2)$$

where t_s is the stoichiometric time (min), C_0 is the feed gas concentration, F_0 and F are the inlet and outlet gas molar flow rates respectively, q is the equilibrium adsorption capacity of gas (mmol g^{-1}), t is the adsorption time (min) which is from time zero to time when equilibrium is reached, V is the volumetric feed flow rate (cm^3 min^{-1}) at standard temperature and pressure (273 K and 1 atm) and W is the weight of the activated adsorbent (g).[25]

Table 5.1 Pure Xe and Kr breakthrough capacities for different porous materials at 298 K and 1 bar.[24]

Material	Xe Uptake / mmol g^{-1}	Kr Uptake / mmol g^{-1}
Ni/DOBDC	3.83	1.69
HKUST-1	3.18	1.92
Activated Carbon	3.72	2.62
CC3	2.56	1.06

From the pure breakthrough curves, the Xe and Kr uptakes of **CC3** were calculated to be 2.56 mmol g^{-1} and 1.06 mmol g^{-1} respectively. These dynamic capacities are in fairly good agreement with the values determined from the pure gas adsorption isotherms of the powder sample. The Xe uptake in **CC3** is lower than other porous materials studied under identical conditions (Table 5.1). This is a consequence of the lower number of available adsorption sites in **CC3**, as well as the absence of open metal sites which are prominent in the MOFs listed above. The Kr uptake in **CC3** is also much lower in comparison and this can be attributed to a lack of these key properties. This is beneficial, as the ideal Xe/Kr selectivity is higher for **CC3** (2.42) than the other listed materials. The high selectivity is due to **CC3** having the optimal pore dimensions for the adsorption of Xe, while there are no smaller cavities which may preferentially adsorb Kr. This results in a lower Kr uptake and therefore a higher Xe/Kr selectivity.

The next stage was to perform breakthrough measurements of Xe and Kr mixtures of different compositions (Xe/Kr = 80:20, 50:50 and 20:80) to analyse whether separation could be achieved with both gases present. It can be seen in Figures 5.5a-c that effective separation of Xe from Kr was achieved at all compositions. The breakthrough result for Xe/Kr (20:80), an industrially-relevant composition, mirrors that of the pure Xe and Kr breakthrough curves, with Xe breaking through after Kr (Figure 5.5c). This is confirmed by the characteristic roll-up in the Kr breakthrough curve, which is caused by the displacement of Kr by Xe.[26] This phenomenon was observed for each binary mixture. Once the Kr breaks through, its outlet concentration exceeds its inlet concentration, as more Kr molecules are displaced by the Xe molecules which are slowly diffusing through the pore structure and preferentially occupying the adsorption sites instead of Kr. In addition, as the Xe

concentration in the gas mixture decreases, the time it takes to break through the adsorption bed and reach equilibrium increases. With a lower concentration of Xe in the gas mixture, there is less competition to occupy adsorption sites and initiate displacement of other Xe atoms, resulting in Xe diffusing through the adsorption bed more slowly and becoming concentrated within the pores. Diversely, the Kr moves through faster, as its greater concentration, combined with a higher diffusivity and lack of adsorption capability, allows it to break through much more rapidly.

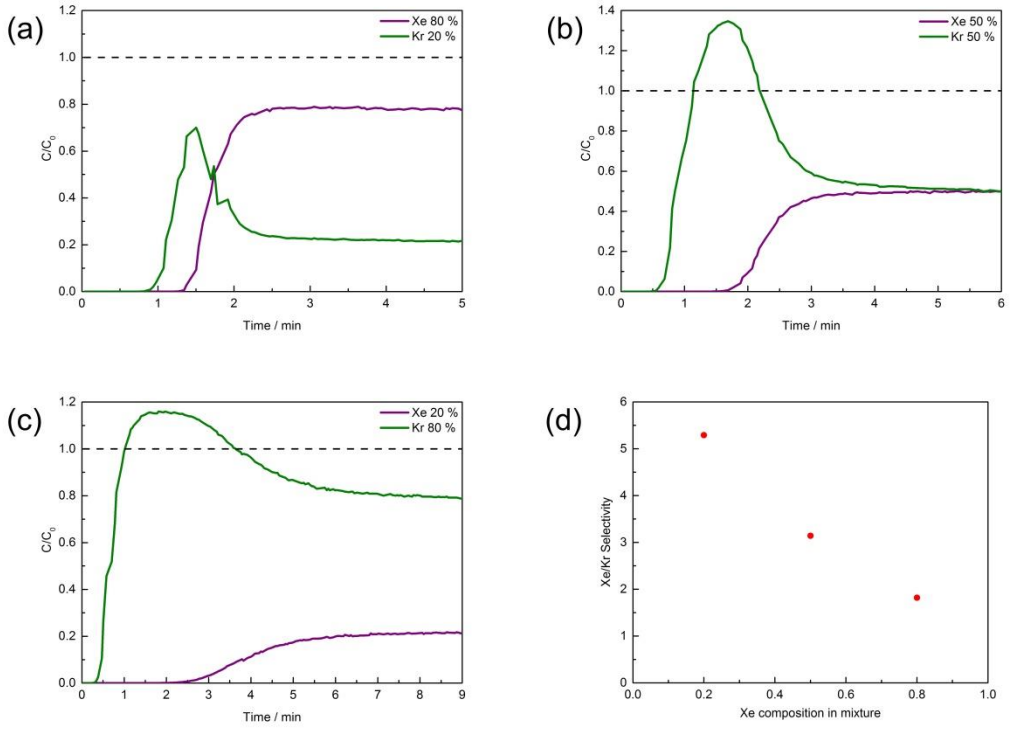

Figure 5.5 (a-c) Xe/Kr breakthrough curves for **CC3** under different Xe and Kr compositions: (a) Xe/Kr (80:20); (b) Xe/Kr (50:50), and; (c) Xe/Kr (20:80). The flow rate of Xe and Kr together is 40 sccm and experiments were conducted at 298 K and 1 bar. (d) Xe/Kr selectivity comparison for **CC3** under different Xe and Kr compositions.

From these breakthrough curves, the respective dynamic capacities of Xe and Kr, determined using Equations 5.1 and 5.2, can be utilised to calculate the Xe/Kr selectivity using the standard definition:

$$S_{AB} = \frac{x_A / y_A}{x_B / y_B} \qquad (5.3)$$

where x_A and x_B are the mole fractions of gases A and B in the adsorbed phase and y_A and y_B are the mole fractions of gases A and B in the bulk phase.[25]

Equation 5.3 represents the overall selectivity, with both thermodynamic and kinetic selectivities taken into account. This is characteristic of breakthrough measurements. These selectivities follow opposite trends for Xe and Kr, with Xe possessing a higher polarisability but a lower diffusivity compared to Kr. Therefore, not only is the adsorption performance considered, but also the kinetic behaviour of the gas molecules within the material itself. This is a more accurate measure of selectivity compared to some simulation studies, which calculate the selectivity of mixture adsorption from single component isotherms at a given pressure.[27]

Table 5.2 Xe and Kr uptakes and selectivities for **CC3** at 298 K and 1 bar under different Xe and Kr compositions.

Xe/Kr Feed Ratio	Xe Uptake / mmol g^{-1}	Kr Uptake / mmol g^{-1}	Xe/Kr Selectivity
80:20	1.93	0.31	1.67
50:50	1.67	0.54	3.08
20:80	1.24	0.86	5.29

It can be seen in Table 5.2 that as the Xe composition in the mixture decreases, its uptake also falls. This is due to its lower concentration. Of greater interest, the Xe/Kr selectivity is observed to increase. For example, the Xe/Kr (20:80) selectivity for **CC3** (5.29) exceeds the measured selectivity of Ni/DOBDC (4)[24] but is lower than that of MOF-505 (9-10).[8] The improvement in selectivity is due to the lower concentration of Xe molecules preferentially occupying the cage cavities instead of Kr. Over time, the adsorption bed becomes saturated with Xe, until it finally breaks through after around two minutes (Figure 5.5c). Once equilibrium is reached, the Xe uptake in relation to its initial concentration far exceeds that of Kr and therefore results in a high selectivity. At this concentration, the effect of the pore structure becomes increasingly significant. Despite the presence of open metal sites, which preferentially adsorb Xe, the diameter of the hexagonal pores in Ni/DOBDC (11 Å) is much larger than the pore dimensions of **CC3** and MOF-505. This means that the diffusion of Xe through the pore channels in Ni/DOBDC is not hindered in the same way as it is in **CC3**, where the Xe atom needs to opportunistically hop between cage cavities in the small time period within which the cage windows are wide enough to facilitate diffusion. This validates the conclusion of Sikora *et al.* that pores which are

just large enough to accommodate a single Xe atom are required for effective separation.[22] The superior selectivity observed for MOF-505 can therefore be ascribed to the presence of open metal sites in conjunction with its narrow pore size.

Under these conditions, the kinetic effect predominates over the thermodynamic effect. Although the Xe uptake from the pure breakthrough curves was lower in comparison to the aforementioned MOFs, the higher Xe/Kr selectivity observed for **CC3** means that this porous material may be an ideal candidate for the separation of low concentrations of Xe and Kr from process off-gas streams during the reprocessing of UNF.

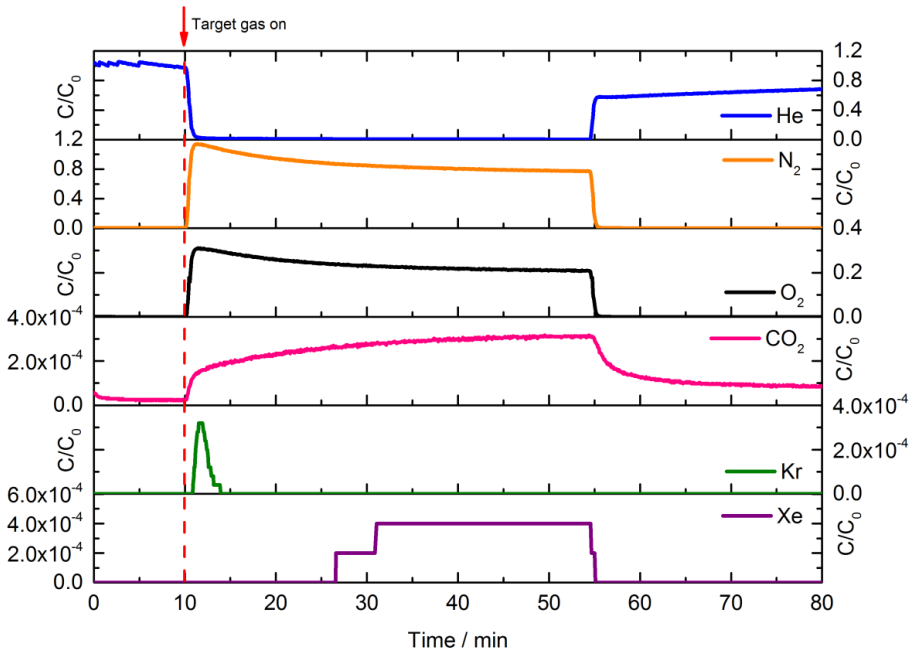

Figure 5.6 Xe (400 ppm) and Kr (40 ppm) in simulated air breakthrough curves for **CC3** at 298 K and 1 bar. The He flow rate is 40 sccm and the flow rate of Xe and Kr together in air is 40 sccm.

To imitate this separation, breakthrough measurements for low concentrations of Xe (400 ppm) and Kr (40 ppm) in simulated air (N_2, 78 %; O_2, 21 %; Ar, 0.9 %; CO_2, 0.03 %; etc.) were performed, mirroring the conditions that would be encountered in the reprocessing of UNF.[24] According to the breakthrough curves (Figure 5.6), N_2 and O_2 break through the adsorption bed immediately, closely followed by CO_2 and Kr. Remarkably, Xe was not detected until over fifteen minutes after the other components, despite using a flow rate of 40 sccm, which is twice the rate used for Ni/DOBDC, the best performing material to date.[24] Under these conditions, the

overall Xe uptake for **CC3** (11 mmol kg^{-1}) is greater than that of Ni/DOBDC (4.8 mmol kg^{-1}). In addition, the calculated Xe/Kr selectivity for **CC3** (20.4) is also higher (Table 5.3). Selectivity and capacity are often seen as a trade-off, but **CC3** displays major improvements with respect to both.

Table 5.3 Comparison of the Xe uptake and Xe/Kr selectivity between Ni/DOBDC and **CC3** from Xe (400 ppm) and Kr (40 ppm) in simulated air breakthrough curves.

Material	Xe Uptake / mmol kg^{-1}	Xe/Kr Selectivity
Ni/DOBDC[24]	4.8	7.3
CC3	11	20.4

This improvement in separation performance was rationalised to be a consequence of the near-perfect fit between the cavities in **CC3** and the Xe guest.[18] Under the breakthrough conditions, Xe slowly diffuses between the cage cavities, while the smaller Kr continues to flow rapidly through the pore channels as a result of its smaller diameter and the lack of available adsorption sites. Xe is not easily displaced from the pore cavities by the other components of air and becomes concentrated within **CC3**, with the selectivity increasing as a result. On the other hand, the large pores in Ni/DOBDC enable Xe to be more easily displaced by the other components of air and lower the overall Xe uptake. Here, a pore-confinement effect has been shown to dominate and proves that high surface areas and open metal sites are not prerequisites for superior performance.[9]

5.5 Xenon and Krypton Uptake in CC1*β*

As a comparison, Xe and Kr uptakes were also measured for **CC1***β*. **CC1** was first reported by Tozawa *et al.* and is synthesised *via* the [4+6] cycloimination reaction of TFB with EDA.[28] Upon crystallisation from an ethyl acetate solution, the isolated cage was found to pack in window-to-arene stacks with disconnected lattice voids, and was therefore formally non-porous to N_2. However, by exposing **CC1** to DCM vapour, it could be transformed into a new polymorph, **CC1***β*, which possessed an interconnected channel structure (Figure 5.7).[29]

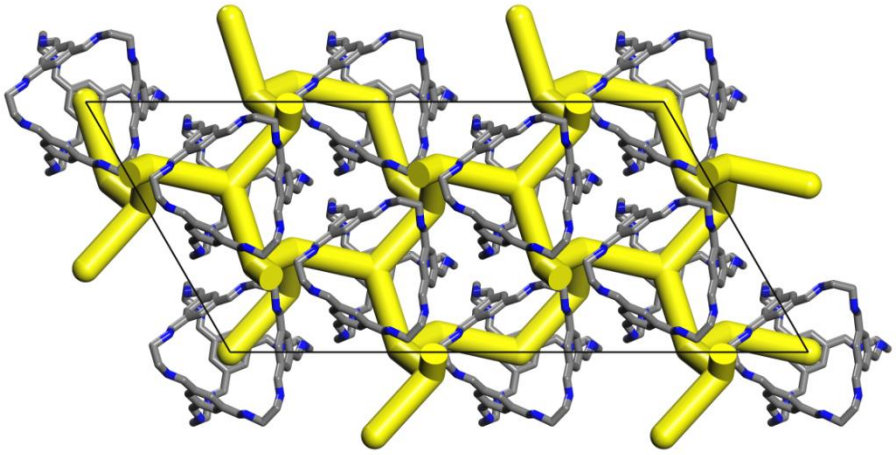

Figure 5.7 Representation of the packing arrangement of **CC1***β*, with interconnected channels shown in yellow.

Although formally non-porous to N_2, **CC1***β* adsorbs a significant quantity of H_2 (5.59 mmol g^{-1}, 1.18 wt %) at 77 K and 1 bar.[29] Its relevance to Xe/Kr separation was confirmed by running volumetric adsorption isotherms for each gas. At 298 K and 1 bar, **CC1***β* was found to adsorb Xe (2.09 mmol g^{-1}) in preference to Kr (0.91 mmol g^{-1}). These values are fairly similar to those of **CC3** and show that **CC1***β* may also show promise in Xe/Kr separation, although in practice, **CC3** is significantly more stable than **CC1***β*.

Synthesised in accordance with the literature procedure,[30] the Xe and Kr uptakes for a powder sample of **CC1***β* were measured, as for **CC3**, using a static gravimetric method. At 298 K and 1 bar, **CC1***β* was found to adsorb Xe (2.31 mmol g^{-1}, 30 wt %) and Kr (0.82 mmol g^{-1}, 7 wt %) with near identical uptakes to **CC3**. Again, as expected, the Xe capacity was higher than that of Kr. However, unlike **CC3**, the Xe uptake at 1 bar had not reached saturation (Figure 5.8). Hence, at 1 bar, Xe adsorption has not reached thermodynamic equilibrium and accessed all the potential adsorption sites. This may be due to the difficulty of the large Xe atoms in traversing the interconnected channels of **CC1***β*, which does not possess the 3-D pore structure of **CC3**. As MD simulations have not yet been run to study this porous material, it is difficult to reliably rationalise the behaviour observed here.

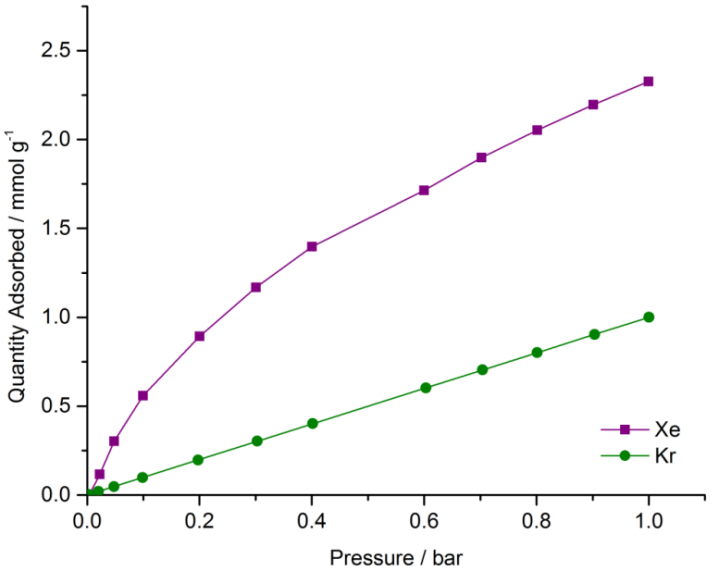

Figure 5.8 Xe and Kr adsorption isotherms for **CC1*β*** at 298 K and 1 bar.

5.6 Xe/Kr Breakthrough Measurements using CC1*β*

Performing dynamic breakthrough measurements for **CC1*β*** pellets with pure Xe and Kr gas streams demonstrated that it took longer for Xe to break through the adsorption bed compared to Kr, as would be expected (Figure 5.9a). Xe was retained for around one minute longer, which was shorter than that observed for **CC3** (over two minutes). The Xe uptake (1.85 mmol g^{-1}) was also lower than the uptake measured for the powder sample using the static gravimetric method (2.31 mmol g^{-1}), while the Kr uptake calculated from the breakthrough curve was actually higher in comparison (1.37 mmol g^{-1} *vs.* 0.82 mmol g^{-1}). These values indicate that a structural change may have occurred during the pelletisation process. Running Xe/Kr mixtures of different compositions (Xe/Kr = 80:20, 50:50 and 20:80) showed that the separation of Xe from Kr was less efficient than for **CC3**, with Xe breaking through quite soon after Kr (Figures 5.9b-d). It is clear that Xe diffuses through the adsorption bed much more readily than in **CC3**. The small roll-up in the Kr curve indicates that the outlet Kr concentration only briefly exceeds the inlet concentration due to less Kr being displaced. This also implies that under the breakthrough conditions, Xe struggles to find appropriate adsorption sites, resulting in more Xe atoms simply flowing straight through the adsorption bed without interaction. This

would explain the lower Xe uptake and also complements the lack of saturation observed in the pure static adsorption isotherm (Figure 5.8).

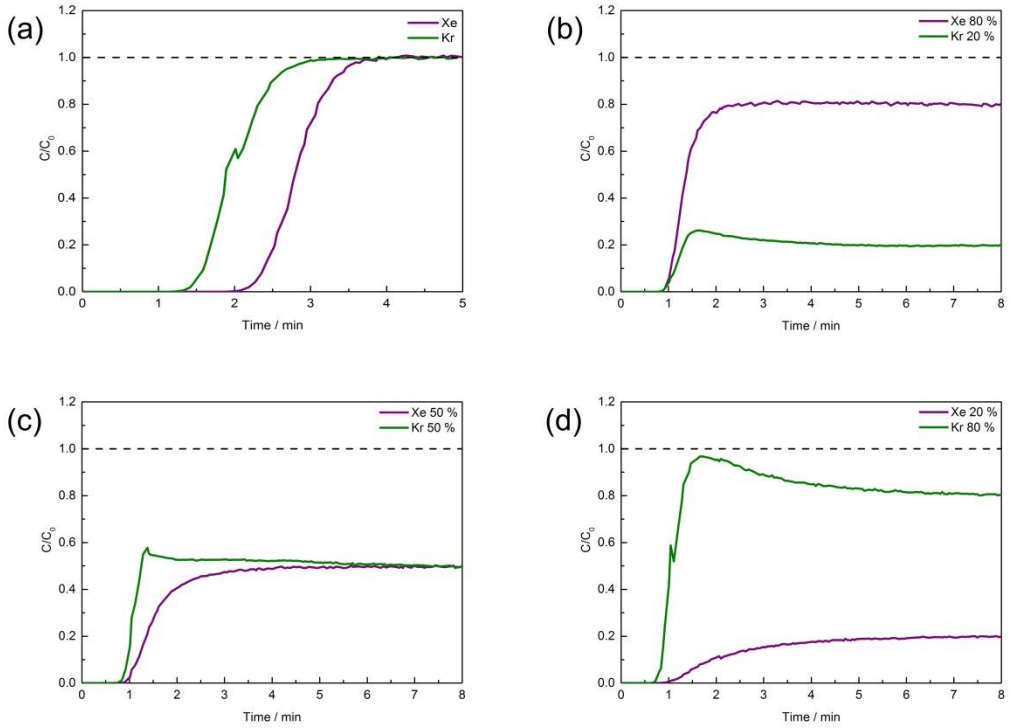

Figure 5.9 (a) Pure Xe and Kr breakthrough curves for **CC1***β* at 298 K and 1 bar. The flow rate of Xe and Kr is 20 sccm. (b-d) Xe/Kr breakthrough curves for **CC1***β* under different Xe and Kr compositions: (b) Xe/Kr (80:20); (c) Xe/Kr (50:50), and; (d) Xe/Kr (20:80). The flow rate of Xe and Kr together is 40 sccm and experiments were conducted at 298 K and 1 bar.

Calculation of the Xe/Kr selectivity revealed that **CC1***β* is not as selective as **CC3** for Xe over Kr at these concentrations. This can be understood by simply analysing the respective gas uptakes (Table 5.4). For **CC3**, the Kr uptakes were always lower than Xe, regardless of the composition used. However, for **CC1***β* this is not the case, with the Kr uptake exceeding that of Xe when using a Xe/Kr (20:80) mixture. This behaviour is understandable based on the Kr uptake calculated from the pure breakthrough curves, which was much higher than expected. A higher Kr uptake resulted in a lower overall Xe/Kr selectivity and this is reflected in the Xe/Kr (20:80) selectivity value for **CC1***β* (2.35), which is nearly half that calculated at the same composition for **CC3** (5.29).

Table 5.4 Xe and Kr uptakes and selectivities for **CC1***β* at 298 K and 1 bar under different Xe and Kr compositions.

Xe/Kr Feed Ratio	Xe Uptake / mmol g^{-1}	Kr Uptake / mmol g^{-1}	Xe/Kr Selectivity
80:20	1.39	0.31	1.17
50:50	1.14	0.73	1.61
20:80	0.71	1.09	2.35

As for **CC3**, breakthrough measurements for low concentrations of Xe (400 ppm) and Kr (40 ppm) in simulated air were performed for **CC1***β*. According to the breakthrough curves (Figure 5.10), N_2 and O_2 break through the adsorption bed immediately, followed by CO_2 and Kr. These were the same observations made for **CC3**. However, rather unexpectedly, Xe was not detected until around seven minutes after the other components and took much longer than in **CC3** to reach equilibrium under the breakthrough conditions. This is peculiar, as based on the binary mixtures tested, the effectiveness of this separation was not expected, especially in comparison to the observations made for **CC3**. Calculation of the Xe uptake and Xe/Kr selectivity showed that while the adsorption capacity of **CC1***β* (8.4 mmol kg^{-1}) was less than **CC3** (11 mmol kg^{-1}), the Xe/Kr selectivity was superior (28.5 *vs.* 20.4). A lower Kr uptake for **CC1***β* compared to **CC3** (0.03 *vs.* 0.05 mmol kg^{-1}) makes a contribution to this increase in selectivity, which is the highest observed from experimental measurements to date.

Under these conditions, it is apparent for both **CC1***β* and **CC3** that Kr is able to diffuse quickly through the adsorption bed, with the other components of air ensuring a low adsorption capacity. In addition, due to a combination of its low concentration and diffusivity, Xe finds it difficult to pass through the adsorption bed, regardless of the extent of interconnection and the pore dimensions between the internal cavities of the cage molecules. For **CC1***β*, it would be extremely beneficial to use MD simulations to probe the influence of the other air components on the Xe and Kr uptake and selectivity, as well as the effect of the pore structure of **CC1***β*, to rationalise this behaviour.

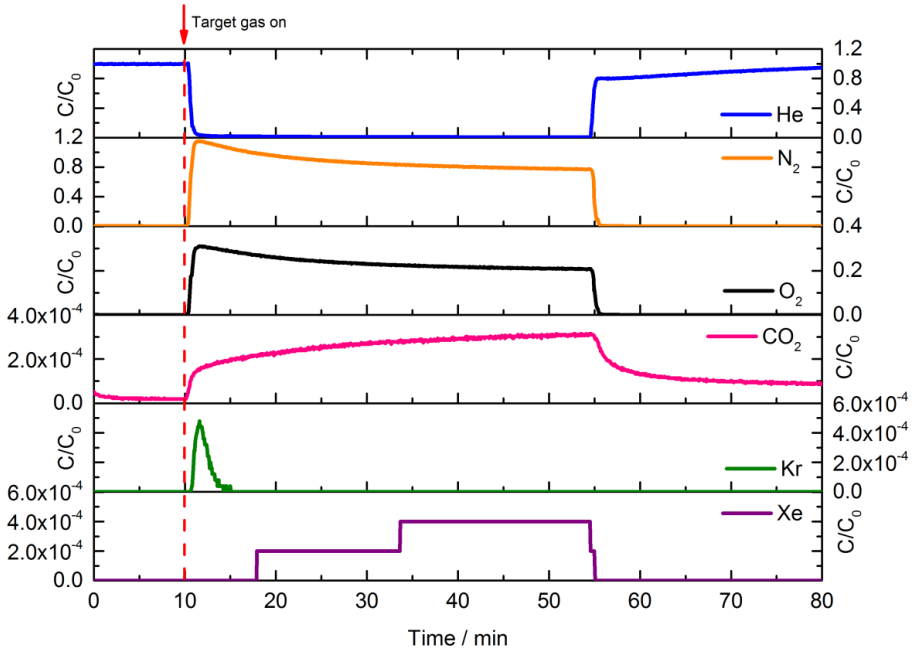

Figure 5.10 Xe (400 ppm) and Kr (40 ppm) in simulated air breakthrough curves for **CC1***β* at 298 K and 1 bar. The He flow rate is 40 sccm and the flow rate of Xe and Kr together in air is 40 sccm.

5.7 Conclusions and Outlook

In this chapter, it has been demonstrated through the use of dynamic breakthrough measurements that two POCs, **CC1***β* and **CC3**, are suitable candidates for the capture and separation of Xe and Kr under conditions mimicking those experienced in the reprocessing of UNF. In the case of **CC3**, the effective separation of these noble gases at low concentrations was achieved as a consequence of the dimensions of its 3-D diamondoid pore network, which were a "perfect fit" for the Xe guest.[18] This resulted in the diffusion of the larger, more polarisable Xe being more hindered in comparison to Kr; leading to both a higher Xe uptake and Xe/Kr selectivity in comparison to the previous-best material Ni/DOBDC. These findings also validate complementary MD simulations which initially investigated the flexibility of the cage structures themselves and its impact on the pore size, as well as studying the diffusion properties of these gases through the pore channels. Despite performing poorly in the separation of Xe from Kr using binary gas mixtures, the Xe/Kr selectivity for **CC1***β* under the same UNF reprocessing conditions actually surpassed **CC3**. The selectivity of 28.5 is the highest recorded to date and shows that at low concentrations, Xe finds it difficult to diffuse through the interconnected pore channels of these POC molecules.

These results demonstrate that neither high surface areas, nor the presence of open metal sites, are key prerequisites for this separation application, with the pore dimensions of the porous material found to be the most important factor. This justifies the conclusions of many simulation studies, where materials containing narrow pores of uniform width, which are large enough to accommodate a single Xe atom, have been shown to be the most applicable for Xe/Kr separation. The synthesis of new materials, or the study of previously-reported ones, needs to keep this feature in mind. However, the design, preparation and isolation of new porous materials with these desired structures and properties are not trivial. Therefore, the use of simulation studies to guide towards and identify promising candidates will prove crucial. With respect to POCs, incorporating silver nanoparticles whilst retaining surface area and appropriate pore dimensions is an attractive option, as they have been shown to enhance Xe adsorption.[31] Furthermore, investigating the utility of POCs in a two-column breakthrough approach[32] may also reinforce their applicability to the commercial separation of these noble gases.

5.8 References

1. Y. Gurdal and S. Keskin, *J. Phys. Chem. C*, 2013, **117**, 5229-5241.
2. F. G. Kerry, *Industrial Gas Handbook: Gas Separation and Purification*, CRC Press: Boca Raton, Florida, 2007.
3. J. Izumi, *In Handbook of Zeolite Science and Technology*, S. M. Auerbach, K. A. Carrado, P. K. Dutta, Eds.; CRC Press: New York, 2003.
4. K. Munakata, T. Fukumatsu, S. Yamatsuki, K. Tanaka and M. Nishikawa, *Journal of Nuclear Science and Technology*, 1999, **36**, 818-829.
5. C. J. Jameson, A. K. Jameson and H.-M. Lim, *J. Chem. Phys.*, 1997, **107**, 4364.
6. S. M. Kuznicki, A. Ansón, A. Koenig, T. M. Kuznicki, T. Haastrup, E. M. Eyring and D. Hunter, *J. Phys. Chem. C*, 2007, **111**, 1560-1562.
7. P. K. Thallapally, J. W. Grate and R. K. Motkuri, *Chem. Commun.*, 2012, **48**, 347-349.
8. Y.-S. Bae, B. G. Hauser, Y. J. Colón, J. T. Hupp, O. K. Farha and R. Q. Snurr, *Microporous and Mesoporous Materials*, 2013, **169**, 176-179.
9. H. Wang, K. Yao, Z. Zhang, J. Jagiello, Q. Gong, Y. Han and J. Li, *Chem. Sci.*, 2014, **5**, 620-624.
10. U. Mueller, M. Schubert, F. Teich, H. Puetter, K. Schierle-Arndt and J. Pastré, *J. Mater. Chem.*, 2006, **16**, 626.
11. D. Banerjee, A. J. Cairns, J. Liu, R. K. Motkuri, S. K. Nune, C. A. Fernandez, R. Krishna, D. M. Strachan and P. K. Thallapally, *Acc. Chem. Res.*, 2015, **48**, 211-219.
12. J. T. A. Jones, T. Hasell, X. Wu, J. Bacsa, K. E. Jelfs, M. Schmidtmann, S. Y. Chong, D. J. Adams, A. Trewin, F. Schiffman, F. Cora, B. Slater, A. Steiner, G. M. Day and A. I. Cooper, *Nature*, 2011, **474**, 367-371.

13. G. Zhang, O. Presly, F. White, I. M. Oppel and M. Mastalerz, *Angew. Chem. Int. Ed.*, 2014, **53**, 1516-1520.
14. M. Mastalerz, M. W. Schneider, I. M. Oppel and O. Presly, *Angew. Chem.*, 2011, **50**, 1046-1051.
15. T. Hasell, J. L. Culshaw, S. Y. Chong, M. Schmidtmann, M. A. Little, K. E. Jelfs, E. O. Pyzer-Knapp, H. Shepherd, D. J. Adams, G. M. Day and A. I. Cooper, *J. Am. Chem. Soc.*, 2014, **136**, 1438-1448.
16. T. Mitra, K. E. Jelfs, M. Schmidtmann, A. Ahmed, S. Y. Chong, D. J. Adams and A. I. Cooper, *Nat. Chem.*, 2013, **5**, 276-281.
17. T. Hasell, M. Schmidtmann and A. I. Cooper, *J. Am. Chem. Soc.*, 2011, **133**, 14920-14923.
18. L. Chen, P. S. Reiss, S. Y. Chong, D. Holden, K. E. Jelfs, T. Hasell, M. A. Little, A. Kewley, M. E. Briggs, A. Stephenson, K. M. Thomas, J. A. Armstrong, J. Bell, J. Busto, R. Noel, J. Liu, D. M. Strachan, P. K. Thallapally and A. I. Cooper, *Nat. Mater.*, 2014, **13**, 954-960.
19. D. Holden, K. E. Jelfs, A. I. Cooper, A. Trewin and D. J. Willock, *J. Phys. Chem. C*, 2012, **116**, 16639-16651.
20. T. Hasell, S. Y. Chong, K. E. Jelfs, D. J. Adams and A. I. Cooper, *J. Am. Chem. Soc.*, 2012, **134**, 588-598.
21. D. Holden, K. E. Jelfs, A. Trewin, D. J. Willock, M. Haranczyk and A. I. Cooper, *J. Phys. Chem. C*, 2014, **118**, 12734-12743.
22. B. J. Sikora, C. E. Wilmer, M. L. Greenfield and R. Q. Snurr, *Chem. Sci.*, 2012, **3**, 2217.
23. G. W. Peterson, J. B. DeCoste, T. G. Glover, Y. Huang, H. Jasuja and K. S. Walton, *Microporous and Mesoporous Materials*, 2013, **179**, 48-53.
24. J. Liu, P. K. Thallapally and D. Strachan, *Langmuir*, 2012, **28**, 11584-11589.
25. J. Liu, J. Tian, P. K. Thallapally and B. P. McGrail, *J. Phys. Chem. C*, 2012, **116**, 9575-9581.
26. S. W. Lee, S. K. Kam and M. G. Lee, *Journal of Industrial and Engineering Chemistry*, 2007, **13**, 911-916.
27. P. Ryan, O. K. Farha, L. J. Broadbelt and R. Q. Snurr, *AIChE J.*, 2011, **57**, 1759-1766.
28. T. Tozawa, J. T. A. Jones, S. I. Swamy, S. Jiang, D. J. Adams, S. Shakespeare, R. Clowes, D. Bradshaw, T. Hasell, S. Y. Chong, C. Tang, S. Thompson, J. Parker, A. Trewin, J. Bacsa, A. M. Slawin, A. Steiner and A. I. Cooper, *Nat. Mater.*, 2009, **8**, 973-978.
29. J. T. A. Jones, D. Holden, T. Mitra, T. Hasell, D. J. Adams, K. E. Jelfs, A. Trewin, D. J. Willock, G. M. Day, J. Bacsa, A. Steiner and A. I. Cooper, *Angew. Chem. Int. Ed.*, 2011, **50**, 749-753.
30. D. P. Lydon, N. L. Campbell, D. J. Adams and A. I. Cooper, *Synthetic Communications*, 2011, **41**, 2146-2151.
31. J. Liu, D. M. Strachan and P. K. Thallapally, *Chem. Commun.*, 2014, **50**, 466-468.
32. J. Liu, C. A. Fernandez, P. F. Martin, P. K. Thallapally and D. M. Strachan, *Ind. Eng. Chem. Res.*, 2014, **53**, 12893-12899.

Chapter 6

Conclusions and Future Outlook

6.1 Conclusions

The work presented in this thesis has primarily focussed on the synthetic modification of trialdehyde and diamine precursors towards the preparation of novel POCs, with an emphasis on tuning their gas sorption and separation properties.

CC14 was isolated after purification of a cage product mixture generated upon scrambling the cage precursors TFB, Me_3TFB and *R,R*-CHDA. Packing in a window-to-window and isoreticular fashion to its parent cage **CC3**, this asymmetric cage possessed a constricted interior cavity and PLE as a result of the incorporated methyl groups occupying accessible space within the pore structure. Although this resulted in lower gas uptakes, kinetic measurements demonstrated the ability of **CC14** to hinder the diffusion of Xe to a greater extent than that observed in **CC3**, making it a potential candidate for the separation of Xe from Kr gas during the reprocessing of UNF.

Enantiomerically-pure derivatives of CHDA were also prepared and successfully reacted with TFB in the preparation of new POC molecules. **CC16** was isolated as a phase-pure [4+6] cage, with the introduction of twelve peripheral methyl groups frustrating the molecular packing, generating additional extrinsic porosity and improving the gas sorption properties in comparison to **CC3**, including an apparent BET surface area of 1023 $m^2\ g^{-1}$. Alternatively, the introduction of twelve peripheral hydroxyl groups made cage formation difficult, with the poor solubility of the resulting cage **CC17** making its preparation, purification and crystallisation a challenge. Adopting a protection-deprotection strategy *via* the TBDMS-functionalised cage **CC18**, **CC17** could be isolated, although the gas sorption properties of this cage in the amorphous state did not exhibit any selectivity towards a particular gas. Utilising a commercially-sourced diamine which possessed bulky ethanoanthracene functionality, **CC19** was successfully synthesised and characterised. Isolated as an [8+12] cage, it is the largest imine bond-based cage prepared to date that is derived from the TFB precursor. However, the inherent flexibility of the bonds resulted in structural collapse upon desolvation.

In a separate investigation, **CC1***β* and **CC3** were demonstrated to be suitable candidates for the capture and separation of Xe and Kr under conditions mimicking those experienced in the reprocessing of UNF, with the measured Xe uptake and

Xe/Kr selectivity for both cages outperforming the previous-best porous material. In the case of **CC3**, the unprecedented performance was a direct consequence of the dimensions of its interconnected 3-D diamondoid pore network in relation to the Xe guest, with the findings validating complementary MD simulations.

6.2 Future Outlook

Despite the field of POCs still being relatively young, developments have been rapid, with cages of varying composition, stoichiometry, size and porosity being prepared in the intervening years. With respect to the cages prepared and presented in this thesis, employing derivatives of traditional precursors has been shown to successfully alter the properties in comparison to their parent cage. Although more sterically-demanding TFB derivatives could not be incorporated into the cage structure, synthetically modifying the diamine precursor was demonstrated to be an effective derivatisation strategy. Introducing other functional groups[1-3] onto cyclised diamine precursors will help build on the results presented herein and may lead to materials with superior properties. In the case of **CC17**, a more detailed investigation would be beneficial in finding a suitable route to its isolation, whether that be through elucidating conditions using the original diol diamine, or finding a protection-deprotection strategy that takes advantage of improved stabilities inferred upon post-synthetic "tying".[4] **CC17** is interesting due to the peripheral hydroxyl functionalities, which could possibly enable the cage to be reacted with metal salts in the preparation of cage-MOF materials,[5] allow chemical attachment to a surface in the preparation of chiral chromatography columns[6] or permit other PSM strategies to tune the gas sorption properties.

Future imine bond-based cages may benefit from a move away from the traditional trialdehyde-diamine approach, with the majority of precursors now being assessed. For example, the use of aldehydes based on the structures of certain extended tetratopic MOF linkers may lead to cages of alternate shapes and packing arrangements. Other approaches could involve the construction of robust architectures from carbon-carbon bonds, following the example of Avellaneda *et al.*[7] or employing alkyne metathesis, which would allow thermodynamic control of the reaction products.[8] Alternatively, utilising bonds which have been successfully employed in the preparation of COFs, including nitroso,[9] hydrazone[10] and boroxine[11]

linkages, could be implemented in the formation of more structurally or chemically robust POCs.

With respect to Xe/Kr separation, future materials prepared specifically for this application need to adhere to the criteria outlined by Banerjee *et al.*,[12] with narrow pores of uniform width, which are large enough to accommodate a single Xe atom, being a critical prerequisite. Due to the difficulty of predicting how a POC molecule will self-assemble and subsequently pack in the solid state, synthesising new cages specifically for this purpose is not trivial. Therefore, the use of simulation studies to guide towards and identify promising candidates, which has been successfully implemented for MOFs, will prove crucial.

6.3 References

1. F. Orsini, G. Sello and G. Bestetti, *Tetrahedron: Asymmetry*, 2001, **12**, 2961-2969.
2. C. Boga, C. Fiorelli and D. Savoia, *Synthesis*, 2006, 285-292.
3. Y. N. Belokon, J. Fuentes, M. North and J. W. Steed, *Tetrahedron*, 2004, **60**, 3191-3204.
4. M. Liu, M. A. Little, K. E. Jelfs, J. T. A. Jones, M. Schmidtmann, S. Y. Chong, T. Hasell and A. I. Cooper, *J. Am. Chem. Soc.*, 2014, **136**, 7583-7586.
5. R. A. Smaldone, R. S. Forgan, H. Furukawa, J. J. Gassensmith, A. M. Z. Slawin, O. M. Yaghi and J. F. Stoddart, *Angew. Chem. Int. Ed.*, 2010, **49**, 8630-8634.
6. A. Kewley, A. Stephenson, L. Chen, M. E. Briggs, T. Hasell and A. I. Cooper, *Chem. Mater.*, 2015, **27**, 3207-3210.
7. A. Avellaneda, P. Valente, A. Burgun, J. D. Evans, A. W. Markwell-Heys, D. Rankine, D. J. Nielsen, M. R. Hill, C. J. Sumby and C. J. Doonan, *Angew. Chem.*, 2013, **52**, 3746-3749.
8. Q. Wang, C. Zhang, B. C. Noll, H. Long, Y. Jin and W. Zhang, *Angew. Chem. Int. Ed.*, 2014, **53**, 10663-10667.
9. D. Beaudoin, T. Maris and J. D. Wuest, *Nat. Chem.*, 2013, **5**, 830-834.
10. F. J. Uribe-Romo, C. J. Doonan, H. Furukawa, K. Oisaki and O. M. Yaghi, *J. Am. Chem. Soc.*, 2011, **133**, 11478-11481.
11. A. P. Côté, A. I. Benin, N. W. Ockwig, M. O'Keeffe, A. J. Matzger and O. M. Yaghi, *Science*, 2005, **310**, 1166-1170.
12. D. Banerjee, A. J. Cairns, J. Liu, R. K. Motkuri, S. K. Nune, C. A. Fernandez, R. Krishna, D. M. Strachan and P. K. Thallapally, *Acc. Chem. Res.*, 2015, **48**, 211-219.